Co-funded by the
Erasmus+ Programme
of the European Union

Semi-Automated Workflow for Multi-Scale Analysis of Heatwaves: A Case Study of Lyon, France

Abuzar Popal

A Thesis Submitted for the Joint Programme of

Master in Urban Climate & Sustainability

August 2021

Author	**Publication type**	**Completion year**
Popal, Abuzar	Thesis	2021
	Number of pages: 66	
Supervisor I	**Supervisor II**	
Prof./Dr. José Dueñas	Prof./Dr. Benjamin Fisher	

Title

Semi-Automated Workflow for Multi-Scale Analysis of Heatwaves: A Case Study of Lyon, France

Degree: Master in Urban Climate & Sustainability

Abstract

Globally, the frequency, severity, and length of heatwaves have intensified and are expected to increase. While many methods for estimating heatwave risk and mapping methodologies have been developed, a comprehensive, harmonized multiscale assessment of the most impacted areas remains absent. Currently, heatwave risk assessment is either too generic and does not adequately represent the heterogeneous urban landscape, or it requires a large amount of data, is computationally intensive, and takes a long time at the microscale level. This research developed a novel semi-automated approach to analyze heatwaves at two different scales: city and neighborhood. Thirteen of the most frequently used machine learning algorithms were used in this research to determine which algorithms delivered the best results for heatwave hotspot identification. The XGBoost classifier achieved the highest accuracy of 94% and was chosen as the basis for forecasting heatwave hotspots. The normalized difference building index (NDBI), the enhanced vegetation index (EVI), the percent of the industrial area (Industrial A P), the albedo, the percent of low-skilled workers (Workers P), and the digital elevation model (DEM) are the factors that contributed the most to the projection of heatwave hotspots. NDBI was the most significant factor in the model, accounting for 30% of the total. The temperature was positively correlated with NDBI, Industrial A P, and Worker P, and EVI, albedo, and DEM were inversely correlated with temperature. The workflow combined city-scale analysis into neighborhood-scale analysis by examining the most severely affected areas in more detail, and greening scenarios were applied to simulate the appropriate heatwave mitigation threshold. Greening 50% of the three most impacted areas was sufficient to reduce the risk from Extreme to High, resulting in a 0.4°C to 0.5°C reduction. It is crucial for decision-makers to quickly explore hotspots at different scales within a heatwave-affected region to efficiently allocate emergency operations in a timely manner and plan future mitigation strategies to reduce the effect of a heatwave in the most impacted areas.

Keywords

Remote Sensing, Land Surface Temperature, Machine Learning, Heatwave Mitigation Scenario Planning , Heatwave Mapping

Originality statement. I hereby declare that this Master's dissertation is my own original work, does not contain other people's work without this being stated, cited and referenced, has not been submitted elsewhere in fulfilment of the requirements of this or any other award.	**Signature** **Abuzar Popal**

ACKNOWLEDGEMENTS

I would like to thank my supervisors José Dueñas, Benjamin Fisher and Rohinton Emmanuel for their continued feedback, support, and guidance during the course of the dissertation.

I would also like to thank my family for their continued support and encouragement throughout the process.

TABLE OF CONTENTS

INDEX OF FIGURES

INDEX OF TABLES

CHAPTER 1: INTRODUCTION

1.1 Rationale

The Intergovernmental Panel on Climate Change (IPCC) identified heatwaves as one of the extreme weather phenomena associated with climate change (Smith et al., 2009). Worldwide, the frequency, severity, and length of heatwaves have intensified and are expected to increase. Heatwaves have become warmer, longer-lasting, and far more widespread while also happening earlier in the season (Perkins-Kirkpatrick et al., 2016). Heatwaves are among the most catastrophic natural hazards, yet they are overlooked mainly due to the associated fatalities and destruction are not immediately evident. Globally, population sensitivity to heat is increasing due to climate change, and this number will grow. Across Europe, it is projected that extreme weather events will continue to increase, droughts will deteriorate, and heatwaves will become more extreme and extended (Liu et al., 2020). Extreme heat events, in particular, are well recognized to have a detrimental effect on human health (Akhtar, 2020). As a result, threat assessment analysis is essential for determining which elements are at risk when exposed to a heatwave (Lowe, Ebi & Forsberg, 2011; Perkins-Kirkpatrick et al., 2016).

Many researchers have studied spatial hazard mapping based on the statistical regression method since it is simple to operate and provides sufficient accuracy (Chan & Konstantinou, 2020; Morabito et al., 2015). Earlier regression methods concentrated on the statistical connection between land surface temperature (LST) and vegetation indices, such as the normalized difference and vegetation index (NDVI). Other remote sensing indices, such as the normalized difference water index (NDWI) and the normalized difference building index (NDBI), were utilized to conduct remotely sensed research in a variety of contexts (Balcik, 2014; Karakuş, 2019; Soltanifard & Aliabadi, 2019). Recent research has also examined linear and nonlinear regression techniques involving temperature and various satellite imagery induced indices, such as the spatially weighted regression model, Lasso model, and Polynomial regression model (Liao, Hou & Strickland, 2016; Moolgavkar, 2000; Samoli et al., 2007). However, Regression models are susceptible to overfitting and have are poor accuracy when dealing with nonlinear relationships between dependent and independent variables (Ray, 2019). Due to geographic heterogeneity, the relationship between land surface temperature and surface factors is usually spatially nonstationary and nonlinear.

Support vector machine (SVM), regression trees, artificial neural network (ANN), gradient boosting (GB), and random forest (RF) are examples of machine learning algorithms that have achieved excellent accuracies in fitting relationships between temperature and other environmental variables (Bakar, Pradhan, Lay & Abdullahi, 2016; Huang et al., 2015; Shatnawi & Abu Qdais, 2019; Zhang & Sun, 2019). The resilience of machine learning models, when deployed to diverse datasets using a machine learning algorithm, may be ascribed to the incorporation of numerous types of independent variables within a robust model, representing the nonlinear connection among dependent and independent variables (Kafy et al., 2021). As a result, numerous studies have been conducted to evaluate existing machine learning methods; Bisquert et al. (2016) examined numerous propagation approaches using two distinct sensors, demonstrating the utility of segmentation strategies. Many studies on the connection of urban land-use / land cover and surface temperature have shown that temperature has an inverse relation with vegetation (Masoudi & Tan, 2019; Hua et al., 2017). and positive correlation with an impervious surface (Li, Heap, Potter & Daniell, 2011; Myint et al., 2011). Li et al., 2019 used a representative spectral index to assess several machine learning models, emphasizing the relevance of vegetation and built-up indices in predictions. Recent research has developed large-scale simulation systems to solve complicated problems,

and these new quantitative study methods are particularly relevant to public health management (Sanchez Cristal, Metcalf, Kreisberg & Little, 2019; Wang, Olofsson, Shen & Bai, 2015).

The brief period preceding and following a disaster is critical for humanitarian and assistance relief operations; hence, a rapid and generalized analysis is necessary. The fast growth in policymakers' use of spatially generated information for decision-making is primarily because of its capacity to handle operational requirements efficiently and effectively across all scales (Beamon & Kotleba, 2006). The data is used to conduct various in-depth assessments of natural disasters, including disaster assessment, risk estimation, and mitigation planning (Sansare & Mhaske, 2020). For visualizing areas damaged by a heatwave, rapid damage mapping is crucial for effectively planning and allocating disaster response and recovery operations. It is vital to emphasize that non-expert users, such as emergency response workers and decision-makers, cannot interpret raw satellite imagery despite improvements in remote sensing availability (Beamon & Kotleba, 2006). To ensure that the resulting products are correctly comprehended by everyone, hazard maps, analysis, and indicators should be prepared by a GIS specialist. The elements of data processing and direct dissemination relationship between the decision-makers and emergency assessment team are critical yet usually ignored. Without a clear and straightforward explanation of the complex image classification, modeling, and GIS deliverables, the emergency response team will get little value from the products (Rao, Rao & Kubo, 2018).

Airborne remote sensing data is commonly utilized before a severe event to map the regions most susceptible to heat exposure and mortality and provide an effective alert system. The city-scale temperature reference based on meteorological station data is overly generalized for heatwave risk and does not designate the heterogeneity of the urban environment (Jedlovec, Crane & Quattrochi, 2017). Recently, satellite imagery,auxiliary data such as census indicators, and remote sensing indices have been incorporated into machine learning models to assess risk variables' geographical variability and create a more comprehensive health warning system. Most research in extreme temperature-related forecasting frameworks focuses on a particular scale of analysis (Park & Kim, 2018; Shi et al., 2021). Micro-level models have a higher resolution in mapping temperature risk, but due to their increased processing requirements and greater computational complexity, however, the models cannot be spatially expanded to cover the entire municipality. To date, the resolution of mesoscale models is unlikely to bring specifics regarding complex urban morphology, despite their ability to study city-scale temperature impacts (Dong, Mitra, Greer & Burt, 2018). The reliance on the aggregation of many years of data to produce significant accuracies necessitates the availability of various multi-year meteorological and land-use data that might not be available for every location. Laaidi et al. (2012) used sixty-one NOAA-AVHRR satellites images of Paris, France, to establish the daily fluctuations in surface temperature. Efficient resource management necessitates concise data processing as well as assimilation at specific scales, with the core principle being that the larger the area of interest, the more aggregate data that can be considered at the expense of thematic differentiation and spatial accuracy of the map components (Weiers, Bock, Wissen & Rossner, 2004). Even though various approaches have been used to estimate heatwave risk and mapping procedures, a comprehensive harmonized multiscale assessment of the most impacted areas remains absent (Zhou, Bonafoni, Zhang & Wang, 2018). Therefore, a new workflow that requires limited data sources that can also resolve the feature selection challenges and define heatwave risk concerning an urban environment in a more thorough method is urgently required.

In recent years, research into mitigating the UHI impact has risen in popularity. In the literature, a variety of urban mitigation techniques have been suggested, including the use of highly reflecting construction materials, attention to building geometry, improving urban vegetation proportions, and the use of green and cool roofs (Akbari et al., 2016; Santamouris, 2013; Yang et al., 2018). Most research suggests that

increasing the percentage of green spaces and using higher reflectivity materials in metropolitan areas can assist cities in mitigating UHI. Microscale mitigation solutions rely on a wealth of data from a range of sources, including meteorological and detailed urban morphology dynamics (Akbari et al., 2016). The process is usually computationally intensive, time-consuming, and requires specialized proprietary software to simulate scenarios. There is an urgent need for rapid generalized analysis of greening scenarios that require only a few resources and can be completed in a short period of time.

1.2 Aims & Objectives

Founded on the current situation, this research intends to:

1) Quantitatively evaluate the performance of thirteen machine learning algorithms in highlighting the most vulnerable areas within an area stricken by heatwaves.
2) Test various climate, land use/land cover, topographic, socio-demographic, and urban morphology metrics to determine the factors that contribute most to the model and their relation to temperature.
3) Create heatwave risk maps that decision-makers can easily interpret with little to no GIS/technical expertise.
4) Simulation of greening scenarios to mitigate the effects of most impacted areas.
5) Package the workflow with minimal input from the user while quantifying most vulnerable areas quickly.

Ultimately, this study aims to answer the resulting important questions: 1) Which machine learning model produces the best results in heatwave hotspot identification? 2) What factors contribute the most to the model prediction? 3) How are the factors correlated to heatwave risk? 4) What are the connections between hazard and vulnerable populations, and how are heatwave risk hotspots distributed spatially? 5) How much greening is required to sufficiently reduce heatwave risk? The answers to these questions will impact emergency response efforts during a heatwave and future urban planning efforts in mitigating the effects of a heatwave in Lyon, France.

CHAPTER 2: LITERATURE REVIEW

2.1 Heatwave Overview

Climate change-related hazards have increased in recent decades, particularly in heatwave severity and frequency, and are anticipated to persist throughout the twenty-first century. The Intergovernmental Panel on Climate Change (IPCC) has identified heatwaves as one of the extreme weather events associated with climate change (Smith et al., 2009). Worldwide, the frequency, intensity, and duration of heatwaves have increased and will continue to increase. Heatwaves are one of the most deadly natural hazards, yet they get limited attention since their fatalities and damage are not usually immediately apparent (Mushore, Mutanga, Odindi & Dube, 2018). Climate change is increasing the vulnerability of communities globally to heat, and this trend will continue. In the 19 years between 1998 and 2017, around 166,000 individuals have died from heatwaves. During the 2003 European heatwave, more than 70.000 people died in Europe (World Health Organisation, 2017). Since 1880, global surface temperatures have increased by 0.85 °C, which has resulted in significant shifts in the probability of extreme weather events (IPCC 2013). Over the last decade, heatwaves have gotten progressively hotter, last longer, and arrive earlier in the season (Perkins-Kirkpatrick & Gibson, 2017).

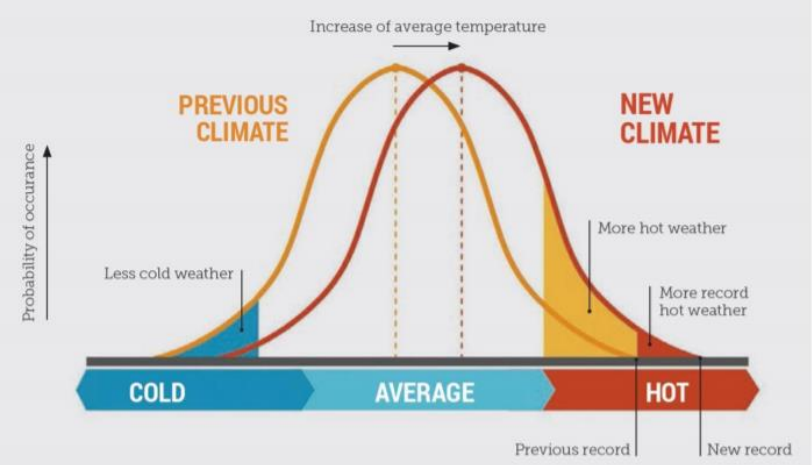

Figure 1 - Connection between normal and extreme temperatures, the relation between a changing average under climate change, and the ratio of extreme weather events (Steffen, 2014)

It is projected that the number of extreme weather occurrences in Europe will increase in the future, droughts will deteriorate, and heatwaves will grow more intense and longer in duration (Morabito et al., 2015). High temperatures, especially extreme heat events, are well considered to be harmful to human health (Akhtar, 2020). Since 1900, excessive heat has caused more deaths in Australia than all other natural hazards combined, accounting for more than 55 percent of all deaths related to natural hazards. In order to evaluate which aspects are at risk as a result of exposure to an extreme temperature hazard, risk assessment analysis is essential (Perkins-Kirkpatrick et al., 2016). Depending on the scale of analysis, efficient resource management necessitates explicit data processing and integration definition. The underlying concept would

be that the larger the area of interest, the greater the aggregate level of data that can be considered at the cost of the thematic distinction and spatial precision of the map items (Morabito et al., 2015). Temperature increases will raise the risk of heatwaves to public health. A lack of local awareness could jeopardize the effectiveness of policies and mitigation measures. To quantify the heatwave danger posed by climate change, more extensive localized evaluation methods are still necessary. While the probability of heatwave events increasing as a result of climate change is projected to grow in the medium to long term, the degree of this shift remains unclear (Chan & Konstantinou, 2020).

By concentrating on instances of higher temperatures, Weiers, Bock, Wissen, & Rossner (2004) detected heatwaves above 28°C, observed a two- to three-fold decline in the average duration between 2 consecutive occurrences of a six-day long heatwave and a two-three-fold increase in the length of a heatwave with an average return period of five years. Population over 65 years old and children, particularly those who have chronic illnesses, are especially vulnerable to the effects of a heatwave. Hospital visits increased by 5% throughout the population, by 13% for children aged 15 and under, and by 19% for children aged five and under, according to Campbell et al. (2019), who looked at the effects of hospital visits and intense heatwaves on different socio-demographic categories.

2.2 Urban Heat Island (UHI)

Heat has been exacerbated as a result of urbanization and the increased number of people living in cities (Sultana & Satyanarayana, 2020). Heatwaves significantly have a negative impact on urban areas due to the large area of rough artificial surfaces, regional and local climatic conditions, and a lack of vegetation and green space, resulting in variations in air temperatures and the development of intense urban heat islands (Cui, Xu, Dong & Qin, 2016) . The UHI indicates the temperature difference between urban and rural areas, and the magnitude of the UHI in urban areas is positive. Numerous studies have established a strong link between heatwaves and human mortality due to their intensity, frequency, and duration (Akhtar, 2020; Arsenović et al., 2019; Stafoggia et al., 2006). Death from heat-related illness is among the most severe public health threats identified in these findings. The harmful health impacts of high temperatures are also dependent on a number of factors impacting the general public's sensitivity to high temperatures and their ability to react to and cope with extreme heat (Arsenović et al., 2019). Elderly, children, socially marginalized, and chronically ill people are among the demographic categories most vulnerable to heatwaves. According to one study conducted in China, the urban heat island effect contributes around 30% to global warming (Huang & Lu, 2015). In contrast, according to a peer-reviewed report from 1999, the impacts of urban and rural environments on global average temperature trends are negligible (Peterson et al., 1999). Climate change, according to several studies, has made this consequence more severe (Hashim & Hashim, 2016; Mills, 2009; Otto, 2019).

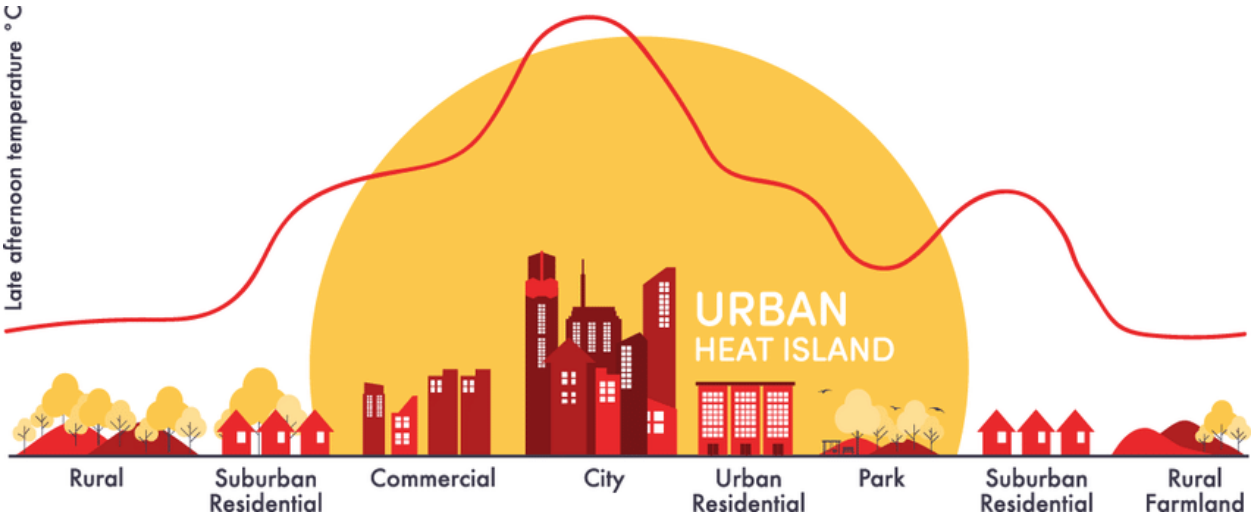

Figure 2 - Urban Heat Island Effect (Fuladlu, 2020)

2.3 Sustainable Urbanization

The sustainability capacity of many infrastructure sectors has improved. Green infrastructure is a network of natural environment elements within an urban region, including green and blue areas that provide ecosystem services (Demuzere et al., 2014). Parks, ponds, street trees, gardens, and urban forests are all part of the green infrastructure. Green infrastructure that has been thoughtfully developed includes environmental services that contribute to human well-being, wildlife habitat conservation, and biodiversity (Rafael et al., 2018). Green infrastructure schemes seek to reduce the environmental impact of buildings over their lifetime by focusing on water-saving and energy-efficient technologies. More climate-friendly technologies are also being developed and implemented, reducing the reliance on coal, fossil fuels, and energy-intensive sectors (Rodrigues et al., 2019; Santamouris & Osmond, 2020). The availability of funds for green infrastructure projects has expanded considerably as more financing is made available through Paris Agreement-aligned programs to offset some of the impacts of climate change on metropolitan areas (Uyar, 2017).

Cities pose significant climate issues with high population densities, including urban heat islands and deteriorated ventilation systems. A solid grasp of the urban outdoor climate is necessary for sustainable urban development (Demuzere et al., 2014). There has been considerable development in remote sensing capabilities, and as a result, satellite data has been widely utilized in the research of UHI concepts and mitigation measures. Extensive research has been performed to determine spatial-temporal differences in the urban thermal environment and their interconnections with various urban environments (Chen et al., 2020). Local Climate Zones (LCZs) are one common method of monitoring thermal conditions in diverse urban structures in cities (Stewart, Oke & Krayenhoff, 2014). Based on land surface parameters such as building height, urban layout, and land use/land cover, the methodology separates the metropolitan region into 17 basic groups. Centered on temperature observations and model simulations, the research community verifies significant temperature disparities among various LCZs. Bartesaghi Koc, Osmond, Peters and Irger (2018) used high-resolution airborne data to understand better the surface temperature properties of LCZs in an Australian city and discovered that day and night thermal conditions varied across different LCZ

categories. With Landsat data, Geletič, Lehnert & Dobrovolný, (2016) investigated the LST contrast within local climate zones in two European cities. Zhao et al. (2019) used remote sensing data to analysis local climate patterns in three cities in Texas. In high-density areas, (Zhou, Chen, Zhang & Zhan, 2013) employed a combination of multi-source satellite data to assess the thermal characteristics of landuse. However, more validation is required due to the fact that temperature varies for cities with varying geographical locations and climatic backgrounds in relation to the extent of the city (Chen et al., 2020).

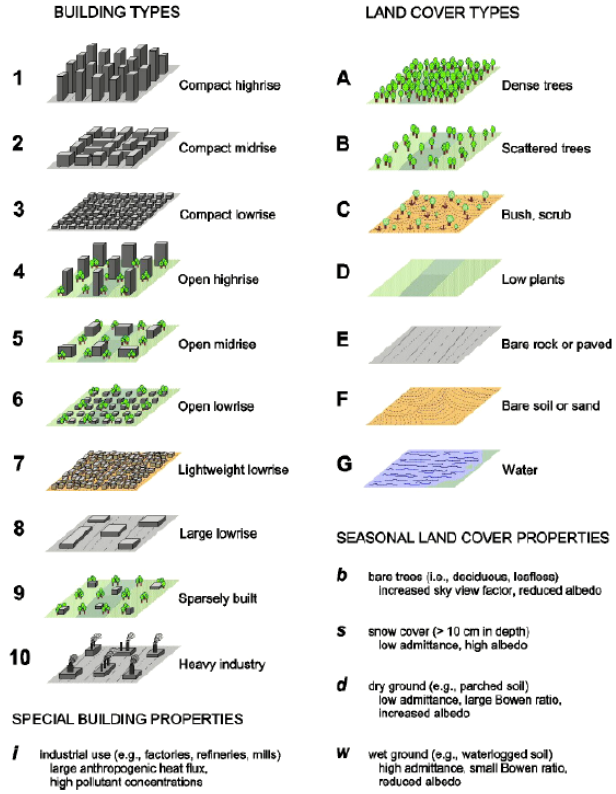

Figure 3 - Local Climate Zone Classes (Stewart, Oke & Krayenhoff, 2014)

2.4 Classification

The ability to automatically classify urban structures has dramatically improved over the previous decade due to better classifiers and the availability of more detailed data sets (Bechtel & Daneke, 2012). Urban surface and structural analyses using Synthetic Aperture Radar (SAR), thermal, hyperspectral, and high-resolution optical data are among the most common applications (Li & Guo, 2016). Furthermore, a large number of multi-sensor hybrid techniques have been employed. The use of these methodologies, on the other hand, is severely restricted by the wide range of typologies that are employed to discriminate distinct urban morphologies (Javanroodi, Mahdavinejad & Nik, 2018; Scott, Petropoulos, Moxley & Malcolm, 2014). While some studies use a simple distinction between water, plants, and buildings, others use more comprehensive land cover categories and, in particular, surface material typologies (Vargo, Habeeb & Stone, 2013). These groupings have been mainly defined qualitatively, integrating utility and structure characteristics. As a result of this variation, there is limited transferability and inconsistent outcome comparability (Bechtel & Daneke, 2012).

More deaths are due to heatwaves than by any other natural phenomenon, and so, many researchers examined the temperature threshold that might have more adverse health impacts on the population (Wilhelmi and Hayden, 2010). Gosling, McGregor and Páldy ‘s (2007) findings are based on a thorough examination of specific thresholds and accompanying death rates. Mortality increased as a result of not only the occurrence of extreme heat events but also owing to the increased intensity and duration of the heatwave exposure. Farhan, Pattipati, Wang and Luh (2015) tested multiple machine learning algorithms using environmental and physiological factors to predict individual thermal comfort with Support Vector Machines (SVM) obtaining the highest accuracy of 77%. Although this exposure has severe health implications, it is also a result of other factors, including population sensitivity to temperature, their ability to tolerate and react to a temperature increase (Wilhelmi & Hayden, 2010).

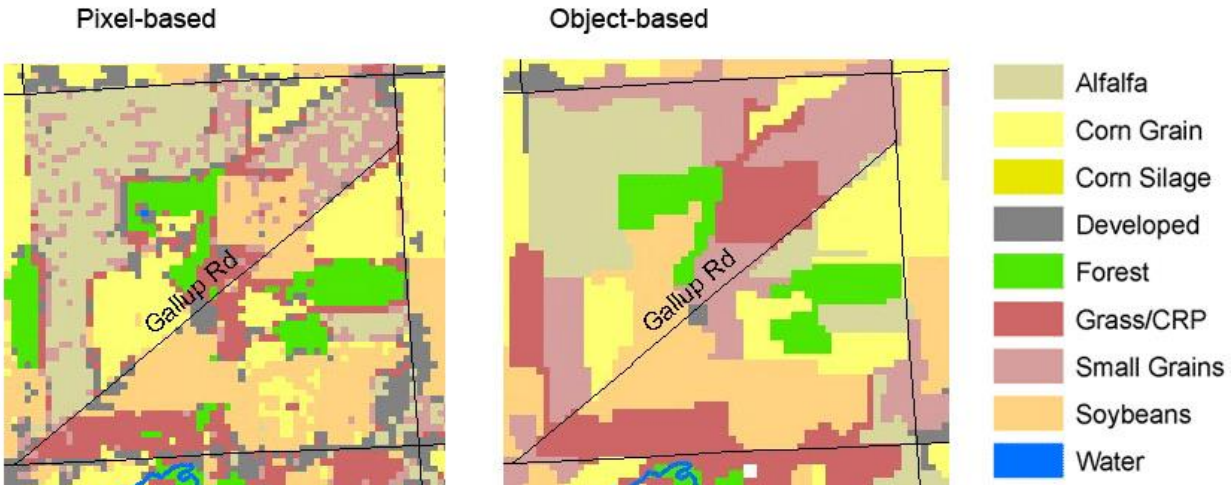

Figure 4 - Pixel-based vs Object-based Classification (Powell & Brooks, 2008)

Object-based and pixel-based analysis are the two main methodologies used to analyze urban morphological constructs. Through the use of current data sets, it is feasible to classify and monitor surface materials. Object-based techniques enable the incorporation of image segmentation into more realistic urban contextual morphologies (Hussain et al., 2013). For example, an object-oriented multi-level soft classification model for identifying urban structural types may use high-resolution satellite data and a digital surface model produced from LIDAR. Given that urban systems on the surface of the earth are among the most complex, the object-oriented approach continues to be challenging. A large amount of contextual information is, therefore, necessary, making microscale research a challenging endeavor to complete accurately (Shackelford & Davis, 2003). For very homogenous urban structures, a less complicated pixel method could be considered. There is no segmentation in this procedure. The pixels are instead classified explicitly at a lesser degree of detail, which is far less time-consuming. Bechtel and Daneke (2012) used multiple parameters to compute different machine learning techniques for LCZ categorization.

2.5 Land Surface Temperature

Most remote sensing heatwave analysis is based on satellite Land Surface Temperature (LST) measurements with fewer resources devoted to air temperature (Ban, 2016). The LST readings combined with other indexes and auxiliary data are then used to predict air temperature values which is one of the main contributors to heatwaves. Part of this is attributed to the continuous satellite derived LST data while the air temperature is calculated at a few places where meteorological stations are sparsely situated across a heterogeneous urban landscape (Bokaie, Zarkesh, Arasteh & Hosseini, 2016). A basic statistical analysis provides a linear association between LST and air temperature. The calculation precision is related to the data used to construct the models, such as time and location. Advanced statistical methods typically involve LST, altitude, and NDVI in the air temperature estimation model (Chan & Konstantinou, 2020). This technique uses multiple linear regression analysis to measure air temperature, and the precision of the estimate is superior to that of a simplified statistical procedure. Although LSTs are a significant control variable for urban energy balance as well as for assessing UHI impacts, their importance to human health is unclear (Stafoggia et al., 2006). Applying LST towards assessment of hazard is due to the ease with which it can be mapped (Sultana & Satyanarayana, 2020). Kalma, McVicar & McCabe (2008) used LST and thermal factors from remote sensing to approximation evaporation. LST approaches do not account for the multitude of variables that lead to local-scale air temperature heterogeneity, such as land cover, building structures, vegetation intensity, exposure to the sun, and wind mechanics (Stewart, Oke & Krayenhoff, 2014; Voogt & Oke, 2003). The small-scale spatial heterogeneity of these variables (1–100 m) goes undetected by weather stations usually placed far apart, from several kilometers to 100km apart (Stewart, Oke & Krayenhoff, 2014). Specific approaches are being employed to address this constraint, such as implementing dense temperature control systems (Han & Xu, 2013) or portable testing utilizing vehicles or bicycles (Fabiani et al., 2019), but these approaches remain expensive to introduce and sustain.

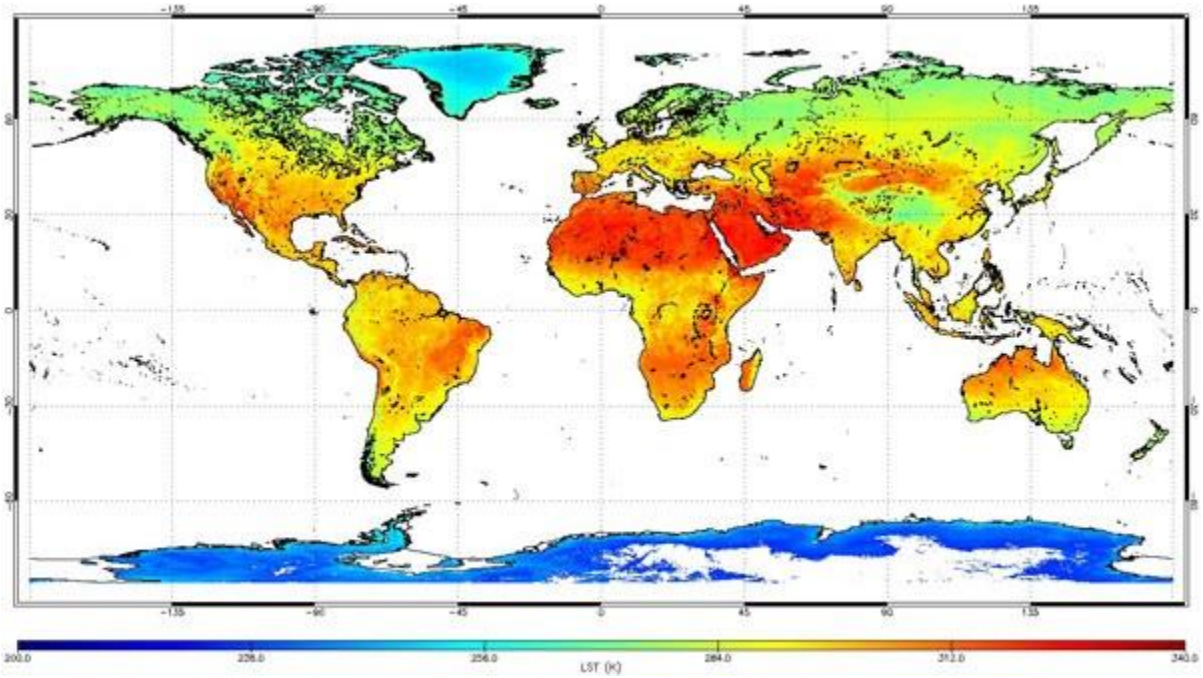

Figure 5 - Global LST for 2006 (ESA, 2006)

2.6 Machine Learning Models

Early research centered on utilizing simulations with weighted regression models to monitor heatwaves. Regression models, however, cannot capture the typically heterogeneous and spatially complex associations between the UHI factors and UHIs. Because of their capability to learn and emulate immensely complicated nonlinear data, machine learning algorithms generally produce better fit models than traditional statistical methods (Huang et al., 2015; Zhang & Sun, 2019). Even shallow neural network models with one hidden layer have been used in the majority of current studies to investigate UHIs with significant accuracy (Balcik, 2014). On the other hand, neural networks require a substantial quantity of training data, are susceptible to overfitting, and have difficulty with generalization.

Deep Learning (DL) is one of the most recent developments in the fields of computer learning and artificial intelligence science. In 1986, the term "deep learning" was initially used to represent machine learning, and in 2000, the definition was broadened to include artificial neural networks (ANN) (Saputra & Lee, 2019). There are numerous layers to a deep learning technique, which allows it to learn different aspects of data by approaching it from different levels of abstraction (LeCun et al., 2015). For the time being, basic linear, multivariate linear, and nonlinear algorithms can be used to distinguish satellite-observed brightness temperatures from LST (Liao, Hou & Strickland, 2016). Prior research has demonstrated that machine learning algorithms produce more accurate air temperature measurements than other techniques (Bakar, Pradhan, Lay & Abdullahi, 2016; Huang et al., 2015; Shatnawi & Abu Qdais, 2019; Zhang & Sun, 2019).

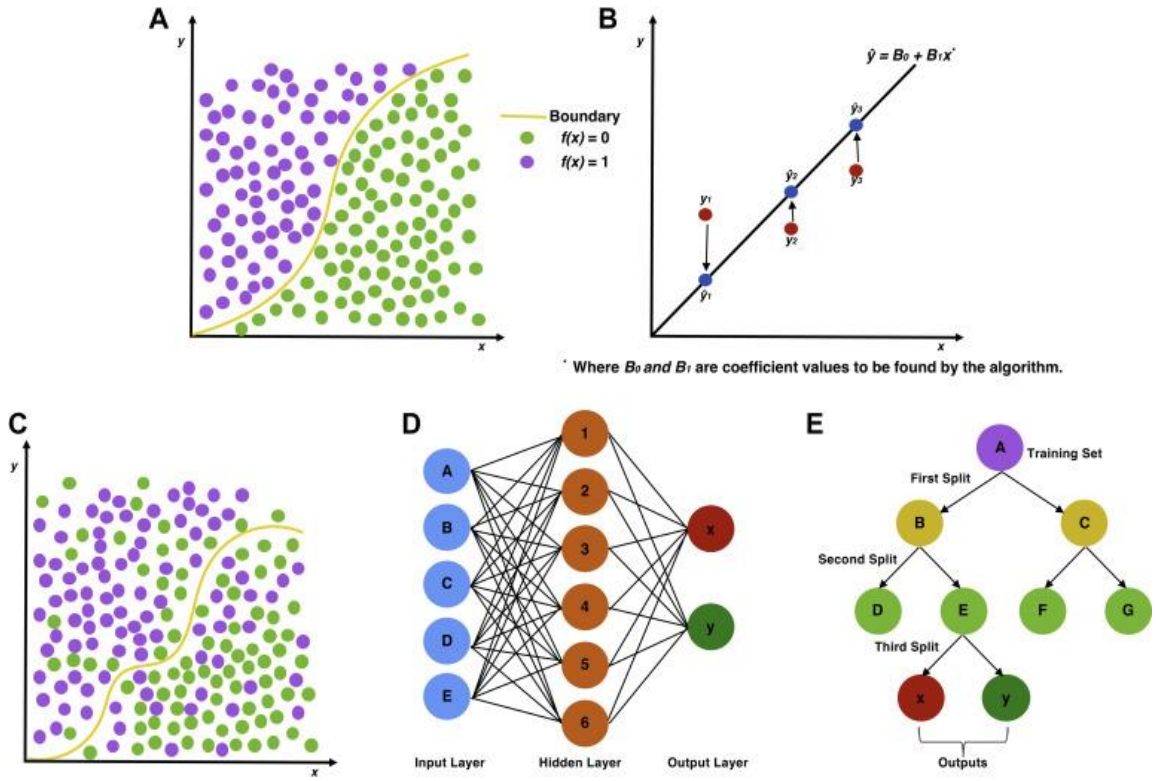

Figure 6 - Illustration of Machine Learning Classifier, logistic regression(A) linear regression (B) support vector machine (C), artificial neural network (D), and decision tree (E) (Tong, 2019)

A good illustration of this is found in machine learning models such as neural networks, which exhibit increased precision and a 1.29°C reduction in root-mean-square error (RMSE) compared to linear models (Zhou, Chen, Zhang & Zhan, 2013). Using the newest version of the Chinese meteorological satellite data, Zhou et al. (2020) used six machine-learning algorithms for air temperature approximation: random forest, multivariate linear regression (MLR), extreme gradient boosting (XGB), gradient boosting decision tree, deep neural network (DNN), and k-nearest neighbors. The XGB model produced a more robust and significantly more accurate air temperature prediction for China-wide air temperature prediction (Zhou et al., 2020). When utilized for large-scale air temperature estimation, it can serve as a reference for machine-learning algorithms.

Were, Bui, Dick & Singh (2015) estimated extreme air temperature using random forests, neural networks, and support vector machines. More accurate than multivariate regression models, machine learning methods capture the nonlinear relation between different inputs and temperature (Modaresi, Araghinejad & Ebrahimi, 2018; Were, Bui, Dick & Singh, 2015). Air temperature estimates must be within 1-2°C of the actual temperature and have high temporal and geographical precision in order to be considered dependable. Further research is required in this situation (Coutts et al., 2016). In previous studies, surface characteristics and atmospheric conditions have been significantly impacted by the interaction between LST and air temperature (Coutts et al., 2016; Were, Bui, Dick & Singh, 2015). Thus, by including a large number of additional characteristics (Coutts et al., 2016), the precision of extreme temperature estimation was significantly improved.

The robustness of machine learning algorithms to solve complex problems has been applied to various remote sensing applications. Youssef et al. (2016) used satellite imagery and boosted regression tree techniques to generate landslide hazard maps with reasonable accuracy. For boreal landscape, Abdi (2020) compared machine learning algorithm performance in classifying land-use/ landcover change. With an overall accuracy of 75%, Bavaghar (2015) employed logistic regression to identify the position and degree of deforestation based on criteria such as residential area and proximity to roadways. Wu et al. (2017) identified changes in landcover on satellite imagery using SVM and decision trees, with SVM having the highest accuracy of 93 percent. Potgieter et al. (2007) employed Principal Components Analysis (PCA) to predict agricultural area in Australia using a time series of enhanced vegetation index (EVI) measurements. Random forests were the most accurate and reliable method for categorizing agricultural areas in Australia after comparing many machine learning algorithms using Landsat images (Schmidt et al. (2016)). Individual tree attributes were derived by Corte et al. (2020), utilizing the machine learning models by the use of high-density UAV-Lidar data. Modis satellite imagery was integrated into a neural network to forecast future forest fires (Kong et al. 2018).

2.7 Heatwave Mitigation

In recent years, research into mitigating the UHI impact has risen in popularity. In the literature, a variety of urban mitigation techniques have been suggested, including use of highly reflecting construction materials, attention to building geometry, improving urban vegetation proportions, and the use of green and cool roofs (Akbari et al., 2016; Santamouris, 2013; Yang et al., 2018). All of this research suggests that increasing the percentage of green spaces and using higher reflectivity materials in metropolitan areas can assist cities mitigate UHI. Because of the large area occupied by rooftops inside cities, green roofs,

according to Akbari et al (2003), are ideal interventions for reducing UHI impacts. Imran (2012) demonstrated in Melbourne, Australia, that raising green roof proportions from 30% to 90% reduces roof surface UHI by 1°C to 3.8°C during the day, and enhancing cool roof albedo from 0.50 to 0.85 reduces UHI by 2.2°C to 5.2°C. By lowering sensible heat flow, green roofs minimize UHI effects. By providing shade and redistributing available energy to enhanced latent heat transfer via evapotranspiration, vegetation lower sensible heat flux (Rodrigues et al., 2019). However, most models require large amounts of data spanning several years to predict greening situations correctly. Data gathering and processing takes time, requires constant data input from numerous sources at an extremely high spatial resolution over a long period of time, and is often tailored to a particular city (Santamouris & Osmond, 2020).

2.8 Mapping Challenges

The fact that urban and microclimate simulations have higher resolution and more precise data does not exclude their spatial distribution throughout a city because of their high processing costs and the complexity of the elements that are vital to their operation (Demuzere et al., 2014). The results of mesoscale systems have yet to be conclusive in terms of the UHI's large-scale consequences. Although they have some capabilities, they are not effective in explicitly assessing and defining a heterogeneous urban environment (Zhao et al., 2019). To create spatially and computationally viable frameworks, more research is needed to address this unsettling challenge. Current geographical and temporal data are typically captured over a variety of time intervals when data is collected from several sources. Future studies should collect spatiotemporal data over the same time period, and researchers should eventually develop models that incorporate meteorological and urban texture components (Scott, Petropoulos, Moxley & Malcolm, 2014). The lack of a workflow connecting extreme temperature analysis from different scales is severely lacking.

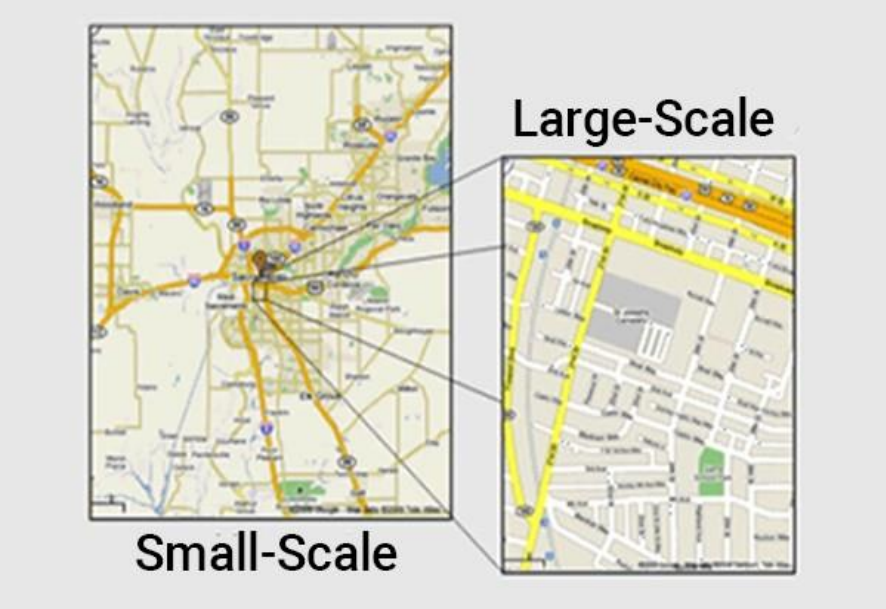

Figure 7 - Small - Scale vs Large-Scale Mapping (Jain, 2020)

Furthermore, while the amount of information available for decision-making has increased, the ability of humans to properly comprehend and utilize this information in disaster management has dropped. Humans are at a disadvantage in instances where actions must be made instantly. A challenge currently observed in the field is the successful incorporation of analysis into a format that is easily interpreted and accessible to the decision-maker (Sultana & Satyanarayana, 2020).

CHAPTER 3: STUDY AREA AND DATA

3.1 Heatwave Event 2018

During the summer of 2018, most of Europe experienced record-breaking temperatures and wildfires as a result of a weaker-than-normal jet stream. Because of an unusually high pressure being maintained across a large area of the northern hemisphere, a heatwave developed in Europe during the summer. The EU was home to 104,000 people over the age of 65 who died because of heat exposure in 2018, accounting for almost one-third of all heat-related deaths in the world (WWA, 2018). The consequences of the heatwave was felt throughout France. Figure 8 displays the Land Surface Temperature anomaly from the average of previous years, indicating that some France regions witnessed over 10°C deviation from the average mean. Despite not breaking any records in terms of temperature or fatalities, France had prolonged temperatures of more than 40 °C that had a detrimental effect on the population. During the early hours of August 4, 2018, the French energy company EDF announced that it would be forced to shut down four nuclear reactors. The actions were taken due to the adjacent river, which was utilized to cool the nuclear reactors, surpassing a crucial temperature (DNA, 2018).

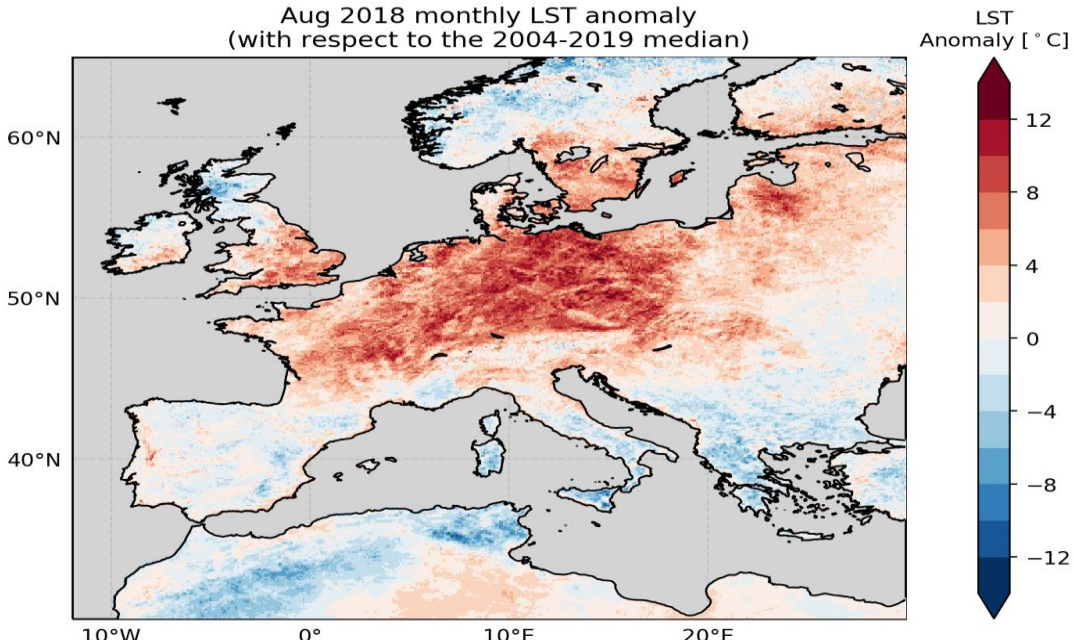

Figure 8 - 2018 Summer Land Surface Temperature Anomaly Across Europe Source: (WWA, 2018)

3.2 Study Area

Lyon has been the economic heart of France since the Renaissance, with a population of over 1.6 million people spread across 1534.60 kilometers of territory. Lyon is a major financial center and a key hub for the pharmaceutical, chemical, and biotechnology sectors. Lyon is located in the central-eastern part of France and situated at the junction of the rivers Rhône and Saône, approximately 470 kilometers southeast

of Paris (Britannica, 2018). Across the previous two decades, the occurrence of heatwaves has increased significantly in Europe. Given that Lyon has consistently been one of the most severely impacted cities in France in terms of heatwave-related fatalities, and because the city provides openly available data from a wide range of variables, it was selected to train the model for heatwave detection.

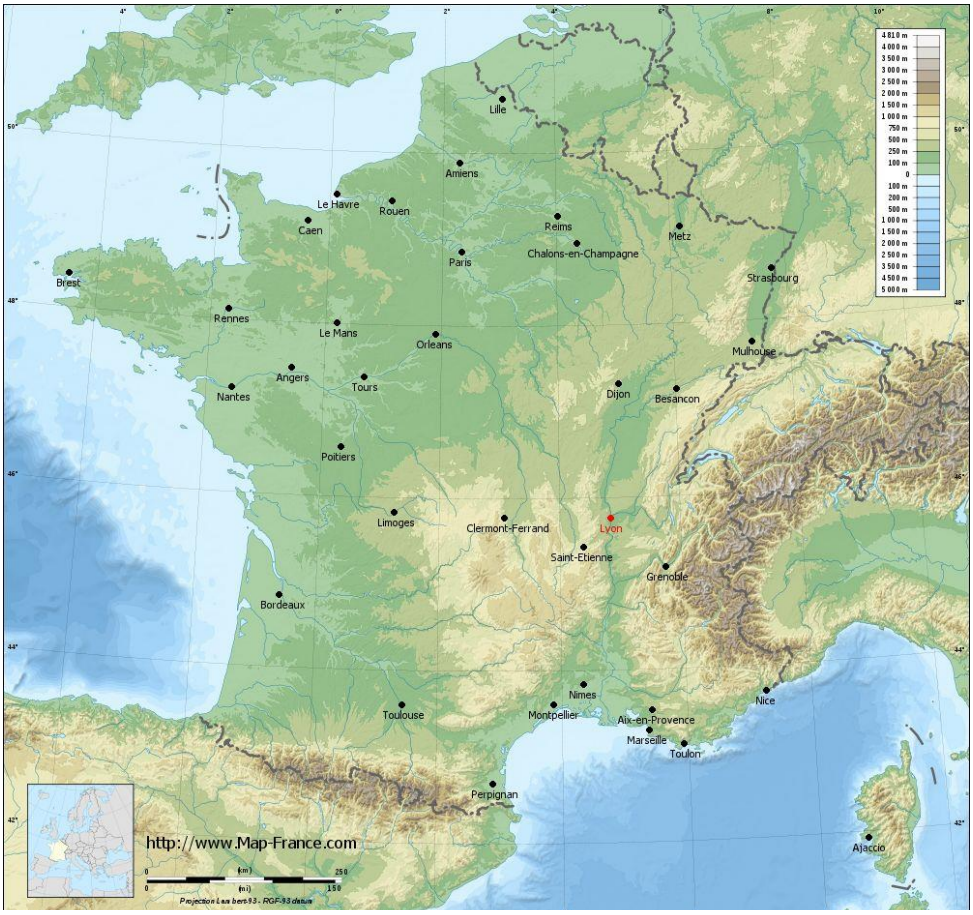

Figure 9 - Map of France (Map France, 2017)

3.3 Data Sources

Lyon's online city platform (https://data.grandlyon.com/) provides a wealth of freely accessible geographical data on a variety of environmental, socioeconomic, and demographic aspects. The platform integrates data from a variety of sources at various scales, including neighborhood, city, regional, and national in a range of formats. Additionally, Lyon's Lidar data is publicly available. Around the time of the 2018 European heatwave, which peaked on August 4, 2018 two satellite images were downloaded for Lyon. The date of image acquisition was constrained since Landsat satellites have a temporal resolution of about 16 days, and some images were discarded because a substantial area of Lyon was obscured by clouds. Table 1 shows the Landsat image specifications utilized in the model. A Landsat image for Glasgow, UK, was also downloaded to evaluate the model's robustness in a different environment.

Table 1 - Landsat 8 Imagery Specifications

Acquisition Date	Path/Row	Landsat	Number of Bands	Spatial Resolution	Radiometric Resolution
12/07/2018	196/28	8	10	30m	16 bit
04/08/2018	197/28	8	10	30m	16 bit
25/06/2018	205/21	8	10	30m	16 bit

Lyon was divided into blocks using Ilots Regroupés pour l'Information Statistique (IRIS) limits. IRIS is the lowest level of census block utilized in France, and it served as the primary unit for disseminating infra-municipal information. The blocks are generated depending on population, with each block consisting of on average of 1,800 to 5,000 persons. Because satellite image induced data and spatial data downloaded from the Lyon city repository are considered simultaneously in the study, the data was assimilated to IRIS blocks and analyzed. In the Lyon area, 29 blocks were removed because they contained missing data for several variables, bringing the total number of blocks to 492 blocks.

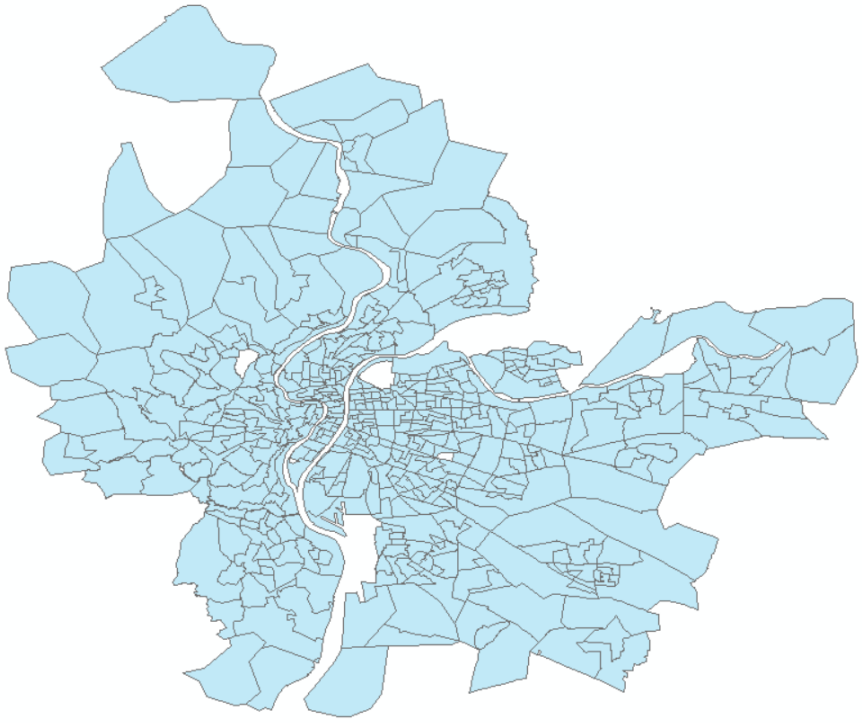

Figure 10 - IRIS blocks of Lyon

CHAPTER 4: METHODOLOGY

4.1 Overview

Even though various approaches have been used to estimate heatwave risk and mapping procedures, a comprehensive harmonized multiscale assessment of the most impacted areas remains absent (Zhou, Bonafoni, Zhang & Wang, 2018). The research proposes a new semi-automated approach for analyzing heatwaves at various scales depicted in Figure 11. Data from Landsat 8 satellite imagery and auxiliary data on socio-demographic, topographic, and environmental factors are clipped to the area of interest and preprocessed to normalize the data due to its multi-source origin. Preprocessing data is a critical stage in Machine Learning. The quality of the data and the valuable information obtained from it directly affect the model's learning capacity; the data needs to be calibrated and preprocessed before feeding it to the model. Preprocessing is the methodical process of assimilating data into a standardized product via filtering, integration, reduction, and transformation (Pant, 2019). The preprocessed data is then routed to the city's lowest level divisions, referred to as "blocks" (or "IRIS" in French), which are analogous to census block groups in the United States of America or the United Kingdom's lower super output areas. The IRIS blocks containing information about 70 factors are then fed into 13 machine learning algorithms for classification, including linear models (LM), linear discriminant analysis (LDA), decision trees (TREE), Naive Bayes (NB), support vector machines (SVM), ensemble methods ,nearest neighbors (KNN), and neural network models. Individual model definitions and hyperparameter adjustment are performed to optimize the accuracy of each model. The relevance and weight of each element contributing to each model are then examined coupled with Principal Component Analysis (PCA) to determine the most significant factors contributing to the prediction of the LST, which is utilized as the premise for defining heatwave hazard.

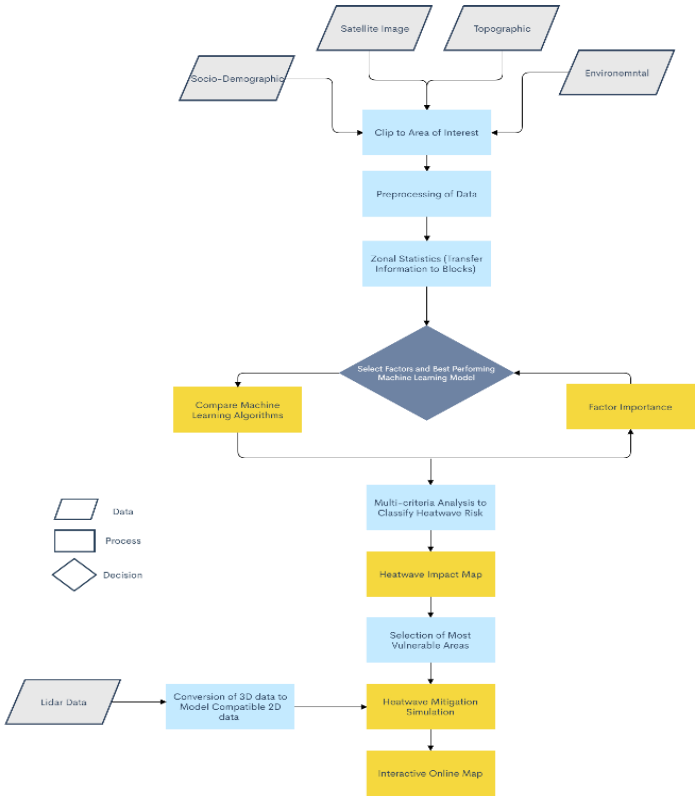

Figure 11 - Semi-Automated Workflow Overview

The machine learning model with the highest overall accuracy and accuracy within the "Extreme" class, which represents the most severely affected areas by heatwaves, is then chosen, along with the factors that contributed the most to the model using the magnitude of feature attributions. Multi-criteria analysis (MCA) is performed on the resulting machine learning output, demonstrating the heatwave's hazard in conjunction with the factors affecting the most vulnerable population. MCA will lower the number of "IRIS" blocks designated as "Extreme" by factoring in both hazard and vulnerable populations to focus attention on the IRIS blocks that require the most attention during a potential heatwave. The MCA-created map will highlight the most severely affected locations, allowing emergency responders and decision-makers to plan and prioritize crucial assistance when resources and time are limited. Next, lidar data for the most afflicted neighborhoods is retrieved to study the areas further. Lidar data provides a more detailed three-dimensional depiction of the site, allowing for additional study of the variables contributing to the higher temperature of the IRIS blocks than the rest of the city. After converting the 3D analysis to model-compatible data, it is used to run several simulations for heatwave mitigation. The most severe IRIS blocks are examined using several scenarios involving green roofs and increased vegetation cover to understand better the implications of various mitigation techniques and their overall effect on temperature. The results will assist city planners in determining the amount of effort necessary to mitigate the areas in the future successfully. Natural disaster management necessitates the rapid integration and dissemination of knowledge; consequently, an online interactive map will contain the research findings, allowing for simple distribution and revision of information with all parties involved.

The semi-automated workflow comprised of five tools that operate in sequence with necessary visual analysis stages in between. In an ideal world, the entire workflow would be implemented in Python, utilizing predefined packages to assist in the performance of intermediate processes; however, Python lacks an interface for visually inspecting transitional results and provides only limited control over the presentation and editing of maps. ArcGIS was utilized to refine the maps and conduct quality control evaluations with its superior interface for displaying data. Fugro software was used to visualize the 3D lidar data easily, as Python and ArcGIS are not very adept at handling big point clouds. Combining the three applications to create the workflow enabled the utilization of each application’s advantages to produce readily available results and adhere to modern requirements for cartographical outputs.

ArcGIS includes tools for spatial and zonal analysis, as well as superior visualization. When working with complex procedures, Python is more powerful and effective, particularly large amounts of data, whereas Fugro is primarily used to visualize Lidar data. Integrating multiple applications was one way to shorten the time required to produce heatwave risk maps. In total, two tools are built within ArcMap using ModelBuilder, and three are written in Python. The workflow is structured to need minimum human interaction, as one tool serves as the input for the next. The separation of the tools was done to ensure that the results were of high quality before going to the next phase. The workflow is divided into five distinct stages:

1. Preprocessing and Zonal Statistics

2. Evaluation of the Machine Learning Model and Feature Importance

3. Multi-Criteria Analysis and Production of Heatwave Risk Map

4. Simulations of Heatwave Mitigation Strategies

5. Interactive Online Map

4.2 Preprocessing and Zonal Statistics

Figure 12 illustrates the procedure for preparing data for processing. Landsat satellite imagery and auxiliary data, comprising all relevant data obtained from the city of Lyon spatial data platform, serve as the two primary data sources. Firstly, the satellite image is cropped to exclude a large portion of the image from the area of interest. By restricting the data to the area of interest, subsequent processes are significantly accelerated. Once the optical bands have been reprojected, the values are scaled using the scale factor indicated in the metadata. Individual bands and their combinations generate various indices that highlight environmental, built-up, topographic, and waterbody aspects. The bulk of the indices are frequently used in research to enhance a particular element of land use/cover; for example, the NDVI index is commonly used to improve vegetation areas. The NDVI method determines a plant's health by evaluating how it reflects light at specific frequencies. Since certain wavelengths are absorbed while others are reflected, the NDVI index optimizes the contrast between visible and near-infrared light. This research aims to evaluate as many metrics as possible to understand which ones relate with the intensity of heatwaves.

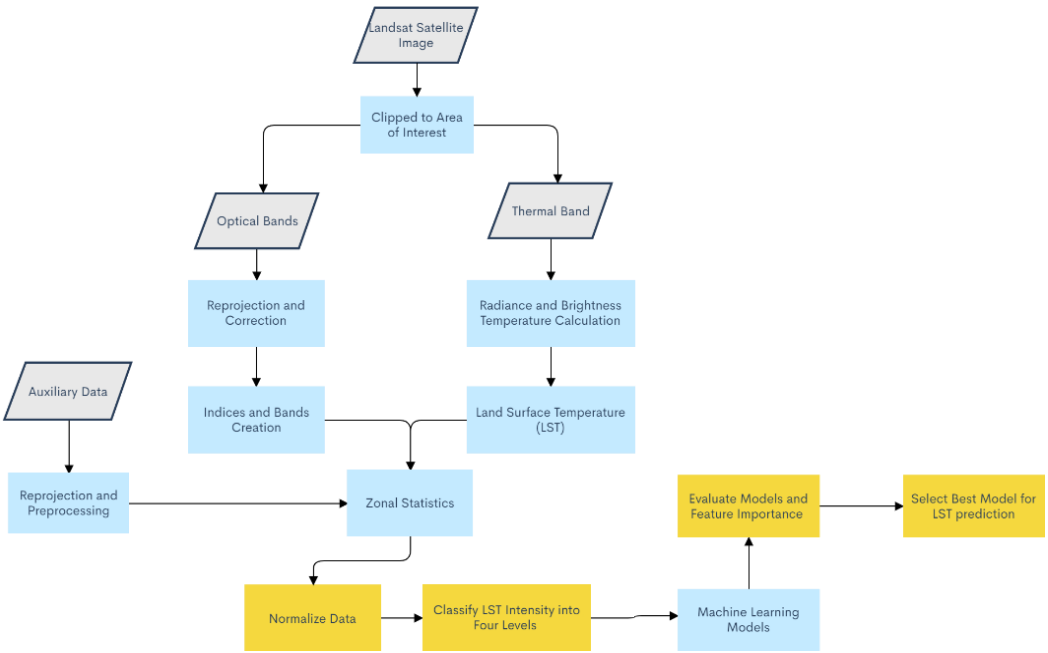

Figure 12 - Pre-processing and Model/Feature Selection Workflow

Band 10 of Landsat 8 imagery is the thermal band used to calculate the land surface temperature. Because LST is intrinsically related to the Earth's surface's radiative and thermodynamic properties, it is routinely used in place of air temperature observations in a wide variety of research. Therefore, digital values must first be translated to radiance and then to usable surface temperature to acquire land surface temperature data.

Instead of analyzing individual pixels, object-based image analysis of remote sensing data aggregates pixels to homogeneous subgroups or areas that may be analyzed. Individual pixels in such areas carry additional data, such as mean and standard deviation for each band. Working with higher quality satellite imagery, which is becoming accessible as sensor quality improves, is also less computationally intensive when pixels are aggregated into zones (Wu et al., 2017). For example, the Zonal Statistics tool in ArcGIS evaluates and

delivers a single statistic at a time. The cell values within an overlapping boundary are used to calculate statistics in a zonal statistics process. This value is used as the cell value for the pixels in the raster result belonging to that section. Since each pixel inside the output raster could only reflect one value, the statistic is generated for only one zone if a zone feature has several overlapping zones (ESRI, 2016).

Zonal Statistics is a critical step that transforms individual pixel values or attributes to the boundary's average. This transformation helps in various ways, including decreasing noise and averaging the readings across a larger region, which mitigates the consequences of outlier values caused by instrument or calibration errors. The tool collects cell values from the value raster for all cells inside each zone to generate a statistic. This classification of cells inside a zone in a value raster is accomplished by superimposing zones on the value raster. Lastly, the mean value of all the raster pixels within a boundary layer is computed for all data within different IRIS boundaries (ESRI, 2016).

Figure 13 - Zonal Statistic Illustration (ESRI, 2016)

The socio-demographic data and some other layers downloaded from the Lyon city spatial repository already came in IRIS boundaries. Therefore, the remainder of the data was converted to the mean pixel value of the IRIS boundary. While the data is estimated, this results in a smooth, easy-to-understand map that avoids pixel values' "salt and pepper" effect (Wu et al., 2017). Alternatively, the mean values will obliterate the detail of hotspots inside an IRIS boundary. However, this detail will add to the ambiguity at the city level when the overall pattern of heatwaves is desired. Additionally, the mean value separates the impacts of outliers or pixels that may have been warped by atmospheric or radiometric distortion.

4.2.1 Landsat 8 Satellite Imagery

The Landsat 8 satellite orbits the Earth in a near-polar sun-synchronous orbit, which means it covers the whole planet at a consistent local time of day. The satellite's return period is 16 days. The OLI sensors of Landsat 8 imagery can acquire images in the visible to thermal infrared spectral ranges. Sensor, solar, atmospheric, and topographic influences all alter Landsat images (Elmes et al., 2020). Preprocessing assists in mitigating these effects to the greatest extent possible for a specific application. Radiometric, atmospheric, and geometric adjustments are generally used when conducting multi-date change detection

of images (Li & Guo, 2016). Atmospheric and geometric modifications were excluded since the research region was cloud-free and the Landsat images were previously corrected geometrically. Radiometric correction is essential for mapping and monitoring because it accounts for variations in the geometry of the atmosphere and the sun. Because of minor fluctuation, radiometric corrections can often be neglected when the time period between images is short and obtained during the same season (Ban, 2016). According to (Song et al., 2001), radiometric modification is unnecessary when employing a classification, conducting post-classification on a single date, or categorizing composite imagery from several dates. A simple test using linear normalization was performed and, due to the minor disparity concerning the digital numbers and normalizing values, the correction was disregarded (Kalma, McVicar & McCabe, 2008).

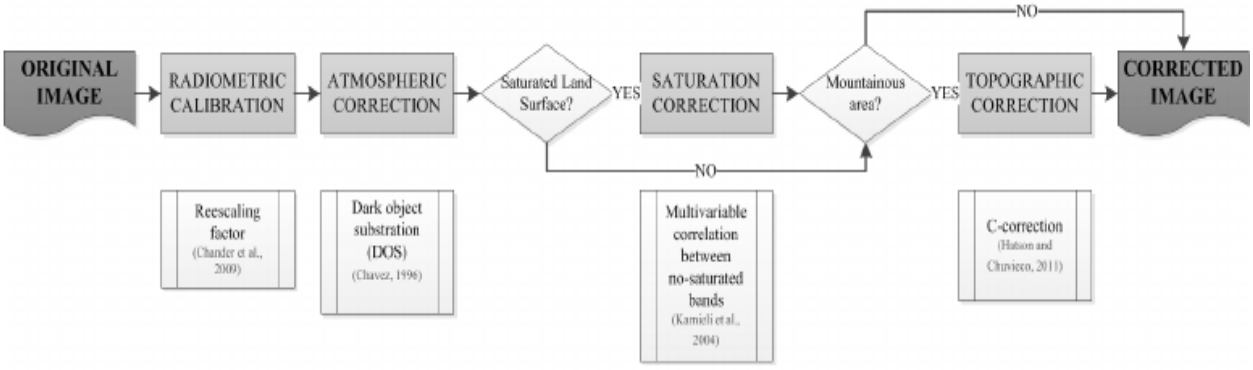

Figure 14 - Satellite Imagery Correction Workflow (Peterson, Sagan & Sloan, 2020)

The procedure is streamlined by disregarding any adjustments and working directly with the raw image. As a result, the procedure is expedited, which is important for efficiently mapping a region affected by a heatwave. The clipping of an area of about 500 km^2 from the original Landsat image is seen in Figure 15. Lyon and its surroundings were clipped from the Landsat imagery.

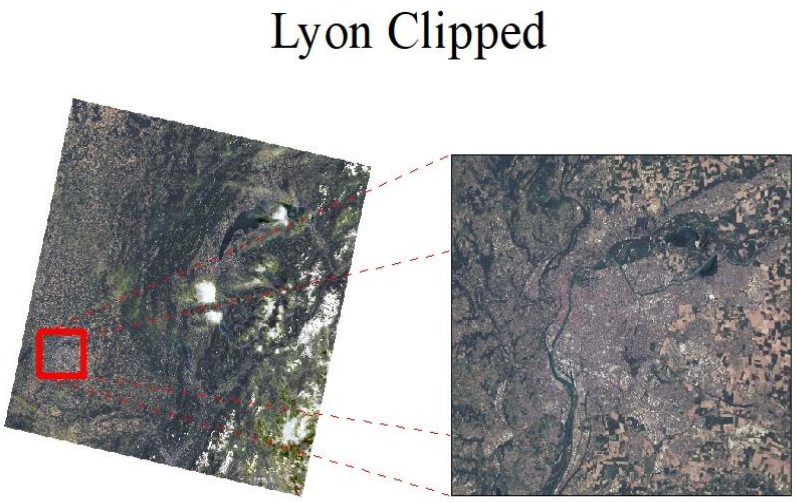

Figure 15 - Lyon Area Clipped from Landsat Image

4.2.1.1 Land Surface Temperature

Atmospheric conditions are usually measured using ground-based air temperature data from established meteorological stations. These stations, however, are frequently placed in sparsely populated areas. Due to the inadequacy of current networks for calculating temperature gradients, these data do not reflect the local heat experienced in residential contexts. Landsat satellite imagery 8 was chosen for this research because it provides the greatest spatial resolution thermal data currently accessible from orbit (Ban, 2016).

As a result, remote sensing satellites are increasingly being utilized to measure the thermal exposure of the population during a heatwave (Fabiani et al., 2019). Thermal data from satellites may be used to visualize the geographic gradient of the radiometric surface but not ambient temperature. Land surface temperature (LST) was determined using Landsat Operational Land Imager (OLI) and Thermal Infrared Sensor (TIRS) bands taken throughout the day when measurable heat island intensities are most significant. The TIRS thermal band has a spatial resolution of 30 m at the nadir, which is deemed sufficient for collecting complicated intra-urban surface temperature variations, allowing for a convincing and thorough study of the urban climate (Geletič, Lehnert & Dobrovolný, 2016). Two satellite images were taken on July 12, 2018, and August 4, 2018, at around 10:45 a.m. Universal Coordinated Time (UTC) was used in this study. Landsat revisit periods are on average 16 days, making it impossible to capture another image during this occurrence.

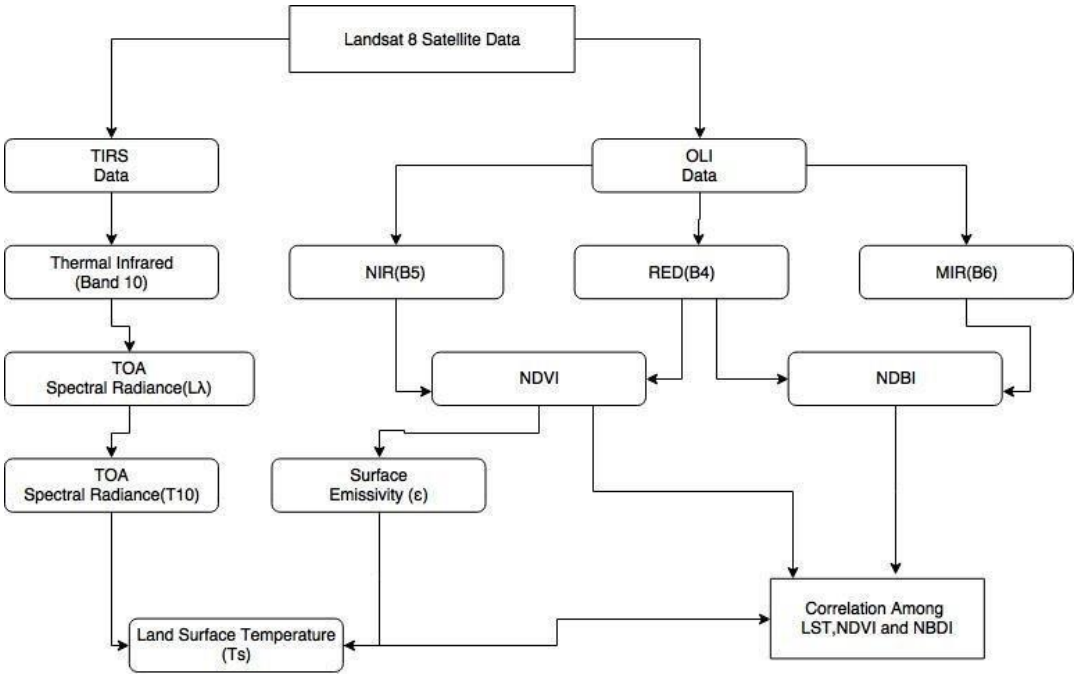

Figure 16 - Land Surface Temperature from Landsat 8 Satellite Data Workflow

The data from the thermal band imaging was calibrated in six steps. The brightness temperature was calculated after Band 10 digital numbers (DN) measurements were transformed to radiance. The Landsat-8 thermal infrared sensor (TIRS) and Landsat 8 Operational Land Imager (OLI) were employed in this research to convert known DNs into LST using a six-step procedure. To transform DN to Land Surface Temperature in Celsius, the following steps were performed:

1) Conversion of raw image into a spectral radiance by Equation (1) (Scarano and Sobrino, 2015).

$$L = = \frac{(L_{max} - L_{min})}{(DN_{max})} \times Band + L_{min} \text{ (1)}$$

Where,

L = Atmospheric SR in $watts/(m2 \times srad \times \mu m)$

L_{max} = Maximum SR Band

L_{min} = Minimum SR Band

$DN_{max} = Q_{cal\,max} - Q_{cal\,min}$ = maximum and minimum difference of sensor calibration

2) Equation (2) was used to convert reflectance to BT (NASA, 2017).

$$BT = \frac{K_2}{Ln\,i(\frac{K_1}{L_\lambda} + 1)} - 273.15 \text{ (2)}$$

Where,

K_2 and K_1 represents the band-specific thermal conversion constants

BT = Brightness temperature in Celsius

3) Eq. (3) was used for calculating NDVI.

$$NDVI = \frac{NIR\,(Band\,5) - R\,(Band\,4)}{NIR\,(Band\,5) + R\,(Band\,4)} \text{ (3)}$$

Where,

the Range: -1 < NDVI < + 1.

4) Proportion of Vegetation (PV) was assessed by Eq. (4) (Roy et al., 2014):

$$P_v = \left(\frac{NDVI - NDVI_{min}}{NDVI_{max} - NDVI_{min}}\right)^2 \text{ (4)}$$

5) Land Surface Emissivity (LSE) was calculated by Eq. (5) (Avdan and Jovanovska, 2016):

$$LSE = 0.004 \times P_v + 0.986 \text{ (5)}$$

6) LST was assessed in Celsius using the by Eq. (6) (Avdan and Jovanovska, 2016):

$$LST = \frac{BT}{\{1 + [\lambda BT/\rho] ln(LSE)\}} \text{ (6)}$$

Where λ is the wavelength of emitted radiance and ρ was calculated as (Eq. (12)):

$$\rho = h\frac{c}{\sigma} = 1.438 \times 10^{-2} mk\ ()$$

Where Boltzmann constant = $\sigma = 1.38 \times 10^{-23}\frac{J}{K}$, Planck's constant = $h = 6.626 \times 10^{-34}\ J\ s$, and velocity of light = $c = 2.998 \times 10^{8}\ m/s$ (Roy et al., 2014).

4.2.1.2 Reclassify LST

A classification approach is suitable when the objective is to accurately assign data to a defined, often limited collection of predefined classes or groups (Hussain et al., 2013). A data collection consisting of input variables and the dependent variable, generally known as the output variable, is utilized to train the model. Afterward, the model can be implemented to testing the dataset containing only the independent variables (Scott, Petropoulos, Moxley & Malcolm, 2014). Based on the standard deviation from the mean, the LST values were divided into four categories, computed by using standard deviation analysis to determine the relative deviation of the data points from the mean. If the data points are further from the mean, the variance within the dataset is more relevant; as a result, the larger the standard deviation, the more widely spread the data is (Vargo, Habeeb & Stone, 2013). The following formula is used to get the standard deviation:

$$\frac{\sqrt{\sum_{i=1}^{n}(xi - \bar{x})^2}}{n-1}$$

where:

xi=Value of the *ith* point in the data set

$\bar{x}$=The mean value of the data set

n=The number of data points in the data set

Figure 17 displays the standard deviation around the mean over a normal distribution. The data represents land surface temperature in which the high values (right tail) are of much more importance than the rest of the data since LST is correlated with heatwave intensity. The research aims to identify the areas within the city that are more affected by heatwaves than their surroundings. In that case, it was decided to classify 50% of the values associated with relatively low LST values as "Low." The Low class would equate to all data that is equal to the mean or lower. The classification is more sensitive to the higher values since it will have three classes explaining 50% of the data above the mean. The mean to one standard deviation data is classified as "Moderate" accounting for 34.1% of the data. Next, the values from one standard deviation to two standard deviations are classified as "High" which equates to 13.6% of the data. The last class was categorized as "Extreme" which are all the values over two standard deviations and accounted for only 2.2% of the data. The Extreme class only includes the high LST values compared to the rest of the city and was purposely chosen to include limited options for emergency services and decision-makers to prioritize allocating limited resources on the ground to the most affected blocks.

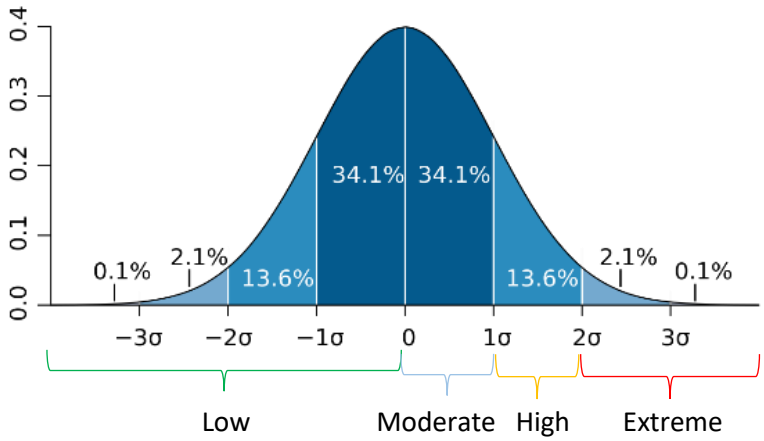

Figure 17 - Standard Deviation of Normal Distribution

The trained model in highlighting heatwave hotspots is designed to work in any urban environment. The classifying of values based on standard deviation makes the model more robust when applying to different cities. The LST values change when dealing with different geographic regions, and the transformation to classes based on the standard distribution makes the classification based on relative values rather than absolute. For instance, 30°C might be considered Extreme in specific locations, whereas it might be an average summer day in other places. Ignoring the absolute value and focusing on the relative differences over an area eliminates training the model to the local environment parameters, making it more applicable to other geographic regions.

4.2.1.3 Optical Bands

Numerous spectral indices may be used to analyze various variables, such as water resources, vegetation, soil and snow (Zhao et al., 2019). Landsat satellite imagery facilitates a variety of operations on its bands, the result of which may be converted to a spectral index. Spectral indices distill multi-spectral satellite imagery down to a single element, enabling the observation of pixel values over time (Li & Guo, 2016). Furthermore, spectral indices exceed individual bands by amplifying beneficial features (ex. land use and cover change) while reducing unwanted properties like atmospheric and topographic noise (Fu & Weng, 2016). Spectral indices are frequently used in remote sensing applications, and their use in evaluating various geographical problems has been thoroughly established. The objective of this study was to assess the most commonly used indicators to ascertain which ones had the strongest correlation with LST. In all, 24 distinct band combinations were evaluated in the machine learning model to determine their predictive ability for LST (Table 2).

Table 2 – Satellite Imagery Derived Bands/Indices

Bands/Indices	Wavelength (micrometers)	Resolution (meters)	Applications
Band 2 - Blue	0.45-0.51	30	Assessment of vegetation vigour
Band 3 - Green	0.53-0.59	30	Chlorophyll absorption for vegetation differentiation
Band 4 - Red	0.64-0.67	30	Biomass surveys and delineation of water bodies
Band 5 - Near Infrared (NIR)	0.85-0.88	30	Vegetation and soil moisture measurements
Band 6 - SWIR 1	1.57-1.65	30	Crop monitoring
Band 7 - SWIR 2	2.11-2.29	30	Hydrothermal mapping
Band 10 - Thermal Infrared (TIRS)	10.6-11.19	100 rescaled to 30	Land Surface Temperature (LST)
Natural Composite	-	30	Natural color composition of RGB bands
Enhanced Vegetation Index (EVI)	-	30	'Optimized' vegetation index designed to enhance the vegetation signal with improved sensitivity in high biomass regions
Modified Normalized Difference Water Index (MNDWI)	-	30	Uses green and SWIR bands for the enhancement of open water features
Built-up Index (BU)	-	30	Index for analysis of urban pattern using NDBI and NDVI
Normalized Difference Built-up Index (NDBI)	-	30	Uses the NIR and SWIR bands to emphasize manufactured built-up areas
Normalized Difference Vegetation Index (NDVI)	-	30	Quantify of vegetation greenness (vegetation density)
Normalize Difference Water Index (NDWI)	-	30	Water bodies analysis
Adjusted Vegetation Index (SAVI)	-	30	Vegetation index that minimizes soil brightness influences
Modified Soil Adjusted Vegetation Index (MSAVI2)	-	30	Minimizes the effect of bare soil on the SAVI
Perpendicular Vegetation Index (PVI)	-	30	Vegetation index sensitive to atmospheric variations
Normalized Difference Moisture Index (NDMI)	-	30	Sensitive to the moisture levels in vegetation
Agriculture Index	-	30	Emphasizes agricultural areas
Healthy Vegetation Index	-	30	More sensitivity to type of vegetation
Atmosphere Index	-	30	Index that minimizes the effect of the atmosphere
Infrared Index	-	30	High sensitivity to vegetation

Natural No Atmosphere Index	-	30	Natural colors minimizing the effects of the atmosphere
Vegetation Analysis	-	30	Vegetation index that emphasizes on different forms of vegetation
Waterland index	-	30	Index that distinguishes the boundary of water/land.

4.2.2 Auxiliary Data

The majority of supplementary data acquired from Lyon's spatial respiratory platform was vector-based and thus easily incorporated into the model. The data were projected to the standard projection, and descriptive statistics were used to evaluate the data distribution and account for outliers and null values. After cleaning the raw data, all the feature information was compiled into a single file. Continuous data from emission measurements were subjected to zonal statistics to determine the mean for each block. Due to the sensitive nature of the data, most of the socio-demographic data was already stored in IRIS blocks.

In comparison, the sum of discrete data was computed by adding the counts of the data points within each IRIS. All variables were then normalized on a 0 to 1 scale to guarantee consistency in the machine learning models. Table 3 contains a list of the data that were used to create the model prediction. The data is collected from various local and national government organizations and is utilized in research as predictions for environmental and public health applications.

Table 3 – List of Auxiliary Factors

		Data	Year	Source
	Amenities	Public Fountains Library School High School Higher Education Number of Parks Area of Green Areas Canopy index -ratio between tree stratum and area	2016	Digital Innovation and Information Systems Department (DINSI)
	Landuse (Percentage of Total)	Agriculture Forest Industrial Road Scrub_Grassland Urban_Continuious Urban_Discontinuious Urban_GreenAreas Proximity to Waterbodies	2017	Urban Development and Living Environment Delegation (DUCV)
	Emissions	Sulfur Dioxide (SO2) Nitrogen Dioxide (NO2) Benzene (C6H6) Ammonia (NH3) Carbon Monoxide (CO) Overall Air Quality	2019	CITEPA - https://www.citepa.org/en/data/
	Energy Consumption	Electricity and Gas Consumption (MWh)	2014	Territorial Strategies and Urban Policies Department (STPU) / Energy Department
	Topographic	DEM	2010	Space Shuttle Radar Topography Mission (SRTM)
Socio-Demographic	Population	Total Population (Total_Pop_P) Population Under 14 (Pop_U_14_P) Population Under 19 (Pop_U19_P) Population Between 20 - 64 (Pop_20_64_P) Population Over 65 (Pop_O_65_P) Male Population (Male_P) Female Population (Female_P)	2013	Institut national de la statistique et des études économiques (INSEE)
	Occupation (Percent of Total)	Farming (Farming_P) Craftsmen (Craftsmen_P) Managers and Higher Positions Managers and Higher Positiions (Managers_Higher_P) Intermediate Jobs (Intermediate_P) Employee (Employees_P) Low Skilled Jobs (Workers_P) Retired (Retired_P) Without Profession (WO_profession_P)	2013	
	Population Status (Percentage	French National (French_P) Foreign Population (Foreign_P) Immigrants Population (Immigrants_P) Residenting Population (Household_Pop_P) Nonresidenting Population (Pop_No_Household_P)	2013	

4.3 Machine Learning Models

Machine learning (ML) is increasingly impacting society, assisted by significant improvements in extensive data, computer efficiency, conveniently accessible data storage, and continuous connectivity. ML approaches are quickly being employed in Earth and Environmental System modeling research due to the growing availability of large data sets, accessibility of computation, and enhanced machine learning algorithms. Climate modeling (Geletič, Lehnert & Dobrovolný, 2016; Gosling, McGregor & Páldy, 2007; Zhao et al., 2019) and remote sensing (Chen et al., 2016; Heung et al., 2016; Peterson, Sagan & Sloan, 2020; Zhou et al., 2020) are all well-studied areas in Earth Science that utilize machine learning applications. Machine learning-based techniques may bring up viable, alternative routes for developing knowledge about urban temperature modeling. In numerous Earth Sciences applications, machine learning models have consistently outperformed conventional predictive models and provided broader flexible solutions to unanticipated scenarios (Bakar, Pradhan, Lay & Abdullahi, 2016; Huang et al., 2015; Shatnawi & Abu Qdais, 2019; Zhang & Sun, 2019). ML techniques are entirely or partially automated methods for inferring facts without establishing certain prior assumptions.

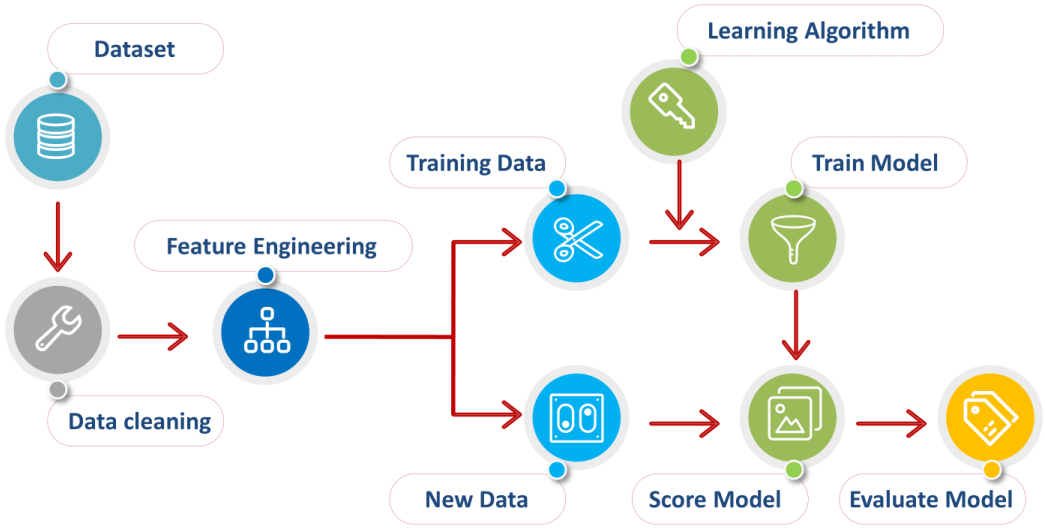

Figure 18 - Machine Learning Workflow (Pant, 2019)

The most often used machine learning algorithms in research include various learners from linear regression, decision trees, random forests, KNN, logistic regression, and gradient boosting domains (Heung et al., 2016; Modaresi, Araghinejad & Ebrahimi, 2018; Saputra & Lee, 2019; Were, Bui, Dick & Singh, 2015; Zhou et al., 2020). The supervised machine learning methods begin with a dependent variable (target) that will be forecasted using a set of predictors (independent variables). Next, a model is defined by converting inputs to desired outputs utilizing a collection of variables (Zhou et al., 2020). Finally, the algorithm is trained until it achieves the desired degree of accuracy when applied to the training data (Heung et al., 2016). The thirteen machine techniques used to estimate the LST are listed in Table 4.

Table 4 - Machine Learning Models Used for Prediction of Heatwaves

Machine Learning Algorithms	Algorithm Group
Logistic Regression (LR)	Linear Models
Linear Discriminant Analysis (LDA)	
Support Vector Machines (SVM)	Support Vector Machines
Linear Support vector Machines (LSVM)	
Gaussian Naive Bayes (NB)	Naive Bayes
AdaBoost (ADA)	Ensemble Methods
Random Forest (RF)	
Gradient Boosting Classifier (GBC)	
Extreme Gradient Boosting (XGB)	
K-Nearest Neighbors (KNN)	K-Nearest Neighbors
Multi-Layer Perceptron Classifier (MLP)	Neural Network
Classification and Regression Trees (CART)	Decision Tree
Decision Tree (Tree)	

4.3.1 Model Evaluation

Classification is the process of categorizing a set of data. Machine learning processes begin by defining the problem, acquiring data and cleaning it, integrating key feature variables, training the model, evaluating overall performance, and refining it using an appropriate cost function. A confusion matrix is a quantitative assessment of the accuracy of a classification algorithm. Every element in a confusion matrix reflects how many classification predictions a model made correctly or incorrectly (Pant, 2019).

Table 5 - Confusion Matrix (Pant, 2019)

		Predicted Class	
		Positive	**Negative**
Actual Class	**Positive**	True Positives (TP)	False Negatives (FN)
	Negative	False Positives (FP)	True Negatives (TN)

True Positive (TP): represent the number of predictions wherein the algorithm correctly predicts the presence of a positive class.

True Negative (TN): This statistic reflects the number of predictions in which the algorithm classified the negative class correctly as negative.

False Positive (FP): This terminology represents the number of predictions produced by the algorithm that are incorrectly classified as positive.

False Negative (FN): The number of classification predictions in which the positive class is incorrectly classified as negative.

Generally, it is better to use a confusion matrix as the assessment metric for a classification machine learning model because the confusion matrix includes many of the most frequently employed performance metrics (Pant, 2019). Thus, it gives a precise yet valuable gauge for the performance of the model. The following statistics summarizes the most commonly used model performance metrics:

Accuracy: This parameter reflects the model's overall performance, calculated as the proportion of total observations correctly classified by the model. Accuracy is evaluated using the following equation: (TN+TP)/(TN+TP+FN+FP).

Precision: This statistic measures the ratio of positive predictions within a positive class. Precision is computed using the following formula: TP/(FP+TP).

Recall: This measure reflects the fraction of all positive samples correctly recognized as positive by the algorithm. The recall is computed using the subsequent formula: TP/(FN+TP).

F1-score: This measure incorporates precision and recall in a single value. In mathematics, it is also the harmonic mean of precision and recall. It may be computed as follows:

$$F_1\text{−score} = 2 \times \frac{\text{Precision} \times \text{Recall}}{\text{Precision} + \text{Recall}} = \frac{2\text{TP}}{2\text{TP} + \text{FP} + \text{FN}}$$

4.2.1 Feature Importance

The concept "feature importance" refers to a method in which input qualities are assigned a value based on their predictive capacity for a dependent variable. For example, linear model coefficients, statistical correlation coefficients, and permutation importance scores are all types of feature importance scores that can be computed (Zien, Krämer, Sonnenburg & Rätsch, 2009). Feature importance scores are critical in predictive modeling because they provide insights from data, insights into the model, and the foundation for feature selection and dimension reduction, enhancing the efficacy and efficiency for a predictive model upon a particular topic (Vargo, Habeeb & Stone, 2013). Fundamentally, machine learning algorithms evaluate the relative significance of variables, which can shed light on their predictive ability.

The issue is that when a classifier is developed with such a large amount of data points, it could also learn from noise and inaccuracies. As a result, the model exhibits an excessive amount of flexibility when replicating the input data, a phenomenon referred to as overfitting (Zien, Krämer, Sonnenburg & Rätsch, 2009). Overfitting is a problem that should be acknowledged whenever a model's performance is increased. Seventy factors are evaluated in this study to determine which are the most important on the model’s performance. In addition, the k-fold cross-validation method was used to investigate the model's validity and avoid overfitting the model with the optimal number of features.

Also, Principal Component Analysis (PCA) was utilized to determine which combination of elements contributed to cohesiveness. PCA is a dimensionality-reduction approach that is commonly applied to reduce the size of large data sets by condensing a collection of factors into a smaller subset that preserves the majority of the data contained in the larger set. While reducing the number of components in a data set will consistently lower accuracy, the objective of dimensionality reduction would be to trade off some precision for simplicity. PCA lowers the number of factors by encapsulating the information in new "components." Because the additional variables are irrelevant to this research and the objective is to determine which variables contribute to the model, the new "components" can be examined to determine the contributions of all the raw variables. Assessing the factors' effect on the new components can aid in deciphering patterns and determining which variables contribute to the cohesiveness of the model. In addition, this assessment will assist in selecting the most influential elements and determining which components function best in conjunction (Fauvel, Chanussot & Benediktsson, 2009).

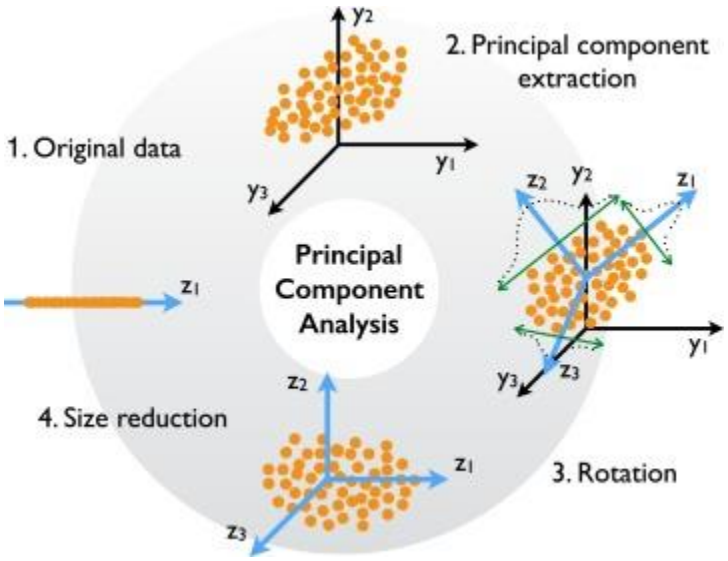

Figure 19 - Principal Component Analysis Steps (Fauvel, Chanussot & Benediktsson, 2009)

The SHAP python package was used to determine the significance of features. SHAP's objective is to quantify the effect of each variable on the prediction of an event (Nandlall & Millard, 2020). In the SHAP explanation technique, Shapley values are calculated using coalitional game theory (Tao, Chen, Xu & Zhu, 2011). The principle behind the relevance of SHAP characteristics is simple: It is vital to have Shapley values that are high in absolute terms. The overall feature importance is obtained by adding all the comparative Shapley scores for each item in the data (Nandlall & Millard, 2020).

SHAP is an attribute characterization metric based on the magnitude of attribute representations. The increase in the model's error rate due to permuting the feature's values, that weakens the relation among the feature and the actual result, is calculated using SHAP factor significance, which is a replacement for permutation feature importance. There is a substantial difference between the two feature importance metrics: The model's performance degradation decides the importance of permutation characteristics. The significance of each variable is then shown in declining order of importance—the predictor importance graph aids in model evaluation by emphasizing each predictor's relative importance. Given the relative nature of the data, all variables are reflected by a value of 1.0. A predictor's significance does not influence

the model's accuracy. It refers to the proportional importance of each predictor in making a prediction, not to the prediction's accuracy (Nandlall & Millard, 2020).

4.4 Multi-Criteria Analysis and Production of Heatwave Risk Map

A Multi-Criteria Analysis (MCA) identifies and examines several alternatives by assessing their impact, effectiveness, and implications. MCA is a systematic approach that enables difficult choices to be explored per predefined criteria and objectives (Deng, 2015). MCA is particularly well-suited for resolving difficult, complex problems that include many and conflicting goals and objectives. It permits the selection of a specific best option as well as the ranking of possible alternatives. In addition, MCA enables the identification of trade-offs between various methods (Farhan, Pattipati, Wang & Luh, 2015). MCA was used to create the Heatwave Impact Risk Map for this project. MCA primarily utilized two sources of data that were weighted equally based on Buscail, Upegui & Viel's (2012) workflow for heatwave health risk mapping. The researchers weighted the following four factors equally (25%); Exposure, Vulnerability, Hazard and Exposure & Vulnerability combined index. The Hazard Map, which is constructed entirely from reclassified LST measurements, depicts all of the IRIS blocks of Lyon based purely on the temperature. The higher the temperature, the more hazardous the circumstance.

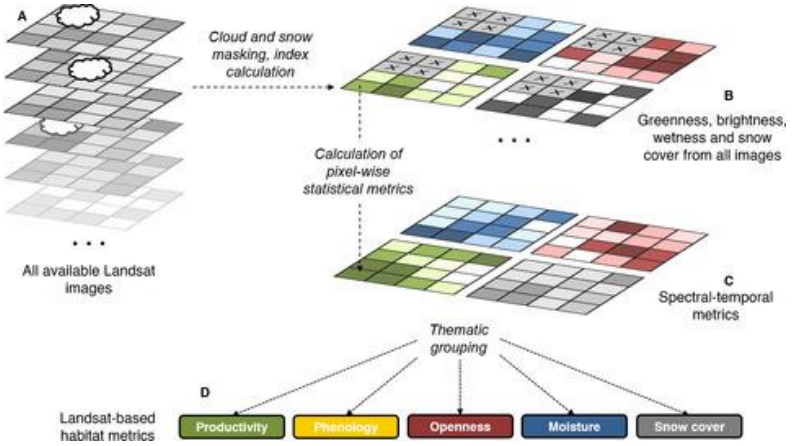

Figure 20 - Landsat Spectral Index Steps

The Vulnerability Map is based on numerous variables that have contributed to the vulnerability of the most susceptible population. The factors were chosen based on published research and empirical data from prior heatwaves, demonstrating a link between the variables utilized and the people most affected by heatwaves (Farhan, Pattipati, Wang & Luh, 2015; Gosling, McGregor & Páldy, 2007). For example, the term "extreme age" refers to the percentage of the population under the age of five and above the age of 65. The term "population density" refers to the amount of people living in a specific area (IRIS boundary). During heatwaves, low-income population is disproportionately affected. The low-income population is categorized according to education, the percentage of low-skilled occupations, the percentage of immigrants, the number of social service outposts and average household income situated in an IRIS, with higher scores corresponding to lower-income IRIS zones. The unemployment rate relates to the percentage of the IRIS population that is unemployed. Each IRIS is evaluated according to its appropriateness on a

scale of 1 to 10. Then combined, they generate the vulnerability map. The final heatwave impact risk map is constructed using the MCA of hazard and vulnerability maps, as seen in Figure 21.

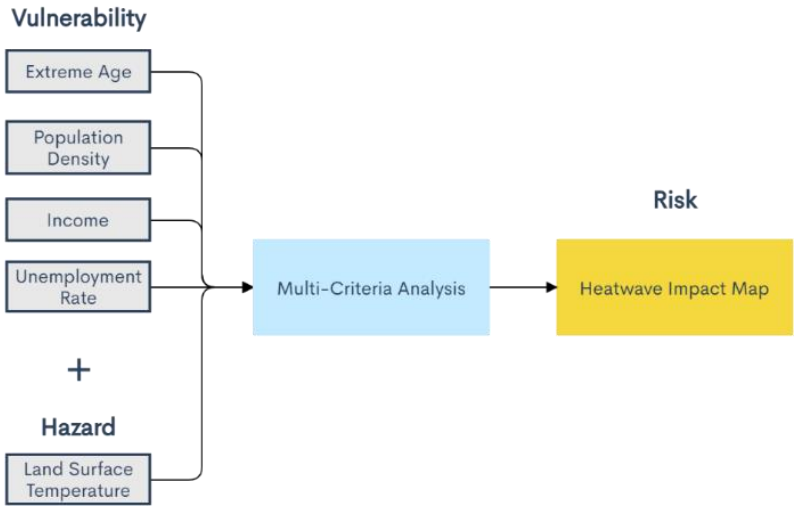

Figure 21 - Multi-Criteria Analysis Workflow

4.4.1 Hazard

Since their inception as a strategy for measuring health implications of traffic-related air quality, hazard maps have been widely adopted as a method for classifying the spatial variation of environmental dangers, such as heatwaves, due to the close relationship between temperatures and land cover types. Hazard maps make use of geographic predictor variables to estimate exposure levels for a given population. The hazard map is half of the Heatwave risk map and is based entirely on land surface temperature.

4.4.2 Vulnerability

The factors considered in the vulnerability analysis have demonstrated a high correlation between heat and health outcomes in the literature (Farhan, Pattipati, Wang & Luh, 2015; Gosling, McGregor & Páldy, 2007). The geographical distribution of the IRIS-required vulnerability characteristics was established using census data. Socioeconomic status was determined by combining social isolation, deprivation, and a low-level education. Each IRIS received a score derived from the Townsend score (one of the most widely used deprivation indices). Vulnerability indices for IRIS boundaries with less than 100 residents were set to zero since a low population density indicates low overall risk. The low educational level measure was calculated by measuring the percentage of the population without a high school diploma. Population and land areas were utilized to get the population density per IRIS (Inhabitants Per Square Meter). The combination of the four components resulted in the vulnerability map, which weighed in at 50% for the final heatwave risk map.

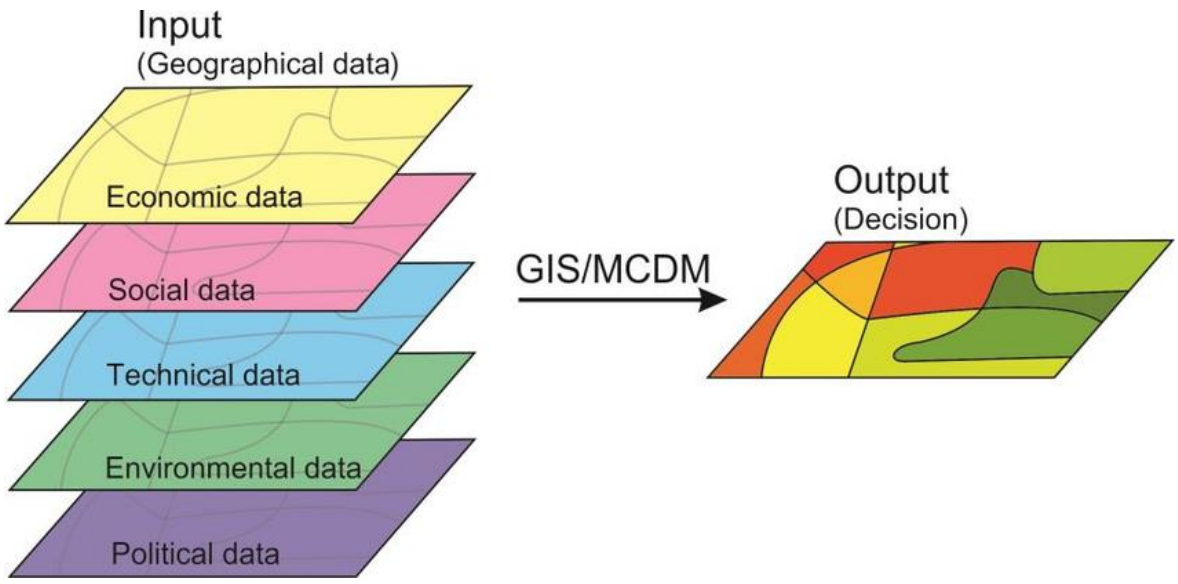

Figure 22 - Using GIS to Convert of Geographic data to Final Product Illustration (Deng, 2015)

4.4.3 Mapping

A heatwave health risk index of one to ten was created by combining the four vulnerability factors (each weighted 25%) for a total of 50% of the overall weight, and the hazard factor weighted 50% based on . Buscail, Upegui & Viel's (2012) framework for heatwave health risk mapping. Choropleth maps were used to illustrate geographical differences in hazard, vulnerability, and risk indices. The index values (1–10) were classified into four categories to indicate the growing dangers of heatwaves (Low, Moderate, High, and Extreme). The models were generated and analyzed using ArcGIS and Python.

4.5 Simulations of Heatwave Mitigation Strategies

A large-scale analysis is conducted after identifying the IRIS with the highest heatwave risk. Due to the small number of IRIS bounds, computationally intensive lidar data will be used to more accurately identify IRIS characteristics. Lidar data provided additional information on the most impacted IRIS, which can then be used to model the effect of greening the IRIS on the entire heatwave risk. The overall process depicted in Figure 23 illustrates the various analyses provided by the lidar data and how the result will be incorporated into the model to anticipate future mitigation possibilities. The three-dimensional lidar data will give critical information on the structure, vegetation, and unused barren/impermeable land. The calculation will then be used to simulate changing the landscape by greening 25%, 50%, and 75% of the available land and observing the effect on temperature. Two elements contribute to the area's greening:

1. By increasing the proportion of green roofs on available buildings' roofs.
2. By increasing the proportion of vegetation on available barren/impermeable land.

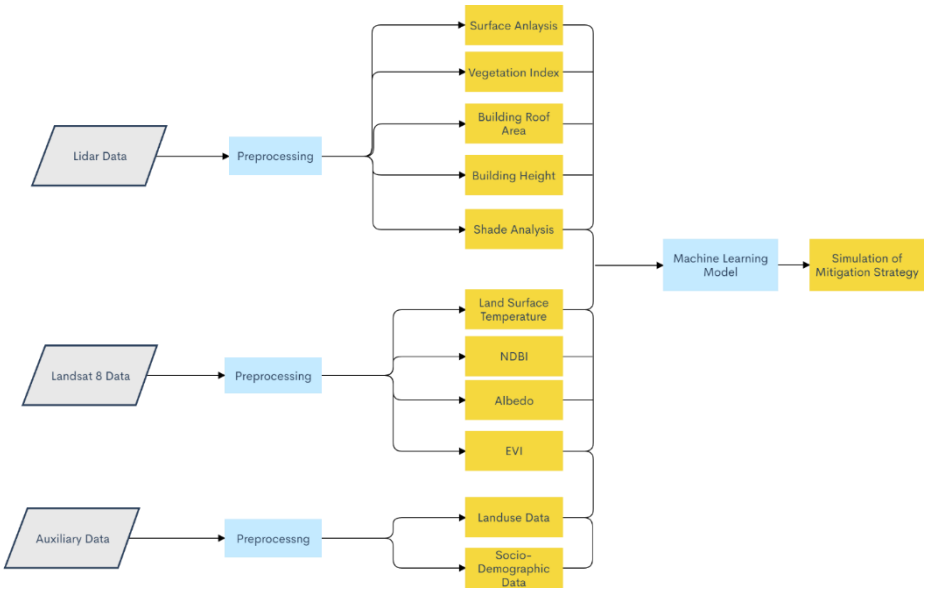

Figure 23 - Greening Simulation Workflow

The link between the many components that comprise the final model will be examined to ascertain the effect of varying the land use pixel values. After generating the correlation, the impact of greening the IRIS in various circumstances will be calculated. The new values are then put into the machine learning model, which is used to forecast heatwave risk under different scenario settings. This approach offers a rapid estimate of the amount of greening necessary to lower the temperature considerably. There is now much more sophisticated customized software available that combines many factors like surface type, soil time, meteorological data, urban architecture, and wind patterns to produce a significantly more realistic simulation. However, such programs take a significant amount of data and time to process, which is not always advantageous during an emergency hazard event. Apart from reducing temperature extremes and urban heat islands, urban greening reduces air and noise pollution, absorbs rainwater that would otherwise cause flooding (Demuzere et al., 2014; Deng, 2015; Santamouris & Osmond, 2020; Uyar, 2017). It also provides habitat for native species and has been shown to boost morale in those who see it, calming traffic and reducing urban crime (Santamouris & Osmond, 2020).

4.5.1 Light Detection and Ranging (Lidar) Data

Lidar is a process of remote sensing that utilizes a laser pulse to measure intervals (variable distances) to the Earth. When such light pulses are combined with appropriate data acquired by the airborne devices, precise three-dimensional measurements about the shape and properties of the Earth are obtained (Corte et al., 2020). Lidar information was used to achieve a more detailed view of the most affected IRIS limits and simulate urban greening scenarios by adding green roofs and enhanced vegetation throughout the block. The method for integrating lidar data into model-compatible data is depicted in Figure 24. After incorporating the new information from the lidar data into the model, future situations can be simulated. Essential factors determined in the preceding phase can then be modified on the various greening scenarios

to observe how it affects the entire IRIS block. The effects of greening potential areas by 25%, 50%, and 75% were investigated by examining their impacts on the model's factors. After generating the association between altering land use, the pixel values were translated in the simulation to see the effect on temperature.

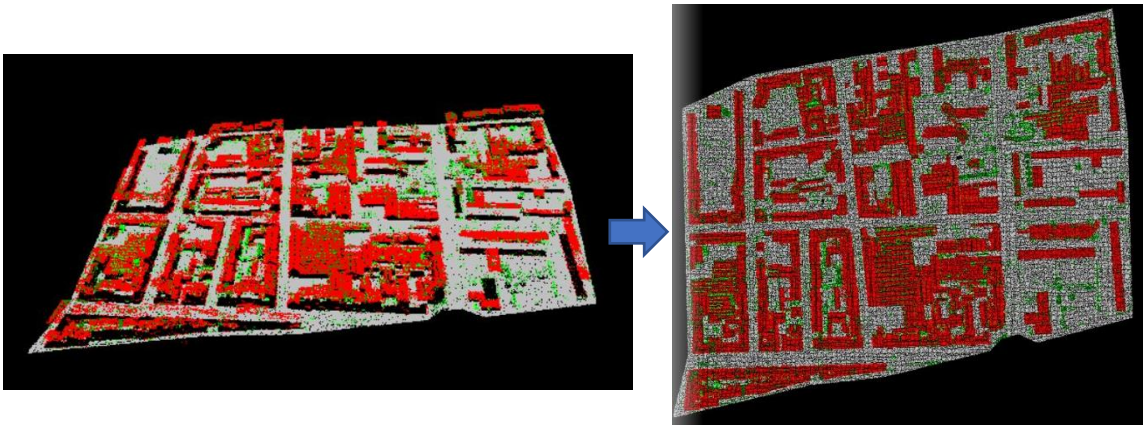

Figure 24 - Conversion of Lidar 3D to Model Compatiable Data

Three-dimensional urban morphology parameters were constructed to establish the effect of the built environment on the UHI model. Separating urban structure and surface points from many other point clouds was the first step, followed by generating a digital surface model (DSM) by using a linear interpolation approach by means of a triangulated irregular network (TIN) (Corte et al., 2020). Splitting the ground point class from other point classes resulted in creating a terrain model (DTM). Next, the building height was generated by the subtracting DTM from the DSM (Building Height = DSM – DTM). Finally, building heights were transformed to a raster of building heights (Rodrigues et al., 2019). The same steps were done for vegetation, but instead of building points, vegetation was separated from the point cloud. Most of the processing steps were performed within ArcMap program utilizing a custom tool from LAStools (https://rapidlasso.com/lastools/).

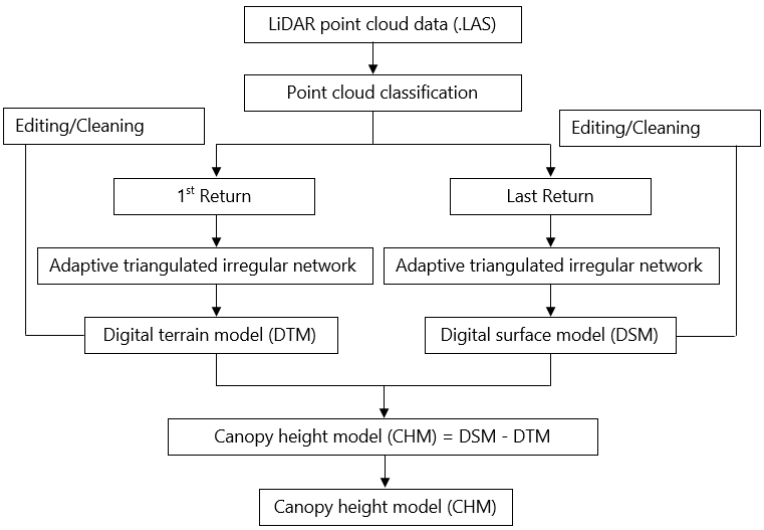

Figure 25 - Lidar Processing Steps

Roof Index of Structures:

The building roof index was calculated as the total of the roof areas of not vegetated buildings. This index was determined using the DSM.

Index of Vegetation:

Lidar data includes the classification of three types of vegetation based on height. Lidar data can detect the difference between low, medium, and high vegetation. The IRIS's total vegetation cover was determined by adding all the vegetation pixels within an IRIS. The vegetation was rasterized into two classes: vegetation on building roofs and vegetation growing on the ground.

Analysis of Shades:

The DSM was calculated using Lidar data, and then shadow analysis was used to determine the percentage of the IRIS that is shaded during a heatwave. The shade study will demonstrate the consequences of increasing the density of high vegetation in various scenarios. Generally, previous research has relied on field tests to determine how shade enhances thermal comfort. For example, 93 percent of individuals visiting a public square in July in Taiwan chose to remain under shade trees or in building shade, demonstrating the critical nature of shade in outdoor areas (Lin, Matzarakis & Hwang, 2010). In addition, greening barren areas have the indirect consequence of making them more accessible and bearable during a heatwave and could provide refuge from direct exposure to the sun.

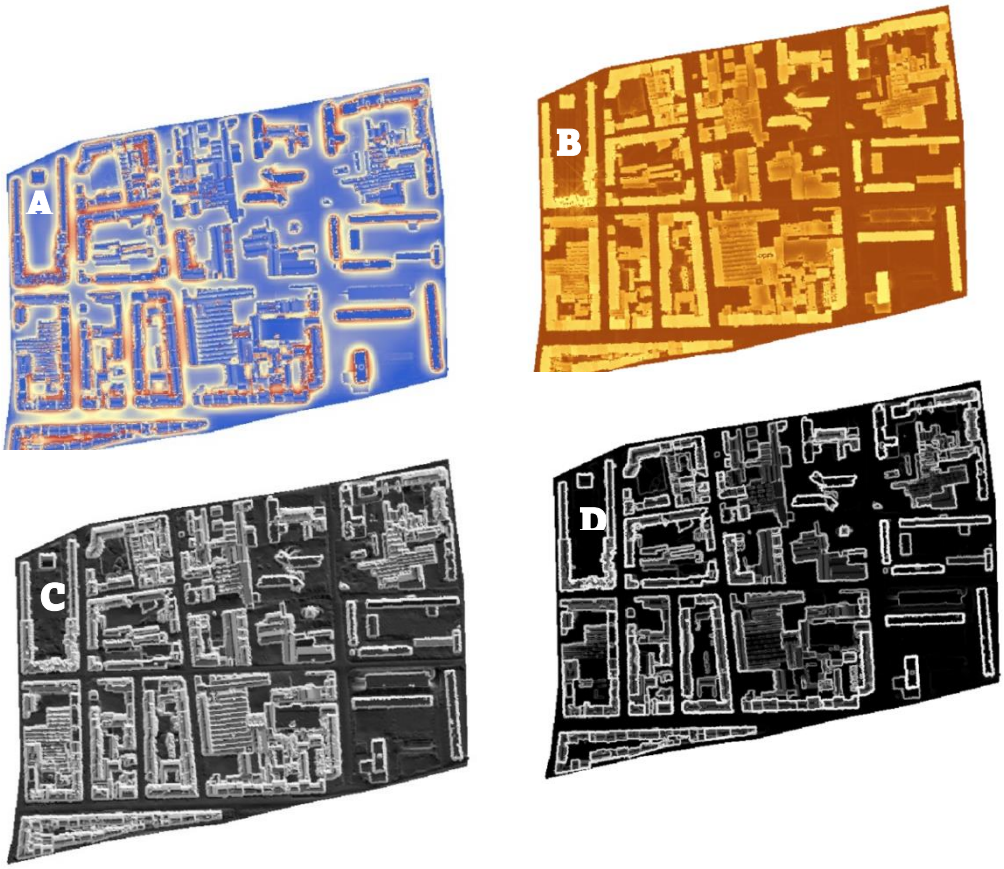

Figure 26 - Lidar Derived Anlaysis (A) Sky View Factor (B) Ground Isolation (C) Building Density (D) Building Edge Detection

4.5.2 Scenario Simulation

The total usable roof area of buildings is estimated using the DSM of buildings. The 2D roof of each structure is then retrieved using statistical means by separating pixels with a relatively consistent height +- 2 m and the area calculated. As a result, the rasterized rooftop structures are isolated from the rest of the image. A similar procedure is followed for vegetation on rooftops, which is subsequently removed from the total rooftop area available. This approach will eventually provide an estimate of the total area accessible for green roof development.

The different ways green infrastructure can be incorporated within an urban environment can be seen in Figure 27. Integrating vegetation in an urban environment requires intensive local knowledge of the urban morphology and flora species selection at particular conditions (Demuzere et al., 2014; Santamouris & Osmond, 2020). One significant limitation of this study was grouping all greening interventions as the same value without any regard to any detail on the type, design, scale, and species used. Therefore, this research will not look at various ways of incorporating green infrastructure but rather the number of areas converted from grey infrastructure to green. Urban green simulations will adjust pixel values of redesigned roofs in the impact variables due to changes in roof materials. This in essense will incorporate the positive effects of green and cool roofs relative to temperature. As a result, the parameter pixel size should be as small as possible to make these adjustments more precisely of the available roof area. The inclusion of more green spaces will, in essence, change the various factors used in the model; for instance, it will increase NDVI and Albedo while decreasing the NDBI.

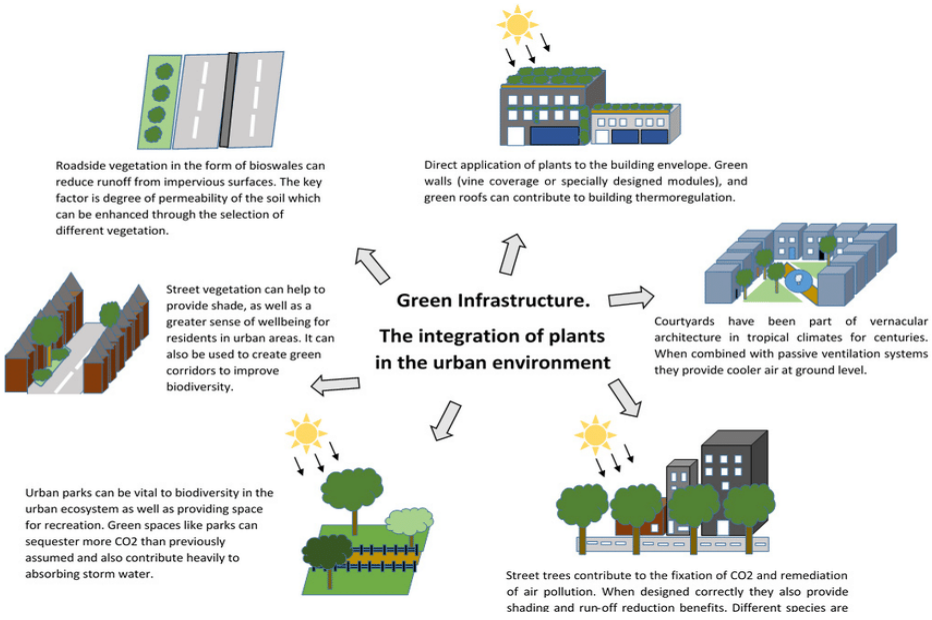

Figure 27 - Green Infrastructure Integration (Wootton-Beard et al., 2016)

CHAPTER 5: RESULTS AND DISCUSSION

5.1 Model Evaluation

5.1.1 All Models

The accuracy results for the thirteen machine learning algorithms are depicted in Figure 28. Most models performed between 70% and 90%, except for AdaBoost Classifier, which performed poorly. AdaBoost Classifier is similar to the best performing classifiers random forests and XGBoost. Ensemble learning algorithm combines multiple base learners' predictions to produce a single, aggregate estimate for each input (Zhou et al., 2020). This approach allows it to discover more intricate correlations between the training set's attributes and targets. AdaBoost algorithm might have performed poorly due to irrelevant features included in the model. Two parameters included in the model had little effect on the overall model but were critical for differentiating the "Extreme" class, which was necessary for classifying the most impacted locations. Models constructed using linear regression, logistic regression, support vector machine (SVM), naive bayes, k-nearest neighbors (KNN), and neural networks all performed well, with accuracies ranging from 70% to 80%. The models demonstrated the most significant degree of confusion between the intermediate classes. Confusion may arise due to the models being calibrated to be extremely sensitive to the Extreme class, resulting in the incorrect classification of the intermediate classes. The neural network model was expected to be one of the best performers; however, because neural networks require a vast dataset to train effectively, the results were not as anticipated. The two Landsat images provided insufficient data to train the link between input factors and output prediction adequately.

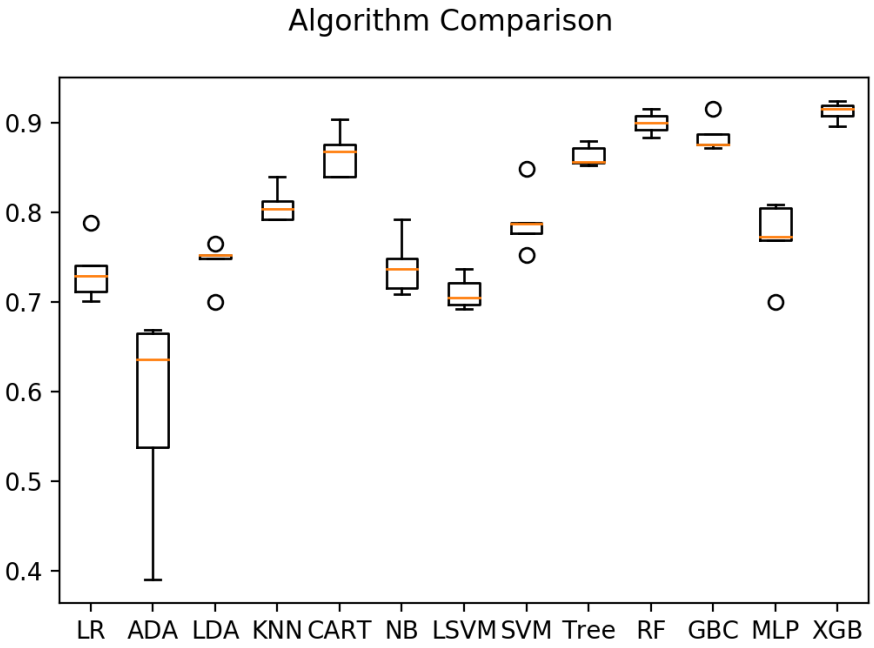

Figure 28 - Machine Learning Model Accuracy for Predicting Heatwave Hotspots

The decision tree and ensemble learning algorithms had the highest accuracy scores, ranging around 90%. Tree-based algorithms facilitate predictions with high accuracy, consistency, and interpretability. In comparison to linear models, tree-based and ensemble algorithms can accurately map nonlinear relationships. Ensemble models are a subset of decision trees. Random forest and gradient boosting models

(CART, XGB, GBC) use ensemble learning. Random forest uses a group of decision trees to categorize new objects based on their properties; each tree provides a classification, and the one with the most votes win. Gradient boosting algorithms employs a collection of learning algorithms that aggregate the predictions of many base estimators to enhance resilience over a single estimator. It takes many weak or mediocre predictors and combines them to create a strong predictor (Zhou et al., 2020). The models that utilized ensemble methods had the best accuracy, which is consistent with the literature.

5.1.2 Best Performing Model

The best performing model was the XGBoost, with an accuracy of 94%. Gradient boosting (GB) algorithms are highly effective classifiers/regressors that work exceptionally well on structured data, and the XGBoost module is an exemplary implementation of this approach. XGBoost has several speed advancements that enable rapid training of a high-performing model. As a result, XGBoost is widely used, and outputs have won many structured dataset competitions (Zhou et al., 2020).

The accuracy results of the model, based on the testing dataset (25% of data), are shown in Table 6. The XGBoost performed well in grouping all classes with accuracies above 88% and perfectly predicting the Extreme class, which signifies the most stricken areas due to heatwaves. The model was customized to give more weight to the Extreme class by changing the weights assigned to the different categories. Then the precision, the proportion of accurately projected positive observations to the overall sum of predict positive observations, and the recall, which is the proportion of accurately forecasted positive observations to all observations in the actual class, were both high (Pant, 2019). Therefore, the model did not wrongly overpredict the Extreme class. F1 Score is the weighted average of Precision and Recall, thus considering false positives and false negatives.

Table 6 - Accuracy Statistics of XGB Model

Class	Precision	Recall	F1-Score	Support
Low	0.93	0.99	0.96	67
Moderate	0.89	0.87	0.88	76
High	0.94	0.92	0.93	84
Extreme	1	1	1	87
Overall Accuracy			0.94	314
Macro Avg	0.94	0.94	0.94	314
Weighted Avg	0.94	0.94	0.94	314

The results of past studies can be compared to the outcome by merging numerous variables and employing different algorithms. For example, Sherafati et al. (2013) achieved an R2 of 0.71 in their study utilizing the ANN model to predict the association between urban sprawl factors and LST. Employing a boosted regression tree to combine 2D/3D urban data, LST was calculated on a 60m cell size grid, resulting in a correlation of around 0.85 for various seasons (Hu et al., 2020). Furthermore, Equere et al. (2020) used a spatial regression model to evaluate the association among horizontal and vertical structural features and

LST in San-Francisco and found an R2 of 0.68. Finally, Chun and Guldmann (2014), utilized a regression model that attained an R2 of about 0.70 using a 30 m pixel resolution.

The vast majority of machine learning algorithms perform optimally when the sample size across each class is approximately equal. Equal class size improves the algorithm's performance by enhancing accuracy and minimizing errors. However, if the data set is unbalanced, high accuracy is achieved by forecasting the majority classes while falling short of capturing the minority class, which is the most significant class in this study. Due to small number of training input data for the Extreme class, with less than 3% (over two standard deviations from the mean), the model had initially performed poorly with significant variation in results. Oversampling, a resampling technique, has been used to expand the proportion of copies in the minority class. Oversampling can be advantageous when data are scarce; however, it might result in overfitting and weak generalization (Heung et al., 2016). The resampling of the Extreme class did not compel the model to produce excessive predictions for the class while keeping high prediction values for the other class. Sensitivity tests also showed little impact of overfitting of the model.

The confusion matrix of the model can be seen in Table 7. The confusion matrix provides the visualization of an algorithm's performance. The model almost predicted the Low and Extreme classes perfectly with higher levels of misclassification in the intermediate layers. A future improvement to the model would be integrating the intermediate classes into one, reducing misclassification among them. Additionally, it is critical to note that the Extreme class was not overpredicted, even after manually adjusting the class weight in the model parameters.

Table 7 - Confusion Matrix of XGB Model

Class	Low	Moderate	High	Extreme
Low	66	1	0	0
Moderate	5	66	5	0
High	0	7	77	0
Extreme	0	0	0	87

5.2 Feature Importance

5.2.1 All Features

Figure 29 depicts the top 20 results of SHAP feature importance for the machine learning model. The feature importance is plotted in decreasing order of importance, and the predictor significance diagram illustrates each predictor's relative value and relationship to the outcome. The NDBI index was the most critical factor in the model, accounting for around 25% of the weight, and it is positively correlated with temperature. NDBI is expected to be a key factor in urban environments due to the UHI effect. The enhanced vegetation index (EVI) is the second most important factor, accounting for around 10%. The EVI has an inverse relationship with temperature, with greater values corresponding to lower temperatures. The discovery is consistent with previous research, as trees and plants reduce surface and air temperatures through shade and evapotranspiration. Other key characteristics include DEM, Albedo, the percentage of the population over 65, the percentage of low-skilled workers, and the percentage of the industrial area,

which accounts for roughly 5% of the total influence. Previous research found that NDVI is crucial in predicting temperature-related studies; however, the EVI index surpassed NDVI significantly in the XGBoost model. The EVI index reduces both atmospheric and soil background noise simultaneously compared to NDVI. NDVI may have performed poorly due to the omission of some preprocessing steps in cleaning the satellite imagery data.

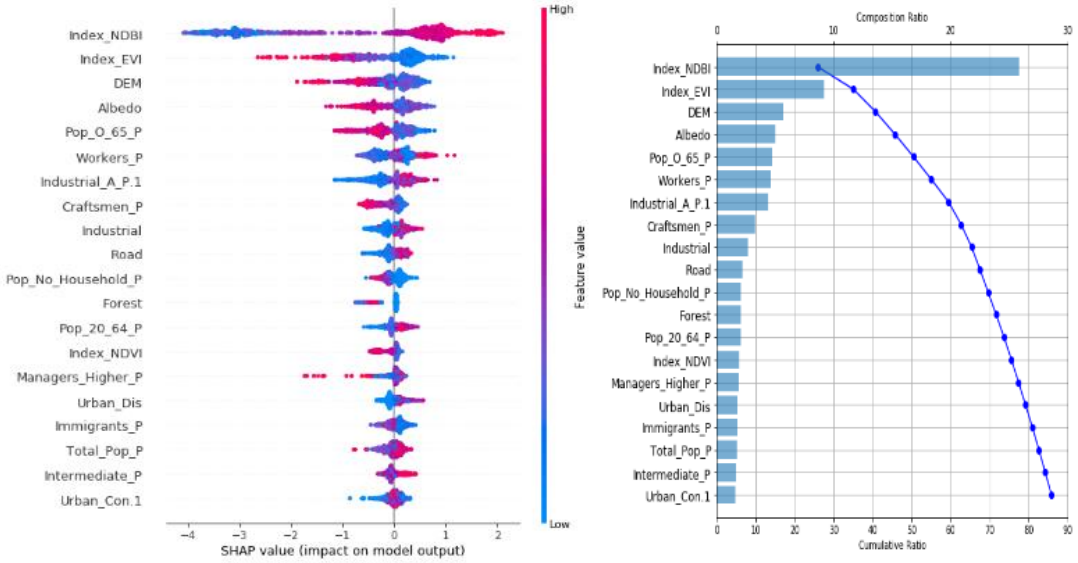

Figure 29 - Feature Importance Analysis for Top 20 Factors: Feature Correlation with Temperature (Left), Feature Contribution to the Model (Right)

Based on the sensitivity analysis results, compared to 3D urban form factors, 2D urban feature characteristics had a greater impact on the LST. The surface temperature is highly connected to 2D urban characteristic factors, whereas the air temperature is closely linked to 3D urban attribute values (Berger et al., 2017). Previously published research demonstrated that the connections among LST and 2D surface variables are greater than those between LST and 3D urban morphology factors (Huang and Wang, 2019). Alavipanah et al. (2018) found both surface and air temperatures to influence UHI formation. Hu et al. (2020) found that NDBI and NDVI remained highly connected towards temperature, when they investigated the impacts of urban variables on UHI during different times of the year. By raising air temperature, 3D urban structural factors can assist in the formation of UHI (Wu and Lung, 2016).

5.2.2 Feature Selection

The final six factors selected for the XGBoost machine learning model can be seen in Figure 30. The correlation with temperature and the overall influence on the model help understand the underlying relationship among the factors in predicting heatwave risk. The factors were selected based on importance in the model encompassing all 70 factors as the PCA analysis, which indicated which combination of factors worked in cohesion. NDBI and the percent of low-skilled workers positively correlate with temperature, whereas EVI and DEM negatively correlate with temperature. Percentage of industrial area and albedo both

have a very weak varying correlation with temperature. As for influence, NDBI has the most significant influence with around 30%, followed by percent of industrial area and EVI accounting for 18%. Albedo is next with 14% and finally DEM and percent of low-skilled workers follow close behind.

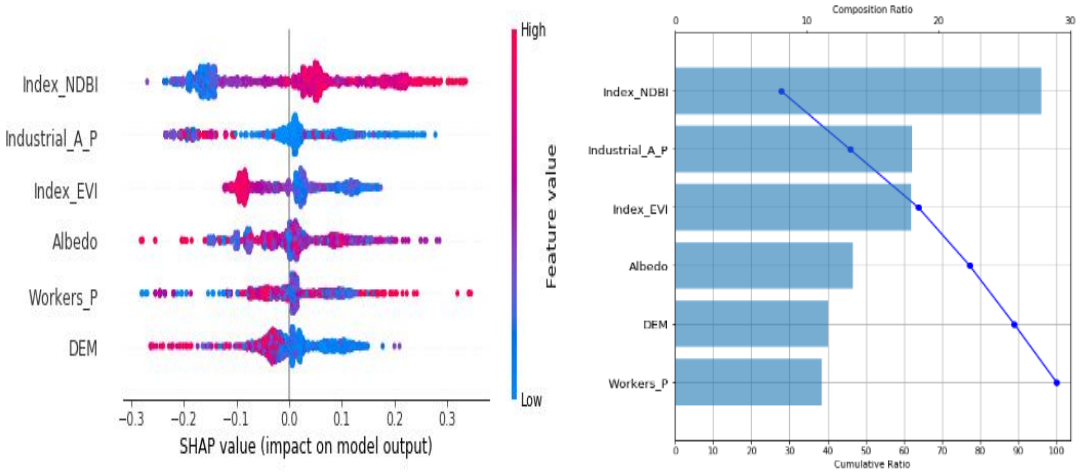

Figure 30 - Feature Importance Analysis for Six Selected Factors: Feature Correlation with Temperature (Left), Feature Contribution to the Model (Right)

Figure 31 depicts in greater detail how the factors influenced different class allocations. Class 0 denotes a Low classification, while class 3 indicates the Extreme class. Despite having a minor input in the overall model, Workers_P greatly aided the model in distinguishing class 3. The model without Workers P resulted in a 12% reduction in overall accuracy, with the Extreme class accuracy reducing by 21%. The general Industrial_A_P was the most important predictor of the Extreme class. Tests revealed that removing the Industrial_A_P and Workers_P variables lowered the models' ability to predict class 3 by 40%. Because class 3 (Extreme) is the most important in this study, it was critical to include Workers_P in the model, even though the population over 65 has a greater overall influence.

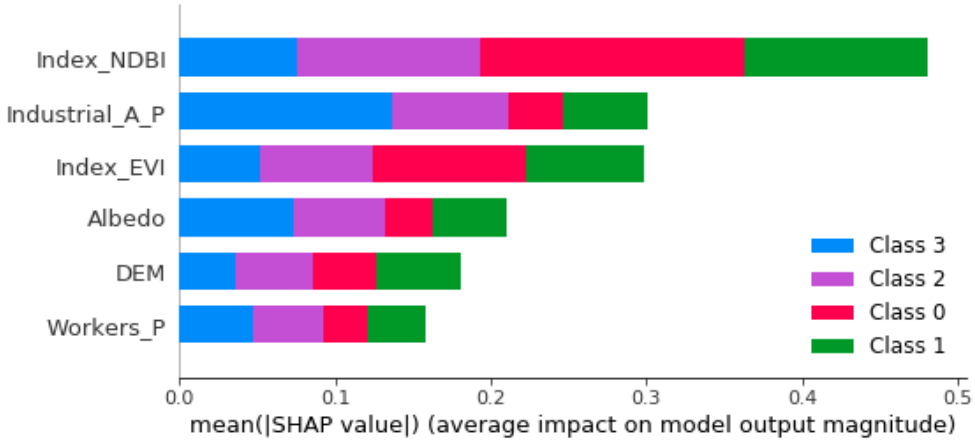

Figure 31 - Factor Contribution to Heatwave Risk Classification (Class 0 = Low, Class 1 = Moderate, Class 2 = High, Class 3 = Extreme)

Figure 32 illustrates the Pearson correlation matrix. Understanding the link between the variables is critical for the subsequent steps, which will involve using mitigation methods to simulate various greening scenarios. The results indicate that EVI, the enhanced vegetation index, is significantly inversely correlated to NDBI, the model's most significant factor. In essence, increasing the vegetation ratio of the IRIS will result in a decrease in temperature, as it is inversely proportional to temperature. As a result, it should have a detrimental influence on NDBI, which is inversely proportional to temperature.

Additionally, increased flora in the IRIS blocks increases the albedo, which substantially negatively influences temperature. Finally, the relationship of changing the one-pixel type to another is established among the factors. The effect of "greenifying" the available land in the most affected areas is simulated.

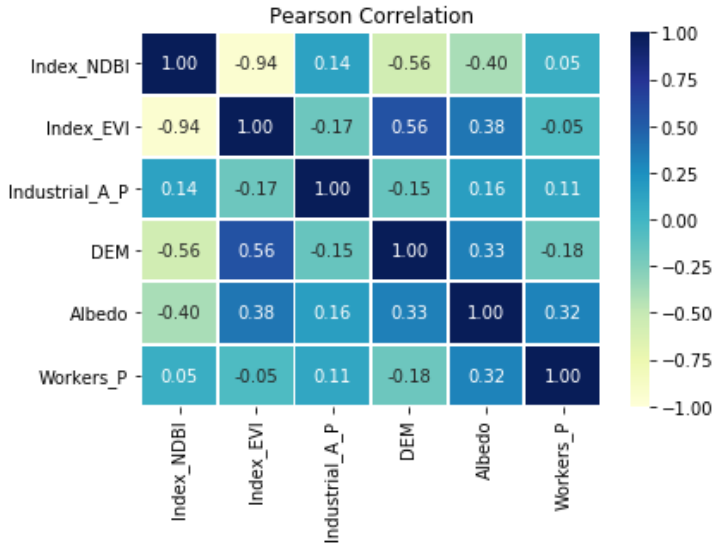

Figure 32 - Correlation Values Among the Factors

5.3 Heatwave Impact Maps

5.3.1 Hazard Map

Figure 33 shows the heatwave hazard map created using the LST estimates. The hazard map shows the LST reclassified into four classes. The IRIS bounds to the north and west are categorized as low risk since they are less inhabited and have a lower buildup to vegetation ratio. Around the center core, where the population density is higher than the surrounding, located at the center of the map with smaller IRIS size, the risk is high, with the surrounding areas having a Moderate risk. In all, 23 IRIS borders pose a severe danger and are primarily residential with substantial industrial areas. Temperatures were higher to the city's east, owing to a more significant proportion of industrial zones adjacent to residential complexes. The factor analysis revealed that industrial areas significantly influenced the model's prediction, particularly in the Extreme

class categorization. The anthropogenic heat and greenhouse gas emission generated by large industries such as warehouses and factories appear to have a significant affect in the microclimate of the area. The hazard map accounts for 50% of the total heatwave risk map.

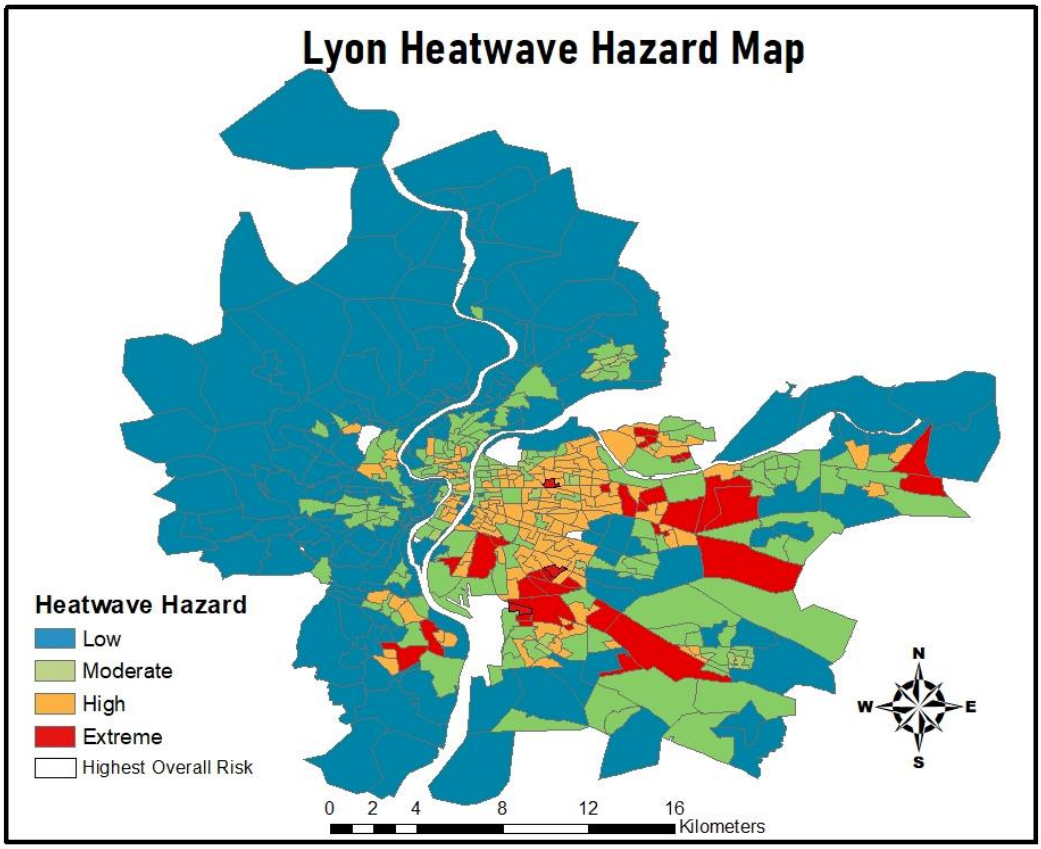

Figure 33 - Heatwave Hazard Map for Lyon

5.3.2.1 Independent Test

To assess the model's predictive capability, it was run on an independent satellite image from a different geographic area. Given that the model was trained exclusively in Lyon, it was critical to determine if the model did not overfit Lyon and could be extended broadly. Figure 34 shows the Glasgow, Scotland heatwave hazard map predicted by the model. The findings indicate that Glasgow's rural regions have the lowest risk, and the risk increases moving closer to the city core. The hazard map follows the general UHI pattern, with urban centers being warmer than rural areas around them.

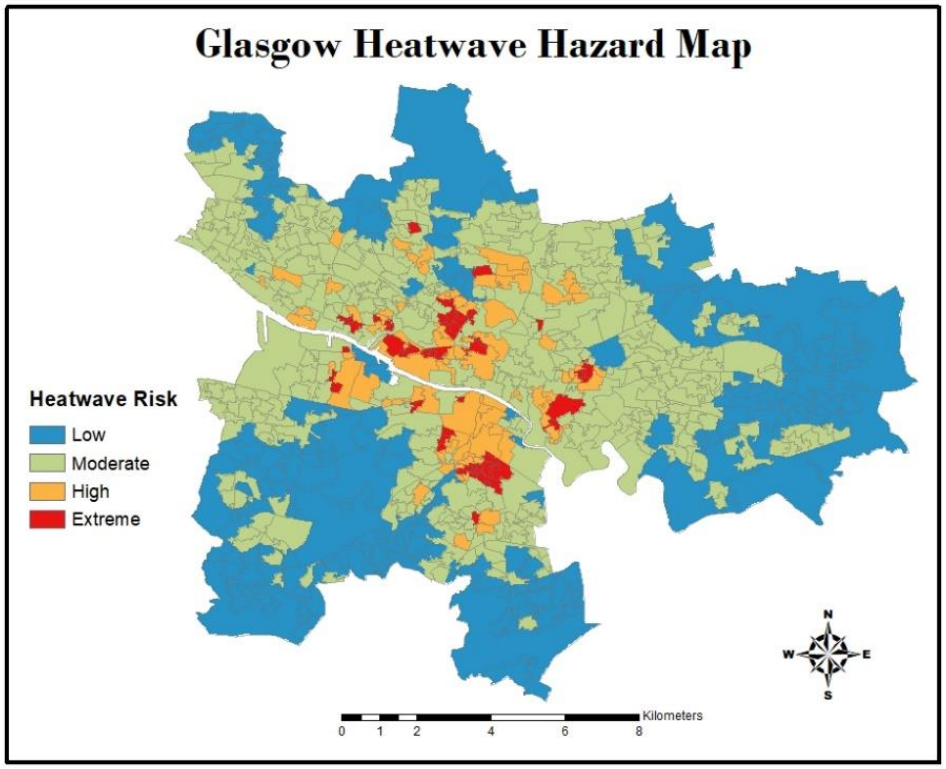

Figure 34 - Heatwave Hazard Map for Glasgow

To properly understand the model's performance, refer to Table 8, which contains the accuracy statistics and confusion matrix. The total accuracy was 81%, with the Extreme class having 100% accurate and the High class obtaining an accuracy of 86%. The model was modified to be more sensitive to the Extreme class, and the accuracy results indicate that this modification was effective. The Moderate class achieved the lowest overall accuracy of 56%. According to the confusion matrix, the Moderate class was approximately equally confused with the Low and High classes. In general, the model performed well in forecasting hazard in Glasgow.

Table 8 - Accuracy Statistics for Glasgow

Class	Precision	Recall	F1-score	Support
Low	0.72	0.85	0.78	66
Moderate	0.71	0.46	0.56	70
High	0.8	0.93	0.86	76
Extreme	1	1	1	70
Overall Accuracy			0.81	282

Class	Low	Moderate	High	Extreme
Low	56	9	1	0
Moderate	21	32	17	0
High	1	4	71	0
Extreme	0	0	0	70

5.3.3 Vulnerability Map

Figure 35 illustrates the heatwave vulnerability map generated using vulnerability indicators. Extreme age, population density, income, and unemployment factors are encompassed in the vulnerability map. The map displays an entirely different pattern from the hazard map, with greater values in western Lyon related to a larger senior population ratio, lower income, and a higher unemployment rate. The center is also associated with increased vulnerability values due to the high population density and extreme age values. Lyon's east and south sides are at Low to Moderate risk, with just two of the four indicators showing high levels. In all, 19 IRIS limits were identified as being at Extreme risk, all of which are located on the western outskirts of Lyon. The vulnerability map accounts for the remaining 50% of the overall heatwave risk map.

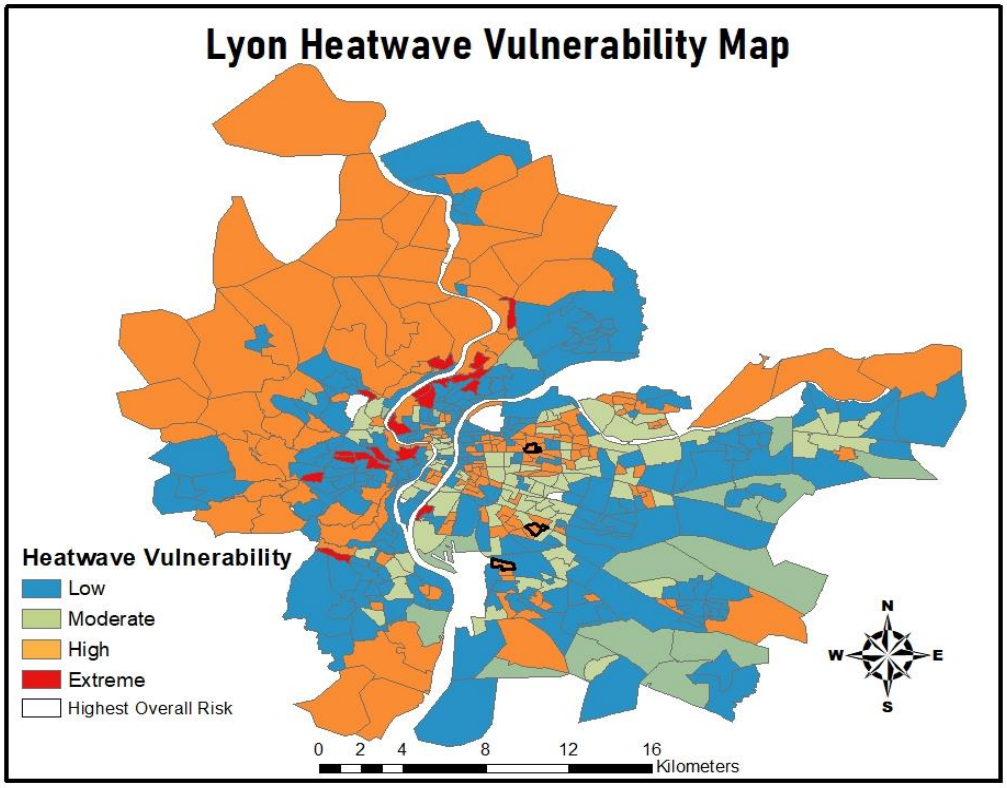

Figure 35 - Heatwave Vulnerability Map of Lyon

5.3.4 Final Heatwave Risk Map

Figure 36 depicts the final heatwave risk map. The combined vulnerability and hazard map reveals a distinct pattern of the most susceptible IRIS boundaries. In the central and eastern areas of Lyon, the highest risk is concentrated. Three IRIS limits are categorized as Extreme in total. The combined map reduced the Extreme class to three from about twenty IRIS zones on the individual hazard and vulnerability maps. Limiting the IRIS to a smaller number of possibilities will assist emergency responders and decision-makers allocate scarce resources to the most impacted regions during a heatwave. The results show that Lyon heatwave risk is not solely influenced by the most urbanized areas but rather a mix of a few factors. The IRIS zones with high NDBI values in the proximity of industrial buildings or zones are most at risk, evident by the eastern part of Lyon being at higher risk due to the higher proportion of industrial activity. The anthropogenic heat and increase in greenhouse gas emission caused by industrial zones could have a major negative effect on microclimate of the zone. The three IRIS regions with the highest risk of heatwaves will be examined further on a larger scale to develop mitigating solutions.

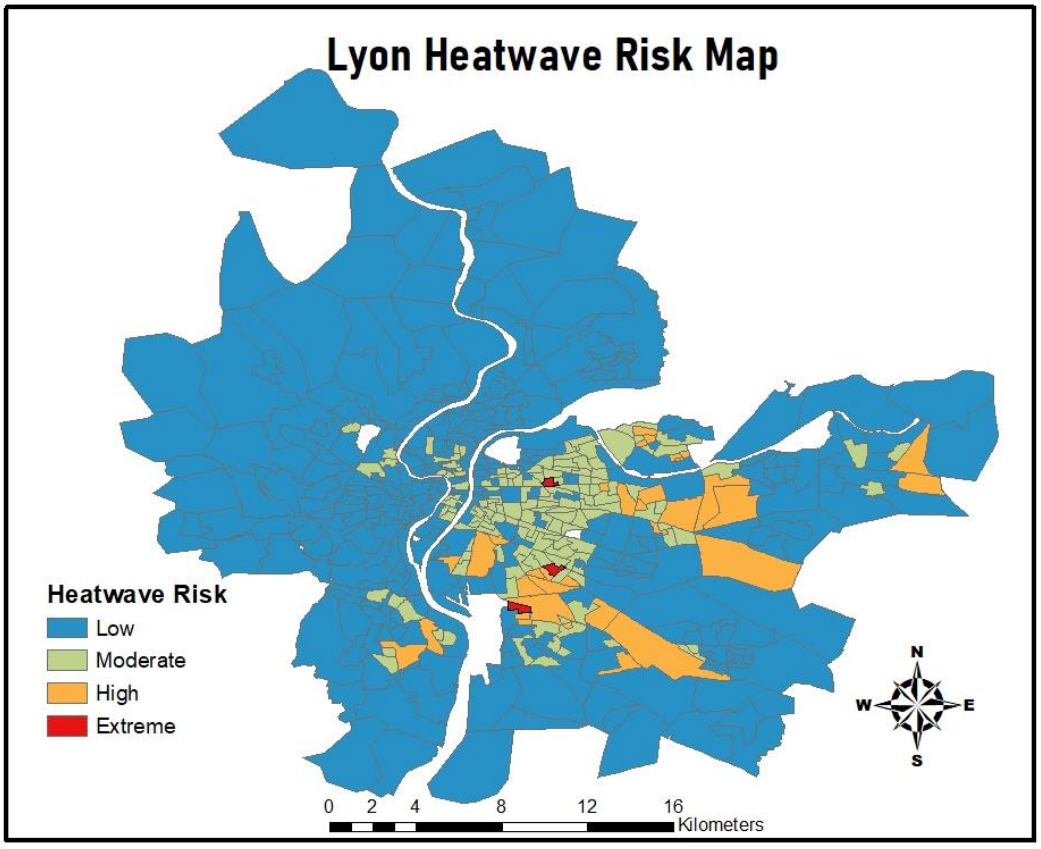

Figure 36 - Heatwave Risk Map for Lyon

5.4 Heatwave Mitigation Strategies

5.4.1 Selected IRIS

A large-scale neighborhood-level analysis of the most affected regions was done using lidar data. Figure 37 shows the three IRIS limits with the highest risk of heatwaves. The severity of the heatwave hazard and the population's sensitivity to heatwaves were used to calculate heatwave risk. Villeurbanne lies in the heart of Lyon, with a population density of 6219 people per square kilometer. It is 304730.34 m^2 in size. Low- and high-rise residential structures and light commercial and industrial facilities make up the IRIS. Extreme circumstances arose from the combination of high NDBI values and a low EVI. Lyon 8e Arrondissement and Saint-Fons cover 438587.16 and 497303.58 square kilometers, respectively, with a population density of about 5500 people per square meters. Both IRIS have a lower NDBI value than Villeubanne, but the areas are surrounded by more industrial zones and contain sparse vegetation.

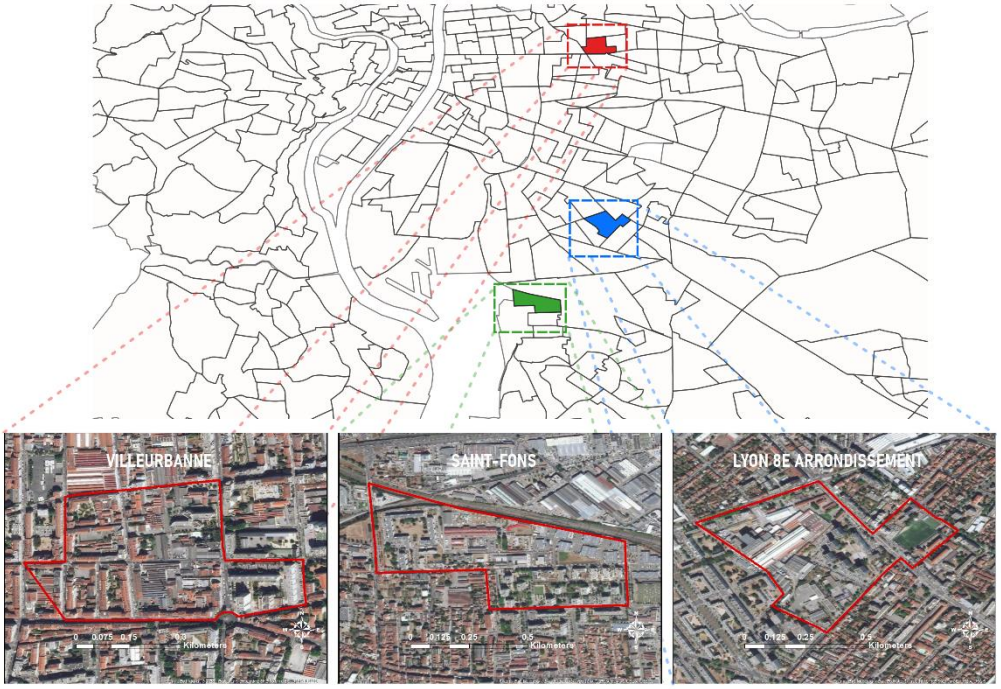

Name: VILLEURBANNE Area: 304730.34 m^2 Population: 1895 people Population Density: 6219 people per square kilometer	Name: SAINT-FONS Area: 497303.58 m^2 Population: 2735 people Population Density: 5500 people per square kilometer	Name: LYON 8E ARRONDISSEMENT Area: 438587.16 m^2 Population: 2431 Population Density: 5543 people per square kilometer

Figure 37 - The Three IRIS bounds with Greatest Heatwave Risk

5.4.2 Lidar Analysis

Lidar data will help turn 3D urban morphology parameters into compatible model parameters, and scenario testing will occur. The parameters calculated are the total building roof area available and the total barren/impervious area, which will then be simulated into different greenifying scenarios: 25%, 50%, 75% of the available area. The scenarios will then be tested in the model, and the results of the mitigation from greenifying the IRIS will provide valuable information on future city planning. For the workflow to be efficient with results coming within a minute, the following assumptions were made:

1) Available building roof areas were calculated only considering the size of the green roof already in place, ignoring other variables such as building roof material type, building roof angle, or any other obstacles that can impede the replacement to a green roof.
2) The change to greenifying scenarios assumed all changes were the same without considering the difference between green roofs and vegetation. All greenifying effects were treated the same without considering type (ex. tree vs. bush).
3) All calculated areas are available for greenifying, and the greenifying scenarios have a uniform effect on the overall IRIS.

Along with precise land-use data, the lidar data aided in the scenario testing of Lyon's most vulnerable areas in the event of a heatwave. The lidar data were divided into separate subclasses, and the percentage of the area associated with each class is presented in Table 9. Villeurbanne is significantly more densely populated and has a greater density of buildings, accounting for 35.34% of the total area. Saint-Fons and Lyon 8E arrondissements with a far lower density of structures have 14.61% and 18.27%, respectively. However, the percentage of impermeable ground available is more significant in both areas than in Villeurbanne, owing to the increased amount of exposed ground in IRIS areas. While Lyon 8e Arrondissement and Saint-Fons have over 15% more impervious ground in the IRIS, the impervious ground suitable for greening is significantly less. The reason is that the latter IRIS areas have a more significant proportion of green space and roads than Villeurbanne. The Impervious Ground area is determined by subtracting the Ground area from the area of roads with a radius of one meter to account for sidewalks and any land use other than barren/impervious surfaces that overlapped the ground areas. Villeurbanne, which also lacks green space, saw a minor decrease, from 30.11% to 28.34% in available impervious ground. Lyon 8e arrondissement impermeable ground coverage was 32.62%, down from 43.7% in total, indicating a more balanced IRIS than Villeurbanne, with modest distributed urban parks and a football pitch. Saint-Fons also decreased from nearly 50% to 35.28% impermeable land, showing more vegetation distributed throughout the IRIS than the other two IRIS.

Table 9 - Percent of Area Associated with Each Class

CLASS	VILLEURBANNE	LYON 8E ARRONDISSEMENT	SAINT-FONS
Ground (Total)	30.11	43.7	49.49
Impervious Ground	28.34	32.62	35.28
Low-Medium Vegetation	11.86	14	14.16
High Vegetation	15.79	17.95	16.74
Building	41.22	23.77	18.52
Rooftop	35.34	18.27	14.61
Other	1.02	0.58	1.08

The percentages of impervious ground and building rooftops converted to m^2 area suitable for greening strategies are shown in Table 10. Owing to the IRIS's varied size, the amount of land available for greening varies significantly. While Villeurbanne has the highest percentage of open areas for greening at 55.68%, due to the smaller size of the IRIS, this equates to approximately 32% less space for development when compared to Saint-Fons, which has the lowest percentage of available areas at 49.88% but a much larger IRIS size. Thus, Villeurbanne has a more balanced input of impervious open ground to building rooftops ratio than the other two IRIS, which has a more dominant contribution from the impervious ground. The differences in the impervious ground and building rooftops ratios amongst IRIS areas will aid in determining which factor contributes the most to the model and hence mitigates heatwave risk the most effectively.

Table 10 - Area Suitable for Greening

	VILLEURBANNE (%)	VILLEURBANNE (m^2)	LYON 8E ARRONDISSEMENT (%)	LYON 8E ARRONDISSEMENT (m^2)	SAINT-FONS (%)	SAINT-FONS (m^2)
Impervious Ground	28.34	86360.58	32.62	143067.13	35.27	175398.97
Building Rooftops	27.34	83313.28	18.27	80129.87	14.61	72656.05
Total Available	55.68	169673.85	50.89	223197	49.88	248055.02

5.4.3 Scenario Results

The available areas were simulated into three different greenifying scenarios: 25%, 50%, 75%. The outcomes of the situations are shown in Table 11. The outcome of the scenario is provided in terms of temperature and heatwave risk categorization. The heatwave risk classification will indicate if the change was sufficient to shift the categorization from Extreme to High or away from the top 2.2% of overall risk. In essence, it would indicate if the scenario had sufficiently decreased the risk for the IRIS by not being categorized as the most extreme class.

Overall, the simulations demonstrate that mitigating the effects of a heatwave on an IRIS that is more densely inhabited with more structures is significantly more challenging than mitigating the impact of a heatwave on a more balanced IRIS. Even with greater greening intensity, the benefits appear to be diminished, compounding the difficulty of mitigating the effects of UHIs in an urban context. Twenty-five percent greening resulted in a minor change in the total temperature and heatwave risk class, with the model continuing to classify all three IRIS as Extreme risk. By greening 50% of the available space, all three locations were lowered to High risk, indicating that the mitigating actions were partly successful. The temperature difference between 0.42°C and 0.52°C was similarly substantial. The importance of other factors contributing to the model can also be seen in Saint-Fons, where a temperature of 39.97°C was classified as Extreme after 25% greening. In contrast, Villeurbanne and Lyon 8E Arrondissement had temperatures of 40.22°C and 40.31°C, respectively, after 50% greening and were classified as High risk. The higher elevation may explain the classification discrepancy, which correlates negatively with temperature and the higher concentration of low-skilled workers in Saint-Fons compared to Villeurbanne and Lyon 8E Arrondissement. Thus, the 75% greening scenario had a negligible effect on Villeurbanne, a mediocre effect on Lyon 8E Arrondissement, and a significant influence on Saint-Fons, but not enough to classify the areas in a lower overall risk class.

Table 11 - Simulation of Greening Scenario Results

	VILLEURBANNE	LYON 8E ARRONDISSEMENT	SAINT-FONS
Original Temperature	40.64	40.83	40.28
Original Risk Class	Extreme	Extreme	Extreme
25% Green Roof & Vegetation (Temp)	40.42	40.52	39.97
25% Green Roof & Vegetation (Class)	Extreme	Extreme	Extreme
50% Green Roof & Vegetation (Temp)	40.22	40.31	39.80
50% Green Roof & Vegetation (Class)	High	High	High
75% Green Roof & Vegetation (Temp)	40.16	40.13	39.43
75% Green Roof & Vegetation (Class)	High	High	High

The result indicates that there might be a threshold for greenifying highly densely populated areas with the effect of mitigation decreasing with more radical plans. The greenifying of impervious ground has the most benefits when applying a radical greenifying transformation. The benefit in temperature is most significant when moving from 50% to 75% for Saint-Fons, which consists of the highest proportion of impervious ground. Figure 38 displays the temperature decrease of the three areas relative to greenifying scenarios. The analysis shows that it is essential to understand the local urban morphology, and one solution fits all might not be the best way forward. Although only available land was considered and greenifying efforts were generalized in this study, it could provide a blueprint for future more intensive methodology and the influence of the locality features on temperature.

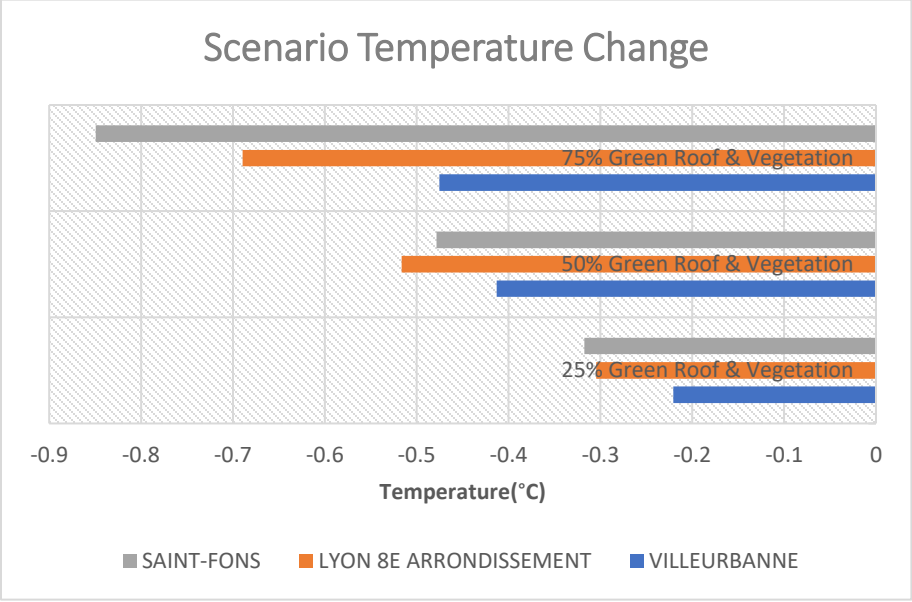

Figure 38 - Scenario Temperature Change

The results of the scenario testing are consistent with previous research. For example, Chun and Guldmann (2014) demonstrated that raising NDVI on building roofs reduced LST between about 1 and 3 degrees Celsius in most cells with a cell size of 120 m. Additionally, a similar study demonstrated that by improving the NDVI value by 0.1 in the most vulnerable places, resulting in a 15% improvement in vegetation, the LST would decrease by 1.27 °C (Mutani and Todeschi, 2020). Additionally, Herrera-Gomez et al. (2017) determined that by raising vegetation cover by 11% to 40%, the LST would decrease by approximately 1.5°C to 6.5°C.

The purpose of this work was to develop an appropriate model for heatwave prediction using effective 2D/3D urban parameters as an expression of hazard and vulnerability indicators. Additionally, sensitivity analysis was used to determine the effect of various parameters on the heatwave prediction model. The lidar-derived land use information aided in determining where future heatwave mitigation efforts could be implemented. Scenarios of greenifying the most stricken areas are simulated to find the effects on urban temperature reduction in Lyon, France. The concept of this study was to develop a process that connects city-scale and neighborhood-scale analysis to determine the optimal urban characteristics factors and machine learning algorithm for heatwave risk, which is beneficial for urban planning policy. The semi-automated method was designed to generate a more generalized rapid analysis. However, it will need to be supplemented with fieldwork and other sources of information to exploit the potential for developing successful mitigation strategies.

5.5 Interactive Online Map

The final heatmap risk map and simulation results are published online to disseminate, exchange, and instantly update heatwave assessment products during an emergency. Using ArcMap Server, the publication of risk maps and analysis products can be remotely accessed and updated from any location. A new layer of data can be rapidly uploaded to the online dynamic map, which also contains a variety of basemaps to further investigate the area of interest. Zooming in and out and the ease with which analysis layers may be switched on/off can be advantageous when assessing damage taking in numerous elements. The online interactive map provides a simple-to-understand interface that can assist decision-makers in maximizing their input of the product's targeted information needed to make suitable emergency response decisions. The interactive map is available at: https://arcg.is/0ODz0v .

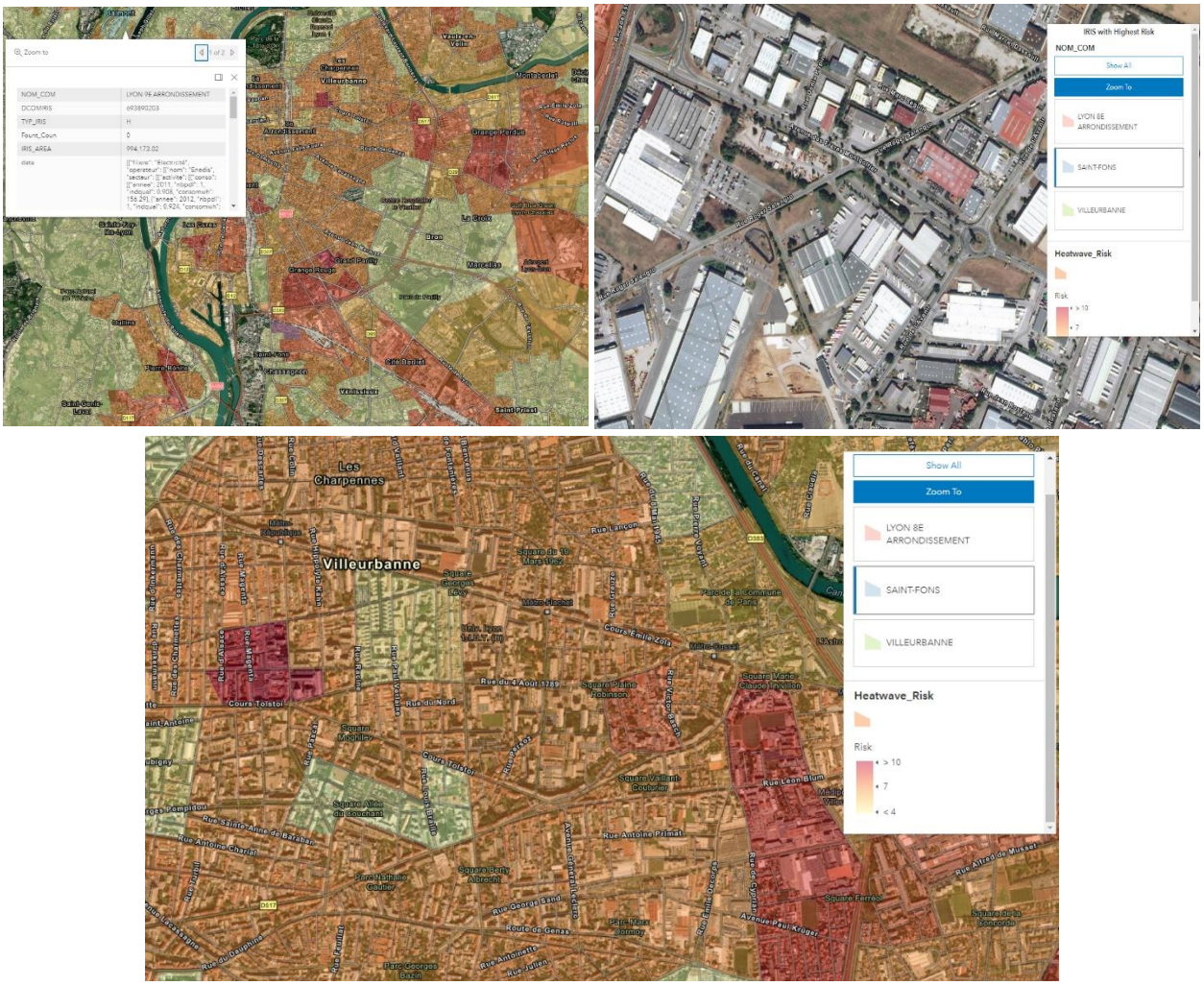

Figure 39 - Snapshots of the Interactive Map

CHAPTER 6: CONCLUSION

For urban heat studies that have depended on a few sparsely distributed meteorological stations in the past to estimate air temperature for a vast and generally diverse zones, it is difficult to capture the heterogeneous makeup of a city. At the onset of a heatwave occurrence, satellite thermal imagery can aide in effectively mapping the regions most susceptible to extreme temperature as well as issuing necessary warnings. Estimation of the geographical heterogeneity of risk variables conducted using satellite images and thermal indices can be produced and can contribute valuable information to the emergency health warning system. Currently, heatwave risk assessment is either too generic and does not portray an accurate representation of urban conditions or require too much data resources, computationally intensive and time-consuming at microscale level.

This research developed a novel semi-automated approach to analyze heatwaves at two different scales: city and neighborhood. Thirteen of the most frequently used machine learning algorithms were used in this research to determine which algorithms delivered the best results for heatwave hotspot identification. XGBoost classifier provided the highest accuracy of 94% and was chosen as the algorithm to base the model on predicting heatwave hotspots. NDBI, EVI, Industrial_A_P, Albedo, Workers_P and DEM are the factors that contributed the most to the projection of heatwave hotspots. NDBI was the most significant factor in the model, accounting for 30% of the total. NDBI, Industrial_A_P and Worker_P had a negative correlation to temperature whereas EVI, albedo and DEM had a negative correlation with temperature. The workflow combined city-scale analysis into neighborhood-scale analysis by examining the most severely affected areas in more detail, and greening scenarios were applied to simulate the appropriate heatwave mitigation threshold. Greenifying 50% of the three most impacted IRIS was sufficient to reduce the risk from Extreme to High, resulting in temperature decrease of 0.4°C to 0.5°C. The model's capacity to forecast heatwave hotspots in other locations was not confined even though it was trained on a heatwave event in Lyon, France. This approach is partly because heatwave intensity was classified using standard deviation statistics based on relative measures rather than absolute temperature readings. When applied to Glasgow, UK, the model produced accuracy of 81% during the 2018 heatwave that swept throughout Europe. It is crucial for decision-makers to quickly explore hotspots at different scales within a heatwave-affected region in order to efficiently allocate emergency operations in a timely manner as well as plan future mitigation strategies to reduce the effect of heatwave in the most impacted areas.

Additionally, the study had several limitations. First, due to a lack of data, the factors included in the analysis may have been incomplete, decreasing the prediction performance. The factors used in the model came from various data sources from different times, sometimes spanning over 10 years which is not representative of the latest ground data. Second, the model was trained on one heatwave event in one city, in order to facilitate processing time. The research data set consisted of two satellite images obtained around a heatwave, which was relatively brief in comparison to other climate studies. Deriving LST from a single heatwave event may be affected by many meteorological conditions such as precipitation, wind direction, and wind speed, therefore more case studies in different seasons and urban environment settings could verify and enhance the results of this study. Cities in various climate zones and data collected over extended periods would expand the data range and representation. Third, various medical incident data from the heatwave and crowdsourced Twitter data can be used to conduct a complete analysis since the data can display exactly where the vulnerable population are located. Finally, the accuracy of existing predicting models is exclusively predicated on LST values derived from satellite images, with no ground-based verification.

While the study's objective was to ascertain a rapid scenario testing framework, the model's estimation might not be very relevant in practice. It is essential to point forth the significant intrinsic constraints of the study. Urban vegetation and green space, according to research, can help to minimize UHI. However, implementing a 75 percent rise in ground-based flora and a green roof with greater albedos across a whole community will be difficult. The model's core building processing assumptions, regardless of whether the roof is slanted or flat, could potentially influence the amount of rooftop space that's available. However, this research is essential because it establishes a fundamental methodology for rapidly forecasting broad-scale green space expansion scenarios. The findings may be applied to other regions to estimate greenifying scenarios. The results should provide an extra resource to city planners and be supplemented by field studies and input from local botanists to provide a comprehensive assessment.

Further research will focus on optimizing the parameters and standardizing the processes associated with machine learning methods to produce accurate LST results with a high spatial resolution. Soil moisture, humidity and other land surface factors associated with LST could be incorporated to determine if these variables aid in heatwave identification. Although the cooling effect of vegetation is significant, based on the findings of this study and previous literature, future research could include vegetation attributes including canopy height, flora species, and biomass, because the cooling effect is reliant on not just the presence of vegetation but also on its type, shape, and size. The investigation of industrial areas within proximity of residential blocks should also be studied in more detail, as the model showed significant negative influence of industrial buildings within residential IRIS blocks. According to previous studies, the 3D urban characteristic factors significantly influence air temperature than they do surface temperature. Thus, to develop a more accurate model, future research should incorporate in-situ data on air temperature as one of the factors for predicting LST fluctuations when designing the heatwave hazard map. Additionally, wind is inextricably linked to urban morphology characteristics and can significantly impact UHIs, which was not examined in this study. As a result, it is advised that future research incorporate wind circulation and wind velocity. This study demonstrated a method for rapidly evaluating the IRIS with minimal resources and established a framework for incorporating the method into a more comprehensive methodology for analyzing heatwaves at the neighborhood level. Locality considerations may assist enhance the methodology in the future by integrating variables such as the kind and location of the intervention since various mitigation actions will have varying degrees of efficacy when considering urban morphology indicators. Also, the results of in situ data regarding greenifying change can be incorporated into the model to calibrate the weights and produce more realistic results.

CHAPTER 7: BIBLIOGRAPHY

ABDI, A.M., 2020. Land cover and land use classification performance of machine learning algorithms in a boreal landscape using Sentinel-2 data. *GIScience and Remote Sensing.* **57**(1), pp.1-20. Available from: 10.1080/15481603.2019.1650447.

AKBARI, H., CARTALIS, C., KOLOKOTSA, D., MUSCIO, A., PISELLO, A.L., ROSSI, F., SANTAMOURIS, M., SYNNEFA, A., WONG, N.H. & ZINZI, M., 2016. Local climate change and urban heat island mitigation techniques - the state of the art. *Journal of Civil Engineering and Management.* **22**(1), pp.1-16. Available from: 10.3846/13923730.2015.1111934.

AKHTAR, R., 2020. *Extreme Weather Events and Human Health International Case Studies.* 1st ed. Cham: Springer International Publishing.

ARSENOVIĆ, D., SAVIĆ, S., LUŽANIN, Z., RADIĆ, I., MILOŠEVIĆ, D. & ARSIĆ, M., 2019. Heat-related mortality as an indicator of population vulnerability in a mid-sized Central European city (Novi Sad, Serbia, summer 2015). *Geographica Pannonnica.* **23**(4), pp.204-215. Available from: 10.5937/gp23-22680.

BAKAR, S.B.A., PRADHAN, B., LAY, U.S. & ABDULLAHI, S. *Spatial assessment of land surface temperature and land use land cover in Langkawi Island.* , 2016.IOP Conf.Ser.: Earth Environ.Sci. IOP PublishingAvailable from: 10.1088/1755-1315/37/1/012064.

BALCIK, F.B., 2014. Determining the impact of urban components on land surface temperature of Istanbul by using remote sensing indices. *Environmental Monitoring and Assessment; Environ Monit Assess.* **186**(2), pp.859-872. Available from: 10.1007/s10661-013-3427-5.

BAN, Y., 2016. *Multitemporal Remote Sensing Methods and Applications.* 1st ed. Cham: Springer International Publishing.

BARTESAGHI KOC, C., OSMOND, P., PETERS, A. & IRGER, M., 2018. Understanding Land Surface Temperature Differences of Local Climate Zones Based on Airborne Remote Sensing Data. *IEEE Journal of Selected Topics in Applied Earth Observations and Remote Sensing.* **11**(8), pp.2724-2730. Available from: 10.1109/JSTARS.2018.2815004.

BEAMON, B.M. & KOTLEBA, S.A., 2006. Inventory modelling for complex emergencies in humanitarian relief operations. *International Journal of Logistics.* **9**(1), pp.1-18. Available from: 10.1080/13675560500453667.

BECHTEL, B. & DANEKE, C., 2012. Classification of Local Climate Zones Based on Multiple Earth Observation Data. *IEEE Journal of Selected Topics in Applied Earth Observations and Remote Sensing.* **5**(4), pp.1191-1202. Available from: 10.1109/JSTARS.2012.2189873.

BISQUERT, M., SANCHEZ, J.M. & CASELLES, V., 2016. Evaluation of Disaggregation Methods for Downscaling MODIS Land Surface Temperature to Landsat Spatial Resolution in Barrax Test Site. *IEEE Journal of Selected Topics in Applied Earth Observations and Remote Sensing.* **9**(4), pp.1430-1438. Available from: 10.1109/JSTARS.2016.2519099.

BOKAIE, M., ZARKESH, M.K., ARASTEH, P.D. & HOSSEINI, A., 2016. Assessment of Urban Heat Island based on the relationship between land surface temperature and Land Use/ Land Cover in Tehran. *Sustainable Cities and Society.* **23**, pp.94-104. Available from: 10.1016/j.scs.2016.03.009.

BRITANNICA., 2018 *Lyon.* Available from: https://www.britannica.com/place/Lyon-France.

CAMPBELL, S.L., REMENYI, T.A., WILLIAMSON, G.J., WHITE, C.J. & JOHNSTON, F.H., 2019. The Value of Local Heatwave Impact Assessment: A Case-Crossover Analysis of Hospital Emergency Department Presentations in Tasmania, Australia. *International Journal of Environmental Research and Public Health; Int J Environ Res Public Health.* **16**(19), pp.3715. Available from: 10.3390/ijerph16193715.

CHAN, H. & KONSTANTINOU, K.I., 2020. Multiscale and multitemporal surface temperature monitoring by satellite thermal infrared imagery at Mayon Volcano, Philippines. *Journal of Volcanology and Geothermal Research.* **401**, pp.106976. Available from: 10.1016/j.jvolgeores.2020.106976.

CHEN, K., LIU, J., GUO, S., CHEN, J., LIU, P., QIAN, J., CHEN, H. & SUN, B., 2016. SHORT-TERM PRECIPITATION OCCURRENCE PREDICTION FOR STRONG CONVECTIVE WEATHER USING FY2-G SATELLITE DATA: A CASE STUDY OF SHENZHEN,SOUTH CHINA. *International Archives of the Photogrammetry, Remote Sensing and Spatial Information Sciences.* **XLI-B6**, pp.215-219. Available from: 10.5194/isprs-archives-XLI-B6-215-2016.

CORTE, A.P.D., SOUZA, D.V., REX, F.E., SANQUETTA, C.R., MOHAN, M., SILVA, C.A., ZAMBRANO, A.M.A., PRATA, G., ALVES DE ALMEIDA, DANILO ROBERTI, TRAUTENMÜLLER, J.W., KLAUBERG, C., DE MORAES, A., SANQUETTA, M.N., WILKINSON, B. & BROADBENT, E.N., 2020. Forest inventory with high-density UAV-Lidar: Machine learning approaches for predicting individual tree attributes. *Computers and Electronics in Agriculture.* **179**, pp.105815. Available from: 10.1016/j.compag.2020.105815.

COUTTS, A.M., HARRIS, R.J., PHAN, T., LIVESLEY, S.J., WILLIAMS, N.S.G. & TAPPER, N.J., 2016. Thermal infrared remote sensing of urban heat: Hotspots, vegetation, and an assessment of techniques for use in urban planning. *Remote Sensing of Environment.* **186**, pp.637-651. Available from: 10.1016/j.rse.2016.09.007.

CUI, Y., XU, X., DONG, J. & QIN, Y., 2016. Influence of Urbanization Factors on Surface Urban Heat Island Intensity: A Comparison of Countries at Different Developmental Phases. *Sustainability (Basel, Switzerland).* **8**(8), pp.706. Available from: 10.3390/su8080706.

DEMUZERE, M., ORRU, K., HEIDRICH, O., OLAZABAL, E., GENELETTI, D., ORRU, H., BHAVE, A.G., MITTAL, N., FELIU, E. & FAEHNLE, M., 2014. Mitigating and adapting to climate change: Multi-functional and multi-scale assessment of green urban infrastructure. *Journal of Environmental Management; J Environ Manage.* **146**, pp.107-115. Available from: 10.1016/j.jenvman.2014.07.025.

DENG, H., 2015. Multicriteria analysis for benchmarking sustainability development. *Benchmarking : An International Journal.* **22**(5), pp.791-807. Available from: 10.1108/BIJ-07-2013-0072.

DNA., 2018 *La centrale de Fessenheim arrête un réacteur.* Available from: https://www.dna.fr/environnement/2018/08/04/la-centrale-de-fessenheim-arrete-un-reacteur.

DONG, L., MITRA, C., GREER, S. & BURT, E., 2018. The dynamical linkage of atmospheric blocking to drought, heatwave and urban heat island in southeastern US: A multi-scale case study. *Atmosphere.* **9**(1), pp.33. Available from: 10.3390/ATMOS9010033.

ELMES, A., HEALY, M., GERON, N., ANDREWS, M.M., ROGAN, J., MARTIN, D.G., SANGERMANO, F., WILLIAMS, C.A. & WEIL, B., 2020. Mapping spatiotemporal variability of the urban heat island across an urban gradient in Worcester, Massachusetts using in-situ Thermochrons and Landsat-8 Thermal Infrared Sensor (TIRS) data. *GIScience and Remote Sensing.* **57**(7), pp.845-864. Available from: 10.1080/15481603.2020.1818950.

ESA., 2006 *Land Surface Temperature*. Available from: https://www.esa.int/ESA_Multimedia/Images/2014/01/Land_surface_temperature.

ESRI., 2016 *Zonal Statistics*. Available from: https://desktop.arcgis.com/en/arcmap/10.3/tools/spatial-analyst-toolbox/zonal-statistics.htm.

FABIANI, C., PISELLO, A.L., BOU-ZEID, E., YANG, J. & COTANA, F., 2019. Adaptive measures for mitigating urban heat islands: The potential of thermochromic materials to control roofing energy balance. *Applied Energy*. **247**, pp.155-170. Available from: 10.1016/j.apenergy.2019.04.020.

FARHAN, A.A., PATTIPATI, K., WANG, B. & LUH, P. *Predicting individual thermal comfort using machine learning algorithms*. , 2015.IEEEAvailable from: 10.1109/CoASE.2015.7294164.

FAUVEL, M., CHANUSSOT, J. & BENEDIKTSSON, J.A., 2009. Kernel Principal Component Analysis for the Classification of Hyperspectral Remote Sensing Data over Urban Areas. *EURASIP Journal on Advances in Signal Processing*. **2009**(1), pp.1-14. Available from: 10.1155/2009/783194.

FU, P. & WENG, Q., 2016. A time series analysis of urbanization induced land use and land cover change and its impact on land surface temperature with Landsat imagery. *Remote Sensing of Environment*. **175**, pp.205-214. Available from: 10.1016/j.rse.2015.12.040.

FULADLU,K., 2020 *Urban Heat Island*. Available from: https://community.wmo.int/activity-areas/urban/urban-heat-islandhttps://community.wmo.int/activity-areas/urban/urban-heat-island.

GELETIČ, J., LEHNERT, M. & DOBROVOLNÝ, P., 2016. Land Surface Temperature Differences within Local Climate Zones, Based on Two Central European Cities. *Remote Sensing (Basel, Switzerland)*. **8**(10), pp.788. Available from: 10.3390/rs8100788.

GOSLING, S.N., MCGREGOR, G.R. & PÁLDY, A., 2007. Climate change and heat-related mortality in six cities Part 1: model construction and validation. *International Journal of Biometeorology; Int J Biometeorol*. **51**(6), pp.525-540. Available from: 10.1007/s00484-007-0092-9.

HAN, G. & XU, J., 2013. Land Surface Phenology and Land Surface Temperature Changes Along an Urban–Rural Gradient in Yangtze River Delta, China. *Environmental Management (New York); Environ Manage*. **52**(1), pp.234-249. Available from: 10.1007/s00267-013-0097-6.

HASHIM, J.H. & HASHIM, Z., 2016. Climate Change, Extreme Weather Events, and Human Health Implications in the Asia Pacific Region. *Asia-Pacific Journal of Public Health; Asia Pac J Public Health*. **28**(2), pp.8S-14S. Available from: 10.1177/1010539515599030.

HEUNG, B., HO, H.C., ZHANG, J., KNUDBY, A., BULMER, C.E. & SCHMIDT, M.G., 2016. An overview and comparison of machine-learning techniques for classification purposes in digital soil mapping. *Geoderma*. **265**, pp.62-77. Available from: 10.1016/j.geoderma.2015.11.014.

HUA, W., CHEN, H., ZHOU, L., XIE, Z., QIN, M., LI, X., MA, H., HUANG, Q. & SUN, S., 2017. Observational quantification of climatic and human influences on vegetation greening in China. *Remote Sensing (Basel, Switzerland)*. **9**(5), pp.425. Available from: 10.3390/rs9050425.

HUANG, Q. & LU, Y., 2015. The Effect of Urban Heat Island on Climate Warming in the Yangtze River Delta Urban Agglomeration in China. *International Journal of Environmental Research and Public Health; Int J Environ Res Public Health*. **12**(8), pp.8773-8789. Available from: 10.3390/ijerph120808773.

HUANG, R., ZHANG, C., HUANG, J., ZHU, D., WANG, L. & LIU, J., 2015. Mapping of daily mean air temperature in agricultural regions using daytime and nighttime land surface temperatures derived from TERRA and AQUA MODIS data. *Remote Sensing (Basel, Switzerland).* **7**(7), pp.8728-8756. Available from: 10.3390/rs70708728.

HUSSAIN, M., CHEN, D., CHENG, A., WEI, H. & STANLEY, D., 2013. Change detection from remotely sensed images: From pixel-based to object-based approaches. *ISPRS Journal of Photogrammetry and Remote Sensing.* **80**, pp.91-106. Available from: 10.1016/j.isprsjprs.2013.03.006.

JAIN,K., 2020 *What is large-scale and small-scale map?* Available from: https://myscienceschool.org/index.php?/archives/13844-What-is-large-scale-and-small-scale-map.html.

JAVANROODI, K., MAHDAVINEJAD, M. & NIK, V.M., 2018. Impacts of urban morphology on reducing cooling load and increasing ventilation potential in hot-arid climate. *Applied Energy.* **231**, pp.714-746. Available from: 10.1016/j.apenergy.2018.09.116.

JEDLOVEC, G., CRANE, D. & QUATTROCHI, D., 2017. Urban heat wave hazard and risk assessment. *Results in Physics.* **7**, pp.4294-4295. Available from: 10.1016/j.rinp.2017.10.056.

KAFY, A.-.A., FAISAL, A., SHUVO, R.M., NAIM, M.N.H., SIKDAR, M.S., CHOWDHURY, R.R., ISLAM, M.A., SARKER, M.H.S., KHAN, M.H.H. & KONA, M.A., 2021. Remote sensing approach to simulate the land use/land cover and seasonal land surface temperature change using machine learning algorithms in a fastest-growing megacity of Bangladesh. *Remote Sensing Applications.* **21**, pp.100463. Available from: 10.1016/j.rsase.2020.100463.

KALMA, J.D., MCVICAR, T.R. & MCCABE, M.F., 2008. Estimating Land Surface Evaporation: A Review of Methods Using Remotely Sensed Surface Temperature Data. *Surveys in Geophysics.* **29**(4), pp.421-469. Available from: 10.1007/s10712-008-9037-z.

KARAKUŞ, C.B., 2019. The Impact of Land Use/Land Cover (LULC) Changes on Land Surface Temperature in Sivas City Center and Its Surroundings and Assessment of Urban Heat Island. *Asia-Pacific Journal of Atmospheric Sciences.* **55**(4), pp.669-684. Available from: 10.1007/s13143-019-00109-w.

LAAIDI, K., ZEGHNOUN, A., DOUSSET, B., BRETIN, P., VANDENTORREN, S., GIRAUDET, E. & BEAUDEAU, P., 2012. The Impact of Heat Islands on Mortality in Paris during the August 2003 Heat Wave. *Environmental Health Perspectives; Environ Health Perspect.* **120**(2), pp.254-259. Available from: 10.1289/ehp.1103532.

LI, J., HEAP, A.D., POTTER, A. & DANIELL, J.J., 2011. Application of machine learning methods to spatial interpolation of environmental variables. *Environmental Modelling & Software : With Environment Data News.* **26**(12), pp.1647-1659. Available from: 10.1016/j.envsoft.2011.07.004.

LI, W., NI, L., LI, Z., DUAN, S. & WU, H., 2019. Evaluation of Machine Learning Algorithms in Spatial Downscaling of MODIS Land Surface Temperature. *IEEE Journal of Selected Topics in Applied Earth Observations and Remote Sensing.* **12**(7), pp.2299-2307. Available from: 10.1109/JSTARS.2019.2896923.

LI, Z. & GUO, X., 2016. Remote sensing of terrestrial non-photosynthetic vegetation using hyperspectral, multispectral, SAR, and LiDAR data. *Progress in Physical Geography.* **40**(2), pp.276-304. Available from: 10.1177/0309133315582005.

LIAO, K., HOU, X. & STRICKLAND, M.J., 2016. Resource allocation for mitigating regional air pollution-related mortality: A summertime case study for five cities in the United States. *Journal of the Air &*

Waste Management Association (1995); J Air Waste Manag Assoc. **66**(8), pp.748-757. Available from: 10.1080/10962247.2016.1176085.

LIN, T., MATZARAKIS, A. & HWANG, R., 2010. Shading effect on long-term outdoor thermal comfort. *Building and Environment.* **45**(1), pp.213-221. Available from: 10.1016/j.buildenv.2009.06.002.

LIU, X., HE, B., GUO, L., HUANG, L. & CHEN, D., 2020. Similarities and Differences in the Mechanisms Causing the European Summer Heatwaves in 2003, 2010, and 2018. *Earth's Future.* **8**(4), pp.n/a. Available from: 10.1029/2019EF001386.

LOWE, D., EBI, K.L. & FORSBERG, B., 2011. Heatwave early warning systems and adaptation advice to reduce human health consequences of heatwaves. *International Journal of Environmental Research and Public Health; Int J Environ Res Public Health.* **8**(12), pp.4623-4648. Available from: 10.3390/ijerph8124623.

MAP FRANCE., 2017 *Map France.* Available from: https://www.map-france.com/Lyon-69000/road-map-Lyon.html.

MASOUDI, M. & TAN, P.Y., 2019. Multi-year comparison of the effects of spatial pattern of urban green spaces on urban land surface temperature. *Landscape and Urban Planning.* **184**, pp.44-58. Available from: 10.1016/j.landurbplan.2018.10.023.

MILLS, D.M., 2009. Climate Change, Extreme Weather Events, and US Health Impacts: What Can We Say?. *Journal of Occupational and Environmental Medicine; J Occup Environ Med.* **51**(1), pp.26-32. Available from: 10.1097/JOM.0b013e31817d32da.

MODARESI, F., ARAGHINEJAD, S. & EBRAHIMI, K., 2018. A Comparative Assessment of Artificial Neural Network, Generalized Regression Neural Network, Least-Square Support Vector Regression, and K-Nearest Neighbor Regression for Monthly Streamflow Forecasting in Linear and Nonlinear Conditions. *Water Resources Management.* **32**(1), pp.243-258. Available from: 10.1007/s11269-017-1807-2.

MOOLGAVKAR, S.H., 2000. Air Pollution and Daily Mortality in Three U.S. Counties. *Environmental Health Perspectives; Environ Health Perspect.* **108**(8), pp.777-784. Available from: 10.1289/ehp.00108777.

MORABITO, M., CRISCI, A., GIOLI, B., GUALTIERI, G., TOSCANO, P., DI STEFANO, V., ORLANDINI, S. & GENSINI, G.F., 2015. Urban-hazard risk analysis: Mapping of heat-related risks in the elderly in major Italian cities. *PloS One; PLoS One.* **10**(5), pp.e0127277. Available from: 10.1371/journal.pone.0127277.

MUSHORE, T.D., MUTANGA, O., ODINDI, J. & DUBE, T., 2018. Determining extreme heat vulnerability of Harare Metropolitan City using multispectral remote sensing and socio-economic data. *Journal of Spatial Science.* **63**(1), pp.173-191. Available from: 10.1080/14498596.2017.1290558.

MYINT, S.W., GOBER, P., BRAZEL, A., GROSSMAN-CLARKE, S. & WENG, Q., 2011. Per-pixel vs. object-based classification of urban land cover extraction using high spatial resolution imagery. *Remote Sensing of Environment.* **115**(5), pp.1145-1161. Available from: 10.1016/j.rse.2010.12.017.

NANDLALL, S.D. & MILLARD, K., 2020. Quantifying the Relative Importance of Variables and Groups of Variables in Remote Sensing Classifiers Using Shapley Values and Game Theory. *IEEE Geoscience and Remote Sensing Letters.* **17**(1), pp.42-46. Available from: 10.1109/LGRS.2019.2914374.

OTTO, F., 2019. Attribution of extreme weather events: how does climate change affect weather?. *Weather.* **74**(9), pp.325-326. Available from: 10.1002/wea.3610.

PANT,A., 2019 *Workflow of a Machine Learning project.* Available from: https://towardsdatascience.com/workflow-of-a-machine-learning-project-ec1dba419b94.

PARK, J. & KIM, J., 2018. Defining heatwave thresholds using an inductive machine learning approach. *PloS One; PLoS One.* **13**(11), pp.e0206872. Available from: 10.1371/journal.pone.0206872.

PERKINS-KIRKPATRICK, S. & GIBSON, P.B., 2017. Changes in regional heatwave characteristics as a function of increasing global temperature. *Scientific Reports; Sci Rep.* **7**(1), pp.12256-12. Available from: 10.1038/s41598-017-12520-2.

PERKINS-KIRKPATRICK, S., WHITE, C.J., ALEXANDER, L.V., ARGÜESO, D., BOSCHAT, G., COWAN, T., EVANS, J.P., EKSTRÖM, M., OLIVER, E.C.J., PHATAK, A. & PURICH, A., 2016. Natural hazards in Australia: heatwaves. *Climatic Change.* **139**(1), pp.101-114. Available from: 10.1007/s10584-016-1650-0.

PETERSON, K.T., SAGAN, V. & SLOAN, J.J., 2020. Deep learning-based water quality estimation and anomaly detection using Landsat-8/Sentinel-2 virtual constellation and cloud computing. *GIScience and Remote Sensing.* **57**(4), pp.510-525. Available from: 10.1080/15481603.2020.1738061.

PETERSON, T.C., GALLO, K.P., LAWRIMORE, J., OWEN, T.W., HUANG, A. & MCKITTRICK, D.A., 1999. Global rural temperature trends. *Geophysical Research Letters; Geophys.Res.Lett.* **26**(3), pp.329-332. Available from: 10.1029/1998GL900322.

POWELL, R. & BROOKS, C., 2008. Land Use Land Cover Mapping in the Tiffin River Watershed. *Michigan Tech Research Institute.* . Available from: Land Use Land Cover Mapping in the Tiffin River Watershed.

RAFAEL, S., VICENTE, B., RODRIGUES, V., MIRANDA, A.I., BORREGO, C. & LOPES, M., 2018. Impacts of green infrastructures on aerodynamic flow and air quality in Porto's urban area. *Atmospheric Environment (1994).* **190**, pp.317-330. Available from: 10.1016/j.atmosenv.2018.07.044.

RAO, P.J., RAO, K.N. & KUBO, S., 2018. *Proceedings of International Conference on Remote Sensing for Disaster Management: Issues and Challenges in Disaster Management.* Cham: Springer International Publishing AG.

RAY, S. *A Quick Review of Machine Learning Algorithms.* , 2019.IEEEAvailable from: 10.1109/COMITCon.2019.8862451.

RODRIGUES, V., SORTE, S., COELHO, S., RAFAEL, S., ASCENSO, A., LOPES, M., MIRANDA, A.I. & BORREGO, C. *Modelling the Potential of Green Infrastructures to Reduce the Impact of Climate Change on Air Quality at Microscale.* , 2019.Cham: Springer International PublishingAvailable from: 10.1007/978-3-030-22055-6_23.

SAMOLI, E., TOULOUMI, G., SCHWARTZ, J., ANDERSON, H.R., SCHINDLER, C., FORSBERG, B., VIGOTTI, M.A., VONK, J., KOSNIK, M., SKORKOVSKY, J. & KATSOUYANNI, K., 2007. Short-Term Effects of Carbon Monoxide on Mortality: An Analysis within the APHEA Project. *Environmental Health Perspectives; Environ Health Perspect.* **115**(11), pp.1578-1583. Available from: 10.1289/ehp.10375.

SANCHEZ CRISTAL, N., METCALF, N., KREISBERG, D. & LITTLE, C.M., 2019. Integrating Simulation-Based Exercises into Public Health Emergency Management Curricula. *Disaster Medicine and Public Health Preparedness; Disaster Med.Public Health Prep.* **13**(4), pp.777-781. Available from: 10.1017/dmp.2018.137.

SANSARE, D.A. & MHASKE, S.Y., 2020. Natural hazard assessment and mapping using remote sensing and QGIS tools for Mumbai city, India. *Natural Hazards (Dordrecht).* **100**(3), pp.1117-1136. Available from: 10.1007/s11069-019-03852-5.

SANTAMOURIS, M., 2013. Using cool pavements as a mitigation strategy to fight urban heat island—A review of the actual developments. *Renewable & Sustainable Energy Reviews.* **26**, pp.224-240. Available from: 10.1016/j.rser.2013.05.047.

SANTAMOURIS, M. & OSMOND, P., 2020. Increasing Green Infrastructure in Cities: Impact on Ambient Temperature, Air Quality and Heat-Related Mortality and Morbidity. *Buildings (Basel).* **10**(12), pp.233. Available from: 10.3390/buildings10120233.

SAPUTRA, M.H. & LEE, H.S., 2019. Prediction of Land Use and Land Cover Changes for North Sumatra, Indonesia, Using an Artificial-Neural-Network-Based Cellular Automaton. *Sustainability (Basel, Switzerland).* **11**(11), pp.3024. Available from: 10.3390/su11113024.

SCOTT, D., PETROPOULOS, G., MOXLEY, J. & MALCOLM, H., 2014. Quantifying the Physical Composition of Urban Morphology throughout Wales Based on the Time Series (1989–2011) Analysis of Landsat TM/ETM+ Images and Supporting GIS Data. *Remote Sensing (Basel, Switzerland).* **6**(12), pp.11731-11752. Available from: 10.3390/rs61211731.

SHACKELFORD, A.K. & DAVIS, C.H., 2003. A combined fuzzy pixel-based and object-based approach for classification of high-resolution multispectral data over urban areas. *IEEE Transactions on Geoscience and Remote Sensing.* **41**(10), pp.2354-2363. Available from: 10.1109/TGRS.2003.815972.

SHATNAWI, N. & ABU QDAIS, H., 2019. Mapping urban land surface temperature using remote sensing techniques and artificial neural network modelling. *International Journal of Remote Sensing.* **40**(10), pp.3968-3983. Available from: 10.1080/01431161.2018.1557792.

SHI, Y., REN, C., LUO, M., CHING, J., LI, X., BILAL, M., FANG, X. & REN, Z., 2021. Utilizing world urban database and access portal tools (WUDAPT) and machine learning to facilitate spatial estimation of heatwave patterns. *Urban Climate.* **36**, pp.100797. Available from: 10.1016/j.uclim.2021.100797.

SMITH, J.B., SCHNEIDER, S.H., OPPENHEIMER, M., YOHE, G.W., HARE, W., MASTRANDREA, M.D., PATWARDHAN, A., BURTON, I., CORFEE-MORLOT, J., MAGADZA, C.H.D., FÜSSEL, H., PITTOCK, A.B., RAHMAN, A., SUAREZ, A. & VAN YPERSELE, J., 2009. Assessing Dangerous Climate Change through an Update of the Intergovernmental Panel on Climate Change (IPCC) "Reasons for Concern". *Proceedings of the National Academy of Sciences - PNAS; Proc Natl Acad Sci U S A.* **106**(11), pp.4133-4137. Available from: 10.1073/pnas.0812355106.

SOLTANIFARD, H. & ALIABADI, K., 2019. Impact of urban spatial configuration on land surface temperature and urban heat islands: a case study of Mashhad, Iran. *Theoretical and Applied Climatology.* **137**(3), pp.2889-2903. Available from: 10.1007/s00704-018-2738-4.

SONG, C., WOODCOCK, C.E., SETO, K.C., LENNEY, M.P. & MACOMBER, S.A., 2001. Classification and Change Detection Using Landsat TM Data: When and How to Correct Atmospheric Effects?. *Remote Sensing of Environment.* **75**(2), pp.230-244. Available from: 10.1016/S0034-4257(00)00169-3.

STAFOGGIA, M., FORASTIERE, F., AGOSTINI, D., BIGGERI, A., BISANTI, L., CADUM, E., CARANCI, N., DE'DONATO, F., DE LISIO, S., DE MARIA, M., MICHELOZZI, P., MIGLIO, R., PANDOLFI, P., PICCIOTTO, S., ROGNONI, M., RUSSO, A., SCARNATO, C. & PERUCCI, C.A., 2006. Vulnerability to Heat-Related Mortality: A Multicity, Population-Based, Case-Crossover Analysis. *Epidemiology (Cambridge, Mass.); Epidemiology.* **17**(3), pp.315-323. Available from: 10.1097/01.ede.0000208477.36665.34.

STEWART, I.D., OKE, T.R. & KRAYENHOFF, E.S., 2014. Evaluation of the 'local climate zone' scheme using temperature observations and model simulations. *International Journal of Climatology.* **34**(4), pp.1062-1080. Available from: 10.1002/joc.3746.

SULTANA, S. & SATYANARAYANA, A.N.V., 2020. Assessment of urbanisation and urban heat island intensities using landsat imageries during 2000 – 2018 over a sub-tropical Indian City. *Sustainable Cities and Society.* **52**, pp.101846. Available from: 10.1016/j.scs.2019.101846.

TAO, L., CHEN, H., XU, Y. & ZHU, Z. *A New Promoter Recognition Method Based on Features Optimal Selection.* , 2011.IEEEAvailable from: 10.1109/icbbe.2011.5779973.

TONG,F., 2019 *Everything you need to know about Graph Theory for Deep Learning.* Available from: https://towardsdatascience.com/graph-theory-and-deep-learning-know-hows-6556b0e9891b.

UYAR, T.S., 2017. *Towards 100% Renewable Energy Techniques, Costs and Regional Case-Studies.* 1st ed. Cham: Springer International Publishing.

VARGO, J., HABEEB, D. & STONE, B., 2013. The importance of land cover change across urban–rural typologies for climate modeling. *Journal of Environmental Management; J Environ Manage.* **114**, pp.243-252. Available from: 10.1016/j.jenvman.2012.10.007.

WANG, Y., OLOFSSON, T., SHEN, Q. & BAI, Y., 2015. *ICCREM 2015 : environment and the sustainable building : proceedings of the 2015 International Conference on Construction and Real Estate Management, August 11-12, 2015, Lule﷽a, Sweden.* Reston, Virginia: American Society of Civil Engineers.

WEIERS, S., BOCK, M., WISSEN, M. & ROSSNER, G., 2004. Mapping and indicator approaches for the assessment of habitats at different scales using remote sensing and GIS methods. *Landscape and Urban Planning.* **67**(1), pp.43-65. Available from: 10.1016/S0169-2046(03)00028-8.

WERE, K., BUI, D.T., DICK, ØB. & SINGH, B.R., 2015. A comparative assessment of support vector regression, artificial neural networks, and random forests for predicting and mapping soil organic carbon stocks across an Afromontane landscape. *Ecological Indicators.* **52**, pp.394-403. Available from: 10.1016/j.ecolind.2014.12.028.

WOOTTON-BEARD, P., XING, Y., DURAI PRABHAKARAN, R., ROBSON, P., BOSCH, M., THORNTON, J., ORMONDROYD, G., JONES, P. & DONNISON, I., 2016. Review: Improving the Impact of Plant Science on Urban Planning and Design. *Buildings (Basel).* **6**(4), pp.48. Available from: 10.3390/buildings6040048.

WU, Q., ZHONG, R., ZHAO, W., FU, H. & SONG, K., 2017. A comparison of pixel-based decision tree and object-based Support Vector Machine methods for land-cover classification based on aerial images and airborne lidar data. *International Journal of Remote Sensing.* **38**(23), pp.7176-7195. Available from: 10.1080/01431161.2017.1371864.

WWA., 2018a *Heatwave in northern Europe, summer 2018.* Available from: https://www.worldweatherattribution.org/attribution-of-the-2018-heat-in-northern-europe/.

WWA., 2018b *Heatwave in northern Europe, summer 2018.* Available from: https://www.worldweatherattribution.org/attribution-of-the-2018-heat-in-northern-europe/.

YANG, J., MOHAN KUMAR, D.L., PYRGOU, A., CHONG, A., SANTAMOURIS, M., KOLOKOTSA, D. & LEE, S.E., 2018. Green and cool roofs' urban heat island mitigation potential in tropical climate. *Solar Energy.* **173**, pp.597-609. Available from: 10.1016/j.solener.2018.08.006.

ZHANG, Y. & SUN, L., 2019. Spatial-temporal impacts of urban land use land cover on land surface temperature: Case studies of two Canadian urban areas. *International Journal of Applied Earth Observation and Geoinformation*. **75**, pp.171-181. Available from: 10.1016/j.jag.2018.10.005.

ZHAO, C., JENSEN, J., WENG, Q., CURRIT, N. & WEAVER, R., 2019. Application of airborne remote sensing data on mapping local climate zones: Cases of three metropolitan areas of Texas, U.S. *Computers, Environment and Urban Systems*. **74**, pp.175-193. Available from: 10.1016/j.compenvurbsys.2018.11.002.

ZHAO, W., DUAN, S., LI, A. & YIN, G., 2019. A practical method for reducing terrain effect on land surface temperature using random forest regression. *Remote Sensing of Environment*. **221**, pp.635-649. Available from: 10.1016/j.rse.2018.12.008.

ZHAO, W., WU, H., YIN, G. & DUAN, S., 2019. Normalization of the temporal effect on the MODIS land surface temperature product using random forest regression. *ISPRS Journal of Photogrammetry and Remote Sensing*. **152**, pp.109-118. Available from: 10.1016/j.isprsjprs.2019.04.008.

ZHOU, J., CHEN, Y., ZHANG, X. & ZHAN, W., 2013. Modelling the diurnal variations of urban heat islands with multi-source satellite data. *International Journal of Remote Sensing*. **34**(21), pp.7568-7588. Available from: 10.1080/01431161.2013.821576.

ZHOU, K., LIU, H., DENG, X., WANG, H. & ZHANG, S., 2020. Comparison of Machine-Learning Algorithms for Near-Surface Air-Temperature Estimation from FY-4A AGRI Data. *Advances in Meteorology*. **2020**. Available from: 10.1155/2020/8887364.

ZIEN, A., KRÄMER, N., SONNENBURG, S. & RÄTSCH, G. *The Feature Importance Ranking Measure*. , 2009.Berlin, Heidelberg: Springer Berlin HeidelbergAvailable from: 10.1007/978-3-642-04174-7_45.

CHAPTER 8: APPENDIX

8.1 Machine Learning Algorithms Confusion Matrix and Accuracy

ADA

Classification Report

	precision	recall	f1-score	support
1	0.76	0.81	0.78	67
2	0.55	0.30	0.39	76
3	0.49	0.88	0.63	84
4	0.92	0.54	0.68	87
accuracy			0.63	314
macro avg	0.68	0.63	0.62	314
weighted avg	0.68	0.63	0.62	314

Confusion Matrix

[[54 13 0 0]

[17 23 36 0]

[0 6 74 4]

[0 0 40 47]]

Accuracy

TrainADA: 0.579790 (0.105931) TestADA: 0.490271 (0.081446)

CART

Classification Report

	precision	recall	f1-score	support
1	0.90	0.96	0.93	67
2	0.82	0.76	0.79	76
3	0.88	0.88	0.88	84
4	0.99	1.00	0.99	87
accuracy			0.90	314
macro avg	0.90	0.90	0.90	314
weighted avg	0.90	0.90	0.90	314

Confusion Matrix

[[64 3 0 0]

[7 58 10 1]

[0 10 74 0]

[0 0 0 87]]

Accuracy

TrainCART: 0.866030 (0.023974) TestCART: 0.770558 (0.033811)

GBC

Classification Report

	precision	recall	f1-score	support
1	0.90	0.99	0.94	67
2	0.86	0.82	0.84	76
3	0.91	0.87	0.89	84
4	0.98	1.00	0.99	87
accuracy			0.92	314
macro avg	0.91	0.92	0.91	314
weighted avg	0.92	0.92	0.92	314

Confusion Matrix

[[66 1 0 0]

[7 62 7 0]

[0 9 73 2]

[0 0 0 87]]

Accuracy

TrainGBC: 0.885967 (0.016043) TestGBC: 0.757860 (0.026415)

KNN

Classification Report

	precision	recall	f1-score	support
1	0.83	0.94	0.88	67
2	0.64	0.59	0.62	76
3	0.76	0.67	0.71	84
4	0.93	1.00	0.96	87
accuracy			0.80	314
macro avg	0.79	0.80	0.79	314
weighted avg	0.79	0.80	0.79	314

Confusion Matrix

[[63 4 0 0]

[13 45 18 0]

[0 21 56 7]

[0 0 0 87]]

Accuracy

TrainKNN: 0.808609 (0.017676) TestKNN: 0.697184 (0.047082)

LDA

Classification Report

	precision	recall	f1-score	support
1	0.76	0.90	0.82	67
2	0.73	0.50	0.59	76
3	0.61	0.77	0.68	84
4	0.86	0.76	0.80	87
accuracy			0.73	314
macro avg	0.74	0.73	0.73	314
weighted avg	0.74	0.73	0.73	314

Confusion Matrix

[[60 6 1 0]

[19 38 19 0]

[0 8 65 11]

[0 0 21 66]]

Accuracy

TrainLDA: 0.743984 (0.022632) TestLDA: 0.719611 (0.059743)

LR

Classification Report

	precision	recall	f1-score	support
1	0.78	0.90	0.83	67
2	0.66	0.58	0.62	76
3	0.65	0.67	0.66	84
4	0.86	0.83	0.84	87
accuracy			0.74	314
macro avg	0.74	0.74	0.74	314
weighted avg	0.74	0.74	0.74	314

Confusion Matrix

[[60 7 0 0]

[17 44 15 0]

[0 16 56 12]

[0 0 15 72]]

Accuracy

TrainLR: 0.734432 (0.030466) TestLR: 0.703687 (0.055405)

LSVM

Classification Report

	precision	recall	f1-score	support
1	0.72	0.96	0.82	67
2	0.75	0.32	0.44	76
3	0.60	0.74	0.66	84
4	0.82	0.84	0.83	87
accuracy			0.71	314
macro avg	0.72	0.71	0.69	314
weighted avg	0.72	0.71	0.69	314

Confusion Matrix

[[64 1 2 0]

[25 24 26 1]

[0 7 62 15]

[0 0 14 73]]

Accuracy

TrainLSVM: 0.710512 (0.016522) TestLSVM: 0.678239 (0.037682)

MLP

Classification Report

	precision	recall	f1-score	support
1	0.85	0.93	0.89	67
2	0.76	0.59	0.67	76
3	0.72	0.81	0.76	84
4	0.92	0.93	0.93	87
accuracy			0.82	314
macro avg	0.81	0.81	0.81	314
weighted avg	0.81	0.82	0.81	314

Confusion Matrix

[[62 5 0 0]

[11 45 20 0]

[0 9 68 7]

[0 0 6 81]]

Accuracy

TrainMLP: 0.771076 (0.039029) TestMLP: 0.748387 (0.036856)

NB

Classification Report

	precision	recall	f1-score	support
1	0.78	0.87	0.82	67
2	0.64	0.58	0.61	76
3	0.61	0.63	0.62	84
4	0.83	0.80	0.82	87
accuracy			0.72	314
macro avg	0.72	0.72	0.72	314
weighted avg	0.72	0.72	0.72	314

Confusion Matrix

[[58 8 1 0]

[16 44 16 0]

[0 17 53 14]

[0 0 17 70]]

Accuracy

TrainNB: 0.740810 (0.029679) TestNB: 0.697440 (0.020172)

RF

Classification Report

	precision	recall	f1-score	support
1	0.88	0.99	0.93	67
2	0.83	0.78	0.80	76
3	0.90	0.87	0.88	84
4	1.00	1.00	1.00	87
accuracy			0.91	314
macro avg	0.90	0.91	0.90	314
weighted avg	0.91	0.91	0.91	314

Confusion Matrix

```
[[66  1  0  0]
 [ 9 59  8  0]
 [ 0 11 73  0]
 [ 0  0  0 87]]
```

Accuracy

TrainRF: 0.900306 (0.011400) TestRF: 0.783359 (0.031686)

SVM

Classification Report

	precision	recall	f1-score	support
1	0.82	0.96	0.88	67
2	0.77	0.62	0.69	76
3	0.69	0.79	0.74	84
4	0.91	0.84	0.87	87
accuracy			0.80	314
macro avg	0.80	0.80	0.80	314
weighted avg	0.80	0.80	0.79	314

Confusion Matrix

[[64 3 0 0]

[14 47 15 0]

[0 11 66 7]

[0 0 14 73]]

Accuracy

TrainSVM: 0.791066 (0.031547) TestSVM: 0.726011 (0.034760)

Tree

Classification Report

	precision	recall	f1-score	support
1	0.90	0.94	0.92	67
2	0.80	0.78	0.79	76
3	0.89	0.87	0.88	84
4	0.99	1.00	0.99	87
accuracy			0.90	314
macro avg	0.89	0.90	0.90	314
weighted avg	0.90	0.90	0.90	314

Confusion Matrix

[[63 4 0 0]

[7 59 9 1]

[0 11 73 0]

[0 0 0 87]]

Accuracy

TrainTree: 0.863630 (0.010887) TestTree: 0.776959 (0.042047)